Nanoscale

ROYAL SOCIETY OF CHEMISTRY

REVIEW

View Article Online
View Journal | View Issue

Cite this: *Nanoscale*, 2024, **16**, 15851

Understanding and tuning magnetism in van der Waals-type metal thiophosphates

Rabindra Basnet *[a] and Jin Hu *[b,c]

Received 11th April 2024,
Accepted 29th July 2024

DOI: 10.1039/d4nr01577k

rsc.li/nanoscale

Over the past two decades, significant progress in two-dimensional (2D) materials has invigorated research in condensed matter and material physics in low dimensions. While traditionally studied in three-dimensional systems, magnetism has now been extended to the 2D realm. Recent breakthroughs in 2D magnetism have attracted substantial interest from the scientific community, owing to the stable magnetic order achievable in atomically thin layers of the van der Waals (vdW)-type layered magnetic materials. These advances offer an exciting platform for investigating related phenomena in low dimensions and hold promise for spintronic applications. Consequently, vdW magnetic materials with tunable magnetism have attracted significant attention. Specifically, antiferromagnetic metal thiophosphates MPX_3 (M = transition metal, P = phosphorus, X = chalcogen) have been investigated extensively. These materials exhibit long-range magnetic order spanning from bulk to the 2D limit. The magnetism in MPX_3 arises from localized moments associated with transition metal ions, making it tunable *via* substitutions and intercalations. In this review, we focus on such tuning by providing a comprehensive summary of various metal- and chalcogen-substitution and intercalation studies, along with the mechanism of magnetism modulation, and a perspective on the development of this emergent material family.

1. Introduction

Since the discovery of graphene,[1] numerous two-dimensional (2D) materials have been theoretically predicted and experimentally realized. For a long time, 2D material research was mainly centralized around graphene and transition metal dichalcogenides (TMDs) in terms of their electronic properties

Rabindra Basnet

Dr Rabindra Basnet is currently a postdoctoral scholar in the Department of Chemistry and Physics at the University of Arkansas at Pine Bluff (UAPB). His research focuses on the synthesis and characterization (structural, electronic, magnetic, and thermodynamic properties) of a wide range of quantum materials including magnetic, topological, strongly correlated materials, and superconductors. He received a MS degree in Physics from Tribhuvan University, Nepal in 2016 and a Ph.D. in Physics from the University of Arkansas in 2023 before starting his current postdoc position at UAPB.

Jin Hu

Dr Jin Hu is currently an associate professor in the Department of Physics at the University of Arkansas. His research focuses on discovering novel materials with exotic properties or advanced functionalities, and understanding the physics behind the properties. He received a BS degree in Applied Physics from the University of Science and Technology of China in 2008, and a Ph.D. in Physics from Tulane University in 2013. He established the Quantum Material Research group at the University of Arkansas in 2017, and has been awarded the DOE Early Career Award and the NSF Career award.

---

[a] Department of Chemistry & Physics, University of Arkansas at Pine Bluff, Pine Bluff, AR, 71603 USA. E-mail: basnetr@uapb.edu
[b] Department of Physics, University of Arkansas, Fayetteville, Arkansas 72701, USA
[c] Materials Science and Engineering Program, Institute for Nanoscience and Engineering, University of Arkansas, Fayetteville, Arkansas 72701, USA. E-mail: jinhu@uark.edu

because they display almost all functionalities of solid-state systems such as metal, semimetal, semiconductor, and insulator as well as exotic quantum phases and phenomena such as superconductivity, charge density wave, and topological quantum phases. In addition to these properties, magnetism in 2D materials has also attracted intensive attention due to fundamental scientific interest in low dimensional orders and technological demands such as spintronics. Graphene[2] and TMDs[3–5] have been found to exhibit magnetism. However, owing to the non/weak-magnetic nature of the constituted atoms/ions, magnetism in these materials mainly arises from extrinsic factors such as defects or doping of guest atoms. Therefore, there has been an intensive search for 2D materials with intrinsic magnetism. Recently, there have been breakthroughs in discovering intrinsic magnetic orders in atomically thin layers of $FePS_3$,[6] CrI_3,[7] $CrGeTe_3$,[8] $CrBr_3$,[9] VI_3,[10] Fe_3GeTe_2 [11] and Fe_3GaTe_2,[12] which greatly expand the realm of the 2D magnetism and provide material platforms not only for gaining deep insight into low dimensional magnetism but also for spintronic applications.[13–25] These developments have motivated the search for additional novel magnetic van der Waals (vdW) materials, resulting in a blossoming of magnetic vdW materials that can be broadly categorized into two groups: (1) transition metal halides (including both dihalides and trihalides), and (2) transition metal chalcogenides (both binary and ternary) involving transition metals from V to Ni in the periodic table (*i.e.*, V, Cr, Mn, Fe, Co, and Ni). Magnetism in those vdW magnets arises from the magnetic moment of the 3d electrons of the transition metal cations. The metal ions in these compounds are mostly arranged in honeycomb lattices, except for a few compounds such as transition metal dihalides that is characterized by triangular networks of metal ions.[26]

Metal thiophosphates are some of the model systems among various 2D magnetic materials. Those materials were discovered in the late 1800s,[27,28] usually represented by a chemical formula of MPX_3 or $M_2P_2X_6$, where M, P, and X denote transition metal, phosphorus, and chalcogen elements, respectively. Since their discovery, MPX_3 compounds have been studied in various fields including magnetism,[6,29–43] magneto-optics,[44–50] optoelectronics,[27,28,51–53] Li-ion batteries,[27,28,54,55] and ferroelectricity.[27,28,56–59]Their layered structures allow for mechanical exfoliations down to atomically thin layers,[6,29,41–43,60] creating pathways to study 2D physics. The magnetic members of the MPX_3 (M = V, Cr, Mn, Fe, Co, and Ni) family are antiferromagnets in which the M ions carry localized magnetic moments in a layered honeycomb lattice. Antiferromagnetic (AFM) orders have been found to persist down to atomically thin layers and even to the monolayer limit in some MPX_3,[6,42,43] thus these materials have been established as important candidates for 2D magnets.[6,29,41–43,60] The MPX_3 compounds exhibit semiconducting[61] or insulating[62,63] behavior with band gaps ranging from 1.3 to 3.5 eV. Interestingly, applying high pressure can induce insulator-to-metal transitions[64–71] and even superconductivity[72] in some MPX_3 compounds. Furthermore, these compounds also offer platforms to study correlated electrons in 2D magnetic materials.[45,64,73] Recent studies have revealed a strong coupling between optically active excitons and magnetism in MPX_3.[44–49] For example, in $NiPS_3$, a novel coherent spin–orbit entangled excitonic state stabilized by AFM order[44] as well as the correlation between emitted photon and spins[45] have been reported. Such coupling can lead to an all-optical control of magnetic anisotropy.[50] In addition, a strong correlation of magnons and phonons that generates phonon spin through the transfer of spin angular momentum has been demonstrated in $FePS_3$.[42,74] Such intertwined degrees of freedom provide a unique opportunity to explore the interplay between magnetism, strong correlation, and light–matter interactions in 2D magnets.

In addition to fundamental research, this material family also offers a large material pool for potential technological applications. The feasibility of obtaining atomically thin layers enables nanodevices and heterostructures fabrication and integration, opening opportunities for utilization in electronics and spintronics. Moreover, in MPX_3, the band gaps ranging from 1.3 to 3.5 eV cover near-infrared to the UV region, enabling the optoelectronic applications in a broad wavelength horizon.[27,28] Additionally, the unusual intercalation–reduction behavior and higher ionic conductivity of these materials facilitate potential applications in Li-ion batteries.[27,28,54,55] Furthermore, their unusual ferroelectricity could lead to new energy and data storage devices and sensors.[27,28]

Given such versatility, MPX_3 materials have recently gained intensive attention. In particular, magnetism in those materials has been established as an important research topic.[75] The magnetic properties in MPX_3 strongly depend on the choice of the transition metal M and chalcogen X elements. Not only the AFM transition temperature (Néel temperature, T_N) that changes upon substituting M and X,[30–39] but also various AFM structures can be obtained through M[76–93] and X[30–32,94,95] substitutions. Such tuning of magnetism by altering M and X has led to the study of a series of polymetallic[76–93] and polychalcogenide[30–32,94,95] "mixed" MPX_3 compounds. Tunable magnetism has been observed in these mixed compounds, providing promising candidates to explore novel phenomena originating from 2D magnetism. In addition to substitution, the layered structure of MPX_3 allows for another doping strategy *i.e.*, the inter-layer intercalation of guest ions. Intercalating various guest species has been reported to cause AFM to ferrimagnetic (FIM)[96–100] and ferromagnetic (FM)[101] transitions in MPX_3. This suggests that the intercalation could be a promising route to achieve additional magnetic phases in MPX_3 that may not be accessible by substitution.

Thus far, a wide range of magnetic, electronic, vibrational, optical, and ferroelectric properties of pristine MPX_3 compounds have already been summarized by a few excellent review articles.[27,28,75] Therefore, the focus of this review will be put on engineering magnetic properties through various doping strategies: metal substitution, chalcogen substitution, and inter-layer intercalation, aiming to provide a comprehensive summary with sufficient depth and width for deeper understanding of magnetism in MPX_3 based on magnetic exchanges and anisotropies. This review is organized as follows: summarizing the crystal growth methods and lattice structures, an overall theoretical framework for understanding magnetism in MPX_3, experimental efforts in engineering the magnetism, and the perspective of the development of this field. We hope this review can provide the community with comprehensive information on the existing discoveries in doping studies and an in-depth understanding of magnetism, which serves as an important guideline for further exploring the exciting materials physics in MPX_3 as well as other 2D magnets and their property tuning. We wish to cover all relevant studies in this review. However, given the rapid development of MPX_3 materials, the emerging new discoveries may not be included but can be introduced by future review articles.

2. Crystal growth

The studies on functional materials, their properties, and applications, greatly rely on the development of convenient and reliable synthesis methods to produce high-quality crystals. For solid state systems, single crystals are highly desired because a single crystal possesses well-defined crystalline axes so that the intrinsic anisotropic magnetic, electronic transport and optical properties can be experimentally determined, which are critical to understanding the fundamental physics principles that govern the material properties. In addition, well-defined surfaces and edges of a single crystal enables the surface-sensitive measurements such as angle resolved photoemission spectroscopy (ARPES), scanning tunneling microscopy/spectroscopy (STM/S), *etc.* which provide valuable information. Conventional single-crystal synthesis techniques include chemical vapor transport (CVT), flux, Bridgman, floating zone (FZ), and Czocharalski methods. The synthesis of MPX_3 compounds goes back to the late 19th century when Friedel obtained $FePS_3$ by heating a weighed amount of phosphorus pentasulfide with iron.[27,28] This technique was later used by Ferrand[27,28] to synthesize other sibling compounds $ZnPS_3$, $CdPS_3$, and $NiPS_3$. Nowadays, CVT and flux have become the main techniques to grow the bulk single crystals of MPX_3, which have proven to be effective methods to yield large single crystals for physical characterizations.

A CVT method has been widely used to synthesize pristine, metal-, and chalcogen-substituted MPX_3 compounds as summarized in Table 1. As shown in Fig. 1(a), this method is based on the vaporization of source materials at the hot end of the growth chamber (usually a quartz ampoule), transportation of the vapor along some temperature gradient, and condensation of vapor at the cold end. For MPX_3, a mixture of elementary powders of M, P, and X, or pre-synthesized polycrystal precursors prepared by solid-state reaction, can be used as source materials for CVT. For CVT growth, a transport agent such as I_2, $TeCl_4$, $SeCl_4$, *etc.*, is usually added to the source material to aid the vapor transportation process. For MPX_3, CVT growth using these transport agents has been reported.[31,40,71,87–91,102–106] On the other hand, owing to the volatile elements P and S or Se, CVT growth without a transport agent[33,41,107–112] has also been successfully used to synthesize the single crystals of MPX_3. Experimentally, the source materials (elementary powders with proper molar ratio or pre-reacted polycrystal precursors) along with the transport agent (if used) are sealed in an evacuated quartz ampoule. The ampoule should be sufficiently long (usually ∼10–15 cm) to create a proper temperature gradient between the source and sink to facilitate the vapor transport. Then, the ampoule is placed in a two-zone furnace [Fig. 1(a)] which provides the needed temperatures and temperature gradient and heated at a certain duration required for the formation of the desired MPX_3 phase. The source end is kept at a higher temperature (T_{hot}) than the sink end (T_{cold}) to establish the thermal gradient, as summarized in Table 1. The heating process must be slow to avoid excessive pressure due to volatile elements P and X. Upon the completion of the growth, the furnace either slowly cools at a controlled slow cooling rate or naturally cools to room temperature, and single crystals can be found at the cold end. Single crystals harvested by quenching in ice water (*i.e.*, very rapid cooling) have also been reported.[113] The optical images of single crystals of some pristine and substituted (both metal- and chalcogen-substituted) MPX_3 compounds synthesized using the CVT technique are shown in Fig. 1(b–d).

In addition to CVT, the reactive flux technique has been recently reported to synthesize pristine and metal-substituted MPX_3 single crystals. This method adopts P_2X_5 (X = S[114–118] or Se[119]) flux and metal precursors, as summarized in Table 1. First, the metal and P_2X_5 powders in a ratio of 2 : 3 for mono-metallic or 1 : 1 : 3 for bimetallic compounds is sealed in an evacuated silica tube inside a glove box. The mixture is then heated and maintained at a certain temperature with different heating profiles depending on the target compounds.[115] The excess P_2S_5 (melting point ∼285 °C)[114–118] and P_2Se_5 (melting point ∼214 °C)[119] act as a reactive flux that oxidizes the metal element and enhances solubility to reduce reaction times and increase crystallite sizes. Upon the completion of the growth, the excess P_2S_5 flux is then removed with a 1 : 1 mixture of ethanol and water followed by a subsequent treatment using deionized water and acetone.[114–118] On the other hand, the excess P_2Se_5 flux is removed by the distillation process at a temperature gradient between 400 °C and room temperature.[119] This method can result in sizable single crystals in a relatively shorter synthesis time as compared to a traditional CVT technique, as shown in Fig. 1(e).

3. Crystal structure

The crystal lattice structures and symmetries are critical in determining magnetic properties, as has been theoretically predicted for MPX_3.[120] Varying lattice parameters have been found to strongly affect the magnetic properties.[120] So, under-

Table 1 Summary of crystal growth of MPX_3 compounds

Materials	Growth method	Temperature (°C)		Duration (days)	Ref.
		T_{hot}	T_{cold}		
VPS_3	CVT	600	500–350	7–30	71 and 106
$MnPS_3$	CVT	780–650	720–600	7	31, 41, 87, 104 and 238
	P_2S_5 flux	650	—	2	115
$FePS_3$	CVT	750–700	730–600	9–21	6, 72, 88, 91, 104, 107 and 239
	P_2S_5 flux	650	—	3	114–116
$CoPS_3$	CVT	600	550–500	7–8	108 and 240
	P_2S_5 flux	580	—	2	114–116
$NiPS_3$	CVT	760–670	690–550	7–21	31, 88, 89, 91 and 123
	P_2S_5 flux	650	—	2	115
$ZnPS_3$	CVT	600	550	7	151
	P_2S_5 flux	650	—	2	115
$CdPS_3$	CVT	630	600	5	104
	P_2S_5 flux	650	—	2	115
$MgPS_3$	CVT	670	550–800	90	124
	P_2S_5 flux	650	—	2	115
$PdPS_3$		500	450–500	7	124
$SnPS_3$		630	600	3–5	104 and 105
$HgPS_3$	CVT	350	320–500	3	124
	P_2S_5 flux	400	—	2	118
$PbPS_3$		650	620	3–5	105
$CrPSe_3$		800	700	10	103
$MnPSe_3$		650	600	7	31 and 241
$FePSe_3$		720–700	700–600	7–10	72 and 242
$NiPSe_3$		530	500–560	90	124
$ZnPSe_3$		370	—	10	243
$CdPSe_3$		610	650–550	30	124
$MgPSe_3$		620	480–690	90	124
$HgPSe_3$		400	300	5	244
$PbPSe_3$		750	710	3–5	105
$CuCrP_2S_6$		750–720	700–680	5–8	153 and 154
$CuInP_2S_6$	CVT	800	700	7	245
	P_2S_5 flux	650	—	4	115
$AgCrP_2S_6$		750	690	5	156
$AgInP_2S_6$		750–680	610–600	7–9	246 and 247
$Mn_{1-x}Fe_xPS_3$		730	700–630	5	81
$Fe_{1-x}Ni_xPS_3$		760–700	690–600	9	88 and 91
$Ni_{1-x}Mn_xPS_3$		750–720	670–550	7–12	87, 89 and 152
$Mn_{1-x}Co_xPS_3$	P_2S_5 flux	540	—	3	117
$Fe_{1-x}Co_xPS_3$	P_2S_5 flux	580	—	4	114–116
$Ni_{1-x}Co_xPS_3$		625	550	21	90
$Ni_{1-x}Cr_xPS_3$		750	550	7	177
$Mn_{1-x}Zn_xPS_3$		700–650	680–600	7	77, 78, 85 and 151
$Fe_{1-x}Zn_xPS_3$		700	650	7	93
$Fe_{1-x}Cu_xPS_3$		597	577	15	187
$Fe_{1-x}Cd_xPS_3$					
$Mn_{1-x}Fe_xPSe_3$		750	550	7	122
(Mn,Fe,Ni,Co)PS_3		650	-	18	113
(V,Mn,Fe,Ni,Co)PS_3		610	-	3	113
(Zn,Mn,Fe,Ni,Co)PS_3		610	-	3	113
(Mg,Mn,Fe,Ni,Co)PS_3		610	-	3	113
(Fe,Mn,Cd,In)PSe_3		627	377	7	121
$Cu_xNi_{2(1-x)}Cr_xP_2S_6$		750	550	7	181
$MnPS_{3-x}Se_x$		650	600	7	31 and 32
$NiPS_{3-x}Se_x$		750	550	7	31
$FePS_{3-x}Se_x$		750	550	7	122

standing crystal structure is essential for gaining deeper insights into magnetism. At first glance, all MPX_3 materials exhibit very similar layered structures [Fig. 2(a)]. Careful structure characterizations have revealed monoclinic, rhombohedral, and triclinic structures for various MPX_3, as summarized in Table 2. Despite three different lattice structures, MPX_3 materials exhibit common structural characteristics. As shown in Fig. 2(b), metal atoms M are arranged in a honeycomb lattice. Each P displays a tetrahedral coordination, which is covalently bonded with one P to form P–P (P_2) dimers perpendicular to the hexagonal plane and three X featuring a $(P_2X_6)^{4-}$ bipyramid structure unit. Such P–P dimer forming $(P_2X_6)^{4-}$ bipyramids fill the center of the M honeycomb lattice. Therefore, these compounds have also been referred to as

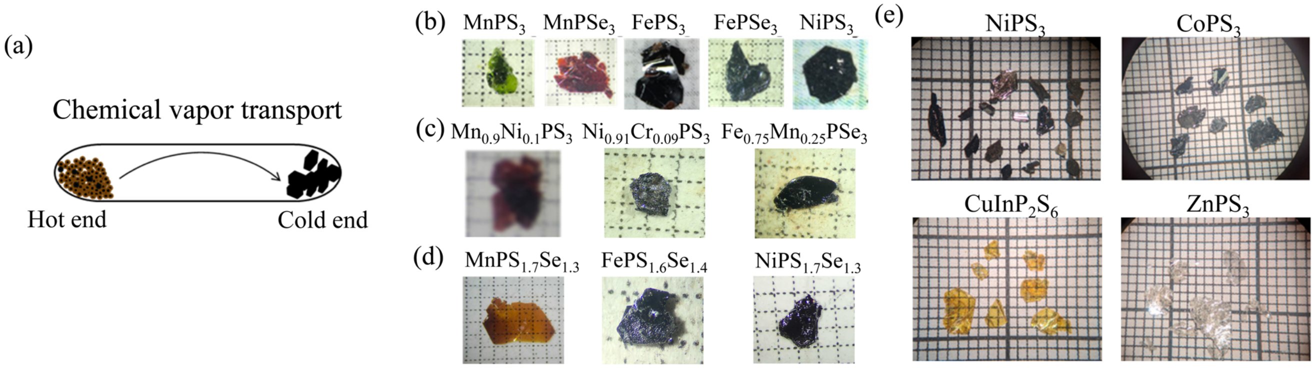

Fig. 1 Crystal growth of MPX_3. (a) Schematic of chemical vapor transport (CVT) growth. Optical microscope images of (b) pristine, (c) metal (M)-, (d) chalcogen (X)-substituted MPX_3 single crystals synthesized by CVT methods. (e) Optical images of single crystals of MPX_3 compounds synthesized by using the reactive P_2S_5 flux method. Reprinted (adapted) with permission.[115] Copyright 2021, American Chemical Society.

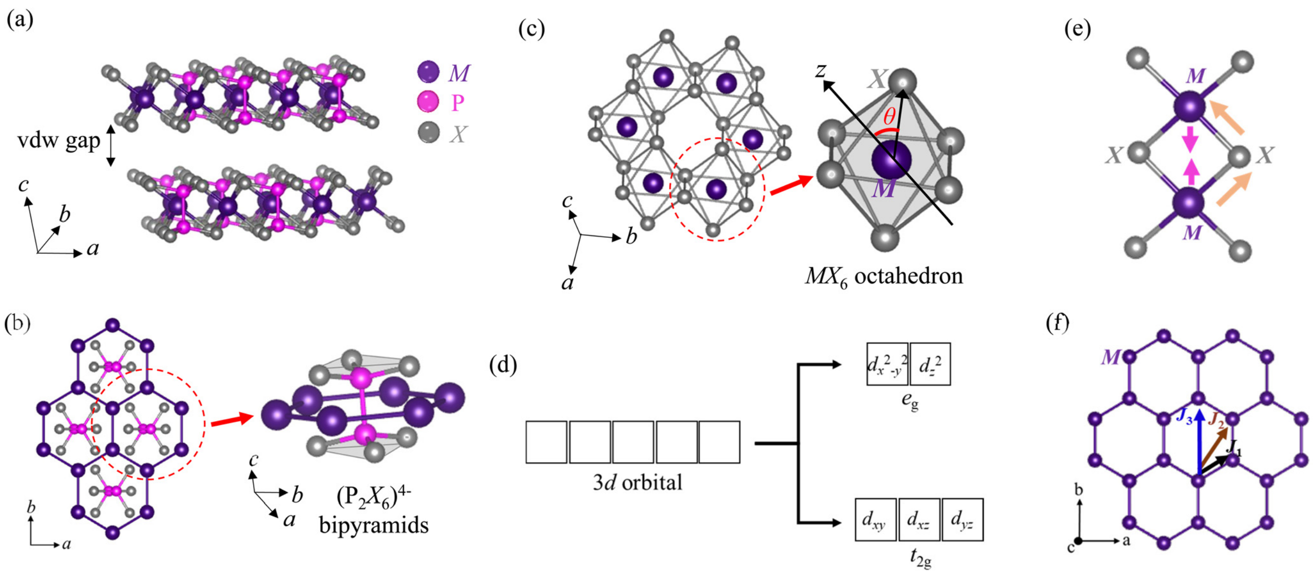

Fig. 2 Crystal structures of MPX_3. (a) The layered structure of van der Waals material MPX_3. (b) The $(P_2X_6)^{4-}$ (X = S or Se) anion sublattice in each layer. Metal M is arranged in a honeycomb lattice around the $(P_2X_6)^{4-}$ bipyramids. (c) MX_6 octahedron of MPX_3. Such MX_6 octahedra possesses a trigonal distortion that is characterized by the angle θ between the trigonal axis (perpendicular to the *ab*-plane) and the M–X bond. (d) Splitting of five 3d orbitals of transition metal cations into three t_{2g} and two e_g levels under an octahedral crystal field. (e) Schematic of direct exchange interaction between magnetic ions, and superexchange interactions between two cations through anion. (f) Schematic of nearest-neighbor (J_1), second nearest-neighbor (J_2), and third nearest-neighbor (J_3) interactions in MPX_3.

$M_2P_2X_6$ in the literature. For chalcogen atoms X that sandwich the metal honeycomb layer, they form almost close-packed surfaces of the layer with an array of octahedral coordinated sites [Fig. 2(c)]. The monolayer MPX_3 can be considered as the monolayer MX_2 where the one-third of M sites are substituted by P–P dimers. Thus, in MPX_3, two-thirds of the octahedral centers are filled by M^{2+} cations while the P–P dimers occupy the remaining one-third [Fig. 2(c), P–P dimer in the center is not shown].

As seen in Fig. 2(a), a finite vdW gap of about 3.22–3.24 Å is present in MPX_3.[27,28,75] Various metal ions M^{2+} with different ionic radii slightly modify the slab size. The two flat pyramids formed by bonding between a P and three X atoms at the top and bottom of the $(P_2X_6)^{4-}$ structural unit [shown in Fig. 2(b)] remain invariable, but the P–P distance is slightly adjusted to accommodate the changes in metal cations. For example, the P–P distance elongates from 2.148 Å in $NiPS_3$ to 2.222 Å in $CdPS_3$,[27] which is accompanied by increases of the layer thickness.

Although the individual lamella is similar for all MPX_3 compounds, their symmetry, and layer stacking to form a bulk lattice structure can vary depending on M and X, as summarized in Table 2. In particular, the symmetries and crystal structures for sulfides and selenides of MPX_3 materials are distinct. Generally, almost all the known sulfides MPS_3 exhibit monoclinic crystal structures with a *C*2/*m* space group, except for

Table 2 Crystal structures of MPX_3 compounds

Materials	Crystal structure	Space group	Ref.
VPS_3	Monoclinic	$C2/m$	71 and 106
$MnPS_3$	Monoclinic	$C2/m$	31, 41, 87, 104 and 238
$FePS_3$	Monoclinic	$C2/m$	6, 72, 88, 91, 104, 107 and 239
$CoPS_3$	Monoclinic	$C2/m$	108, 240
$NiPS_3$	Monoclinic	$C2/m$	31, 88, 89, 91 and 123
$ZnPS_3$	Monoclinic	$C2/m$	151
$CdPS_3$	Monoclinic	$C2/m$	104
$MgPS_3$	Monoclinic	$C2/m$	124
$PdPS_3$	Monoclinic	$C2/m$	124
$SnPS_3$	Monoclinic	$C2/m$	104 and 105
$HgPS_3$	Triclinic	$P\bar{1}$	124
$PbPS_3$	Monoclinic	$P21/c$	105
$CrPSe_3$	Monoclinic	$C2/m$	103
$MnPSe_3$	Rhombohedral	$R\bar{3}$	31 and 241
$FePSe_3$	Rhombohedral	$R\bar{3}$	72 and 242
$NiPSe_3$	Monoclinic	$C2/m$	124
$ZnPSe_3$	Rhombohedral	$R\bar{3}$	243
$CdPSe_3$	Rhombohedral	$R\bar{3}$	124
$MgPSe_3$	Rhombohedral	$R\bar{3}$	124
$HgPSe_3$	Monoclinic	$C2/m$	244
$PbPSe_3$	Monoclinic	$P21/c$	105
$CuCrP_2S_6$	Monoclinic	C2/c	153 and 154
$CuInP_2S_6$	Trigonal	$P\bar{3}1c$	245
$AgCrP_2S_6$	Monoclinic	$P2/a$	156
$AgInP_2S_6$	Trigonal	$P31c$	246 and 247
$Mn_{1-x}Fe_xPS_3$	Monoclinic	$C2/m$	81
$Fe_{1-x}Ni_xPS_3$	Monoclinic	$C2/m$	88
$Ni_{1-x}Mn_xPS_3$	Monoclinic	$C2/m$	87, 89 and 152
$Mn_{1-x}Co_xPS_3$	Monoclinic	$C2/m$	117
$Fe_{1-x}Co_xPS_3$	Monoclinic	$C2/m$	114–116
$Ni_{1-x}Co_xPS_3$	Monoclinic	$C2/m$	90
$Ni_{1-x}Cr_xPS_3$	Monoclinic	$C2/m$	177
$Mn_{1-x}Zn_xPS_3$	Monoclinic	$C2/m$	151
$Fe_{1-x}Zn_xPS_3$	Monoclinic	$C2/m$	93
$Mn_{1-x}Fe_xPSe_3$	Rhombohedral	$R\bar{3}$	86
$(Mn,Fe,Ni,Co)PS_3$	Monoclinic	$C2/m$	113
$(V,Mn,Fe,Ni,Co)PS_3$	Monoclinic	$C2/m$	113
$(Zn,Mn,Fe,Ni,Co)PS_3$	Monoclinic	$C2/m$	113
$(Mg,Mn,Fe,Ni,Co)PS_3$	Monoclinic	$C2/m$	113
$(Fe,Mn,Cd,In)PSe_3$	Rhombohedral	$R\bar{3}$	121
$Cu_xNi_{2(1-x)}Cr_xP_2S_6$	Monoclinic	$C2/m$	181
$MnPS_{3-x}Se_x$	Mono → Rhom	$C2/m \rightarrow R\bar{3}$	32
$NiPS_{3-x}Se_x$	Monoclinic	$C2/m$	31
$FePS_{3-x}Se_x$	Mono → Rhom	$C2/m \rightarrow R\bar{3}$	122

$PbPS_3$[105] which has been reported to crystalize in a $P21/c$ monoclinic structure as its selenide counterpart, and for $HgPS_3$[118] which is triclinic with a $P\bar{1}$ space group symmetry. In sulfides, the monoclinic angle β depends on the metal cation, ranging from 106.97° for $MgPS_3$ to 107.35° for $MnPS_3$. On the other hand, as summarized in Table 2, selenides $MPSe_3$ process larger P–Se bond lengths and Se–P–Se bond angles as compared to their sulfide counterparts, and mostly crystallize in rhombohedral structures with a $R\bar{3}$ space group. The exceptions are $NiPSe_3$, $CrPSe_3$, $HgPSe_3$, and $PbPSe_3$ which exhibit monoclinic crystal structures.

Therefore, the lattice structure of MPX_3 appears to be more sensitive to chalcogen rather than metal. This is further confirmed by substitution studies. As summarized in Table 2, substituting metal atoms M does not change the lattice structure in MPX_3.[76–92,114,116,117] Most known metal-substituted sulfide compounds exhibit monoclinic structure with a $C2/m$ space group in the entire substitutional range. For selenides, previous works on a bimetallic compound $Mn_{1-x}Fe_xPSe_3$ [86] and a high entropy compound $Fe_{1-x-y-z}Mn_xCd_yIn_zSe_3$ [121] also found unchanged lattice with rhombohedral $R\bar{3}$ structures. On the other hand, chalcogen S–Se substitution can induce structure transition from monoclinic ($C2/m$) to rhombohedral ($R\bar{3}$) in $MnPS_{3-x}Se_x$ [32] and $FePS_{3-x}Se_x$,[122] which is consistent with the different lattice structures for their sulfide and selenide end compounds. One exception is $NiPS_{3-x}Se_x$ which displays unchanged monoclinic $C2/m$ structure, which is also in line with the identical $C2/m$ space group for $NiPS_3$ [31,88,89,91,123] and $NiPSe_3$ [124].

4. Magnetism

4.1. Theoretical background

Owing to the insulating nature of MPX_3 compounds, their magnetism can be described by local moment pictures. Magnetism in vdW magnetic materials arises from the magnetic moment of the spin and orbital momenta of the 3d electrons of the transition metal cations. Thus, the choice of transition metal cations plays a vital role in determining magnetism. In the presence of a crystal electric field from the octahedral coordination of the transition metal cations [Fig. 2(c)], the $d_{x^2-y^2}$ and d_{z^2} orbitals among the five d-orbitals of the transition metal point in the direction of the ligands, thereby the electrons in these orbitals experience greater repulsion with ligands and increase the energy of these orbitals. Thus, these two d-orbitals are pushed to higher energy levels in the band structure and referred to as two-fold degenerate high-energy e_g orbitals. On the other hand, the remaining three d-orbitals d_{xz}, d_{yz}, and d_{xy} do not directly align towards ligands leading to a weaker repulsion and stabilized to a lower energy level than two e_g orbitals. Therefore, these three orbitals lie below e_g orbitals ($d_{x^2-y^2}$ and d_{z^2}) in term of energy and constitute three-fold degenerate low-energy t_{2g} orbitals.[125,126] The splitting of five 3d orbitals of transition metal ions under an octahedral crystal field is depicted in the schematic in Fig. 2(d). Then, the d electrons of various transition metal cations fill these orbitals following Hund's rule, as presented in Table 3.[127] The occupancy of these orbitals determines the total magnetic moment of the 3d transition metal cations, with the total magnetic moment given by $g_J[j(j+1)]^{1/2}\mu_B$ where $|j|$, g_J, and μ_B are the total angular momentum quantum number (= spin + orbital angular momentum), Landé g-factor, and Bohr magneton, respectively. When orbital angular momentum is quenched (*i.e.*, $L = 0$), only the spin magnetic moment contributes to the total magnetic moment, resulting in a total magnetic moment of $2[s(s+1)]^{1/2}\mu_B$ where s is the total spin quantum number, which is generally the case for transition metals.[125]

In the classic Heisenberg model, the magnetism can be explained within the framework of isotropic Heisenberg

Table 3 Orbital occupancy for 3d valence electrons of various transition metal cations under octahedral crystal field

Transition metal ions	3d orbital occupancy
V^{2+} ($3d^3$)	e_g ↑ ↑ t_{2g} ↑ ↑ ↑
V^{3+} ($3d^2$)	e_g ↑ ↑ t_{2g} ↑ ↑ ↑
Cr^{2+} ($3d^4$)	e_g ↑ ↑ t_{2g} ↑ ↑ ↑
Cr^{3+} ($3d^3$)	e_g ↑ ↑ t_{2g} ↑ ↑ ↑
Mn^{2+}($3d^5$)	e_g ↑ ↑ t_{2g} ↑ ↑ ↑
Fe^{2+} ($3d^6$)	e_g ↑ ↑ t_{2g} ↑↓ ↑ ↑
Fe^{3+} ($3d^5$)	e_g ↑ ↑ t_{2g} ↑ ↑ ↑
Co^{2+} ($3d^7$)	e_g ↑ ↑ t_{2g} ↑↓ ↑↓ ↑
Ni^{2+} ($3d^8$)	e_g ↑ ↑ t_{2g} ↑↓ ↑↓ ↑↓

Hamiltonian: $H = -2\Sigma(JS_i\cdot S_j)$, where J is the exchange coupling, which is considered to be isotropic, the summation is over all pairs of magnetic ions in the lattice and the spins are treated as three-component vectors where S_i and S_j are spin magnetic moments of the atomic site i and j respectively. The Heisenberg model provides an accurate account of the interactions between the localized magnetic moments that govern the magnetic properties in insulators (such as MPX_3). In vdW materials, magnetic interactions can be anisotropic and are described by a Heisenberg Hamiltonian with anisotropic exchange: $H = -2\Sigma(J_xS_iS_j + J_yS_iS_j + J_zS_iS_j)$, where J_x, J_y, and J_z are exchange couplings along the crystallographic axes. In layered MPX_3, magnetic exchanges within the layer are much stronger than inter-layer interactions,[128–130] hence the long-range magnetic ordering is believed to be mainly governed by intralayer exchange interactions. The interactions between localized moments in insulating MPX_3 compounds are mainly mediated through direct and superexchange interactions, as shown in Fig. 2(e). The direct exchanges between neighboring magnetic moments, which result from the overlapping wavefunctions, mainly depend on their spatial separation, and contribute to the nearest neighbor interaction J_1. Despite the fact that the distances between magnetic cations are large (in the order of 3–4 Å), such direct exchange has been found to be important or even dominate the magnetic interactions in some MPX_3 compounds such as $MnPS_3$.[128] On the other hand, in many other MPX_3 materials such as $NiPS_3$, the long-range magnetic coupling between moments is dominated by metal–chalcogen–metal (M–X–M) superexchange interactions mediated through non-magnetic chalcogen X.[128] The superexchange couplings contribute to both the nearest-neighbor interaction (J_1) and the interactions between further neighbors such as second nearest-neighbor (J_2), and third nearest-neighbor (J_3) interactions.[128] The magnetic interactions J_1, J_2, and J_3 are depicted in Fig. 2(f). The nature and strength of superexchange interactions are determined by M–X–M bonding angle, d-orbital occupancy of M^{2+} ions, and orbital overlap between M^{2+} cation and X^{2-} anion:[40,128] According to Goodenough–Kanamori rules,[131,132] the superexchange interaction is ferromagnetic (FM) if M–X–M bond angle is close to 90° and AFM when M–X–M bond angle is 180°. The occupancy of d orbitals is important. For example, $CoPS_3$ and $NiPS_3$ share the same magnetic structure but possess different strengths for superexchange due to their distinct occupancy of d orbitals for Co^{2+} (d^7) and Ni^{2+} (d^8) ions.[129] Such differences could be important in designing different strategies to tune magnetism in $CoPS_3$ and $NiPS_3$. The overlap of atomic orbitals also affects the superexchange interaction. Usually, stronger orbital overlap strengthens the superexchange, therefore substituting Se for S in MPX_3 leads to enhanced superexchange because of the extended orbital overlap due to more extended atom orbitals of Se than S.[31]

Furthermore, structural distortions also affect the magnetism in MPX_3.[40,128,129] As illustrated in Fig. 2(c) and mentioned above, every metal atom M in MPX_3 is located at the center of an octahedron formed by six X atoms. Such MX_6 octahedra, however, possess a trigonal distortion that is characterized by the angle θ between the trigonal axis (perpendicular to the *ab*-plane) and the M–X bond [Fig. 2(c)]. The experimental θ values for various MPX_3 compounds are presented in Table 4. An ideal octahedral possesses the ideal octahedral angle $\theta \approx 54.75°$. The deviation of θ angle from this ideal value characterizes the trigonal distortion. The crystal field arising from trigonal distortion of MX_6 octahedra together with spin–orbit coupling (SOC) of the M^{2+} cations introduce anisotropy in an otherwise isotropic system. Now, with an additional anisotropy term, the full Hamiltonian becomes $H = -2\sum(J_{ij}S_i\cdot S_j) - A\sum(S_i^z)^2$, where J_{ij} is exchange interaction between neighboring i^{th} and j^{th} moments and A is single-ion anisotropy parameter that defines the magnetic anisotropy of the system. The strengths of various *J's* and A determine the magnetism in MPX_3. Table 4 summarizes the experimental values of J and A parameters obtained by neutron scattering experiments for various MPX_3 materials,[35,94,107,128,129] together with theoretical calculated values for VPS_3.[133] These distinct J and A values for different MPX_3 compounds result in diverse AFM structures for this material family, as shown in Fig. 3. When $J \gg A$ (for very small A), the magnetism is weakly anisotropic and can be explained by the 3D isotropic Heisenberg Hamiltonian, such as $MnPS_3$.[35,40] For large A values, on the other hand, the magnetism becomes rather anisotropic and corresponds to XY

Table 4 Magnetic exchange and anisotropy parameters for MPX$_3$ materials. Here, negative and positive signs denote AFM and FM interactions, respectively. θ is defined as the angle between the z-axis and the vector that joins the metal M^{2+} ion and any particular nearest-neighbor chalcogen ligand [Fig. 3(e)]. Without trigonal distortion, θ becomes 54.7°

Parameters	VPS$_3$ [a] [133]	MnPS$_3$ [35]	FePS$_3$ [107]	CoPS$_3$ [129]	NiPS$_3$ [248]	MnPSe$_3$ [94]
S	3/2	5/2	2	3/2	1	5/2
T_N (K)	56 (ref. 106)	78	118	120	155	74
J_1 (meV)	−7.387	−0.77(9)	1.46(1)	2.04	1.9(1)	−0.45
J_2 (meV)	−0.068	−0.07(7)	−0.04(4)	0.26	−0.1(1)	−0.03
J_3 (meV)	−0.223	−0.18(1)	−0.96(5)	−4.21	−6.90(5)	−0.19
J_c (meV)	—	0.0019(2)	−0.0073(3)	—	0.32(3) (ref. 130)	−0.031(5)
A (meV)	—	0.0086(9)	2.66(8)	2.06	0.3(1)	—
θ (°)	—	51.67 (ref. 129)	51.28 (ref. 129)	51.38 (ref. 129)	51.05 (ref. 129)	—

[a] Theoretical study.

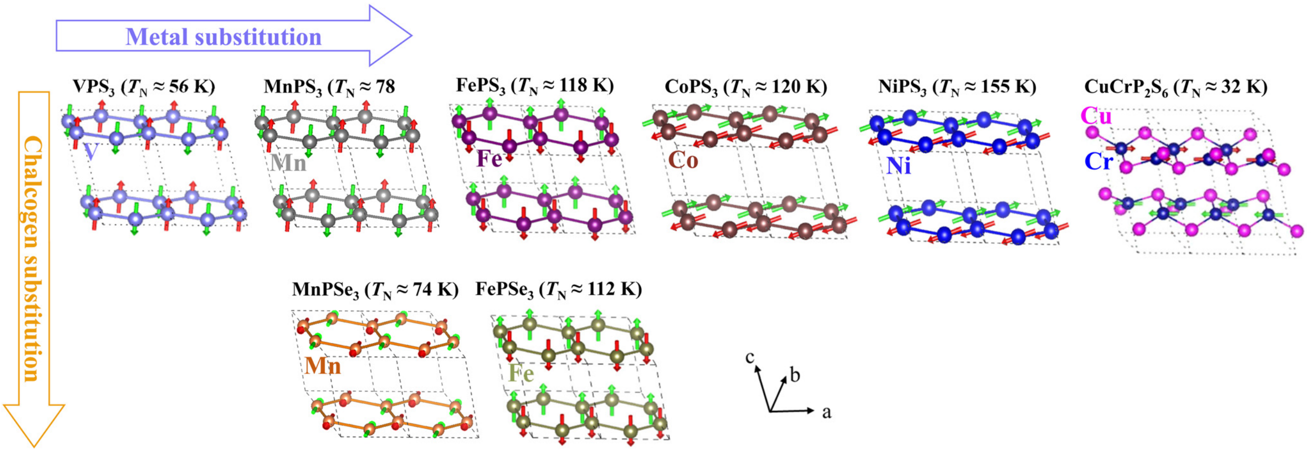

Fig. 3 Experimentally determined magnetic structures of various MPX$_3$ materials. For CuCrP$_2$S$_6$, the low-temperature structure is shown. Magnetic structures for (V,Co,Ni)PSe$_3$ and CuCrP$_2$Se$_6$ have not been experimentally determined.

(such as NiPS$_3$[40,123] and CoPS$_3$[129]) or Ising-type (such as FePS$_3$[40] and FePSe$_3$[30]) magnetism depending on the sign and magnitudes of A. In Mn and Ni systems, the orbital angular momentum (L) is quenched for Mn^{2+} (d^5) and Ni^{2+} (d^8) ions because of their half and fully-filled t$_{2g}$ orbitals respectively, leading to negligible SOC for magnetic ions.[40] In MnPS$_3$ which possesses relative weak trigonal distortion (octahedral angle $\theta \approx 51.67°$), the effect of both spin–orbit splitting and trigonal distortion is found to be negligible for the high spin ground state of Mn^{2+},[40] so the magnetism in MnPS$_3$ is governed by the dipolar anisotropy[35,134,135] which results in an out-of-plane moment orientation with a small tilt towards the a-axis (Fig. 3). On the other hand, NiPS$_3$ exhibits greater trigonal distortion characterized by octahedral angle, $\theta \approx 51.05°$ from the undistorted octahedral angle of 54.75°. This leads to remarkable single-ion anisotropy $A \approx 0.3$ meV in NiPS$_3$, which is much stronger than that of 0.0086 meV in MnPS$_3$ (Table 4).[35,128,129] Consequently, Ni moments are aligned within the basal plane perpendicular to the trigonal axis (Fig. 3),[36,40,135] and this system can be modeled by the anisotropic Heisenberg Hamiltonian with XY-type anisotropy. The situation is different for FePS$_3$, which exhibits a substantial magnetic anisotropy with a much higher A (≈2.66 meV) in comparison to MnPS$_3$ and NiPS$_3$.[107,128] Thus, FePS$_3$ is best described by the Ising Hamiltonian corresponding to the highly anisotropic Ising-type magnetic ordering with magnetic moments aligned along the out-of-plane direction.[40,107] In FePS$_3$, the degenerate t$_{2g}$ orbitals for the high-spin Fe^{2+} (d^6) state lead to a stronger trigonal distortion of the FeS$_6$ octahedra ($\theta \approx 51.28°$ (ref. 107 and 129)) that causes a significant splitting of t$_{2g}$ orbitals to lift the degeneracy while the e$_g$ orbitals remain doubly degenerate.[136] In addition, the lack of half- or fully-filled t$_{2g}$ orbitals for high-spin Fe^{2+} ions also contribute to the net orbital moment and consequently enhances the SOC. Although, a recent X-ray photoemission electron microscopy study has demonstrated that the spin–orbit entanglement for Fe^{2+} under trigonal elongation plays a key role behind the significant magnetic anisotropy in FePS$_3$,[137] the SOC alone may not be a dominant factor behind strong magnetic anisotropy in FePS$_3$ because the SOC for Ni^{2+} (d^8) ion is larger than Fe^{2+} (d^6) ion but the resulting compound NiPS$_3$ is less anisotropic than FePS$_3$.[40] The large crystal electric field arising from the strong trigonal distortion of the FeS$_6$ octahedra might also be attributed to a substantial magnetic anisotropy in FePS$_3$, which has been confirmed by a recent X-ray absorption spectroscopy experiment.[136] In fact, the strong anisotropy due to crystal electrical field *i.e.*, crystal-field anisotropy has been ascribed to Fe^{2+} (d^6) ion in different Fe-based compounds.[138,139]

4.2. Engineering magnetism in MPX_3

Engineering magnetism in layered magnetic materials not only optimizes properties for technological applications (such as high transition temperature, wider hysteresis loop, and various types of FM and AFM structures) but also provides an effective approach to clarify the mechanism for the magnetism by identifying the parameters that govern magnetism. Several strategies such as doping,[30–32,76–91,94,95,97–99,140–146] high pressure,[147–150] and electrostatic gating[14,16] have been adopted to tune the magnetic properties in layered magnets. These techniques have been successful in controlling the spin orientation in vdW magnetic materials, which leads to novel magnetic phenomenon arising from 2D magnetism. Tuning magnetic properties has been one major focus and studied for a long time in the MPX_3 family.[77,78,85] Doping, including metal M and chalcogen X substitutions, and inter-layer intercalation, has been demonstrated as a powerful technique to modulate magnetism in MPX_3, which will be the focus of this review as discussed below.

4.2.1. Metal (M) substitution. Metal substitution has been adopted as an important method to manipulate the magnetic properties in MPX_3. Owing to the structural similarity of the MPX_3 materials, a divalent metal M^{2+} ion can be substituted with another divalent metal ion to create a polymetallic "mixed" compound such as $(Mn,Ni)_xFe_{1-x}PS_3$, $Ni_{1-x}Mn_xPS_3$, $(Mn,Fe)_{1-x}Zn_xPS_3$, $(Mn,Fe,Ni)_{1-x}Co_xPS_3$ and $Mn_{1-x}Fe_xPSe_3$ [76–91,93,114,116,117,151,152] where two different metal atoms are mixed in a honeycomb lattice as shown in Fig. 4(a). In addition to these bimetallic substitutions, the metal substitution in MPX_3 has recently been extended to mixing of more than two divalent metal M^{2+} ions creating medium[121] and high entropy[113] vdW materials. In addition to these bi- and poly-metallic compounds based on isovalent M^{2+} ion substitutions, the non-isovalent substitution of monovalent and trivalent ions that leads to a series of quaternary compounds $(M_1)^{1+}(M_2)^{3+}P_2X_6$ (M_1 = Li, Cu, Ag, *etc.*; M_2 = V, Cr, In, Bi, *etc.*; X = S and Se)[119,153–161] have also been reported in this material family. Although the focus of this review is the divalent metal substitutions, we have also briefly summarized the magnetic properties of a few magnetic quaternary compounds $(Cu,Ag)^{1+}(V,Cr)^{3+}P_2(S,Se)_6$ that have been formed by mixing trivalent ions such as Cr^{3+} or V^{3+} with monovalent metal ions such as Cu^{1+} or Ag^{1+}.[153–157] The magnetic exchange J and single-ion anisotropy A parameters are found to be effectively modulated with metal substitutions that lead to efficient control of magnetic properties. Tunable magnetism arising from competing

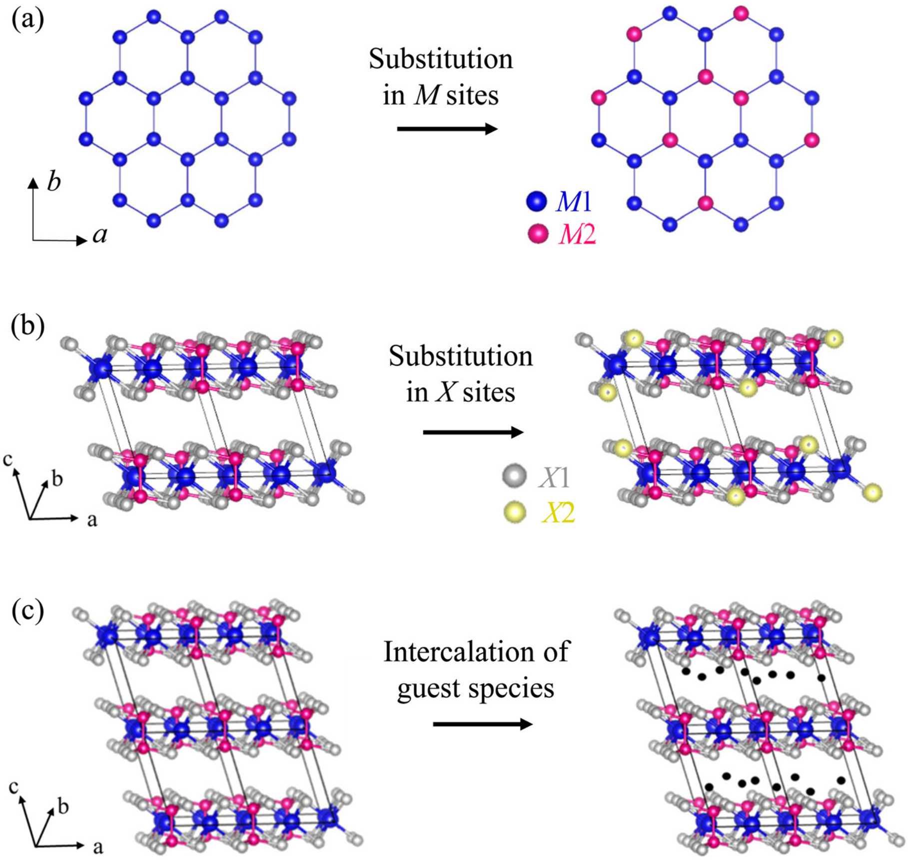

Fig. 4 Conceptual schematic of (a) metal (M) substitution, (b) chalcogen (X) substitution, and (c) Li intercalation in MPX_3.

magnetic interactions, magnetic anisotropies, and spin fluctuations has been observed in metal-substituted MPX_3 compounds, which will be discussed in the following sections.

4.2.1.1. Isovalent substitution

4.2.1.1.1. $Mn_{1-x}Fe_xPS_3$. As shown in Fig. 3, $MnPS_3$ and $FePS_3$ exhibit out-of-plane magnetic moment but different Néel[134] and zig-zag[107] type AFM structures for each layer, respectively. Therefore, the tuning of magnetic properties arising from the competition between two different AFM interactions is expected when Mn^{2+} and Fe^{2+} ions are mixed, which has been studied by Masubuchi *et al.*[81] Single crystals of $Mn_{1-x}Fe_xPS_3$ ($0 \leq x \leq 1$) were synthesized using a CVT technique as detailed in ref. 81.

As shown in Fig. 5, the magnetic properties were characterized by the temperature dependence of magnetization under various magnetic fields along the easy axis (the c^* axis in Fig. 5 is perpendicular to the *ab*-plane. *i.e.*, the out-of-plane direction).[81] A few magnetic phases have been identified: AFM order for $0 \leq x \leq 0.2$ and $0.8 \leq x \leq 1$ composition, which is characterized by a clear AFM transition in susceptibility without remarkable difference between zero-field-cooling (ZFC) and field-cooling (FC). A broad hump in susceptibility occurs above the AFM ordering temperature T_N in end compounds [Fig. 5(a)]. This is a generic feature in many MPX_3 compounds, which has been attributed to a short-range 2D or quasi-2D magnetic correlation owing to the layered structures. The broad hump is suppressed by substitution, leading to a sharper peak at T_N [Fig. 5(a)], which has been ascribed to the weakening of a short-range magnetic correlation due to randomness introduced by Fe substitution.

Samples in $0.5 \leq x \leq 0.6$ compositions display significant irreversibility [Fig. 5(b)] and are ascribed to a spin glass phase, which might be attributed to the competition between dominant exchange interactions in $MnPS_3$ and $FePS_3$ phases, namely AFM Mn^{2+}–Mn^{2+} J_1 interaction and FM Fe^{2+}–Fe^{2+} J_1 interaction, respectively[35,107] (Table 4). This is further confirmed by AC susceptibility.[81] The glass temperature, defined as the temperature where susceptibility displays irreversibility between ZFC and FC measurement, is found to enhance with the frequency in AC susceptibility measurements. The remaining composition regions, *i.e.*, $0.3 \leq x \leq 0.45$ and $0.6 < x \leq 0.7$, are characterized by an AFM-like transition without irreversibility at T_N. However, irreversibility occurs at a lower temperature. This has been ascribed by a reentrant spin glass transition [RSG in the phase diagram in Fig. 5(c)]. Considering equal Mn–Fe substitutions in both end compounds, the reentrant spin glass phase is found to be stronger towards Fe-rich compositions as compared to Mn-rich compositions, which is manifested by the higher reentrant spin glass transition temperature for $x = 0.7$ than $x = 0.3$.[81] Such behavior could stem from much larger single-ion anisotropy A for $FePS_3$ (Table 4) as compared to $MnPS_3$, as has been proposed in dilute alloys.[162]

Overall, $Mn_{1-x}Fe_xPS_3$ displays a non-monotonic doping dependence of T_N with a minimum of around $x \approx 0.5$. Such behavior is widely seen in other metal-substituted MPX_3 and is usually interpreted by spin frustration due to the mixing of two types of magnetic ions compounds ($MnPS_3$ and $FePS_3$) with significantly distinct magnetic exchange interactions J_1, J_2, and J_3 [35,107] as summarized in Table 4.

4.2.1.1.2. $Fe_{1-x}Ni_xPS_3$. For $Fe_{1-x}Ni_xPS_3$, the distinct XY- and Ising-like antiferromagnetism for the end members $NiPS_3$ and $FePS_3$ respectively makes it rather interesting to investigate the evolution between those two magnetic orders with distinct magnetic anisotropies.

$Fe_{1-x}Ni_xPS_3$ single crystals were grown using CVT with a temperature gradient from (760–700) to (690–600) °C for 200 hours.[88,91] The magnetic properties of $Fe_{1-x}Ni_xPS_3$ were characterized using temperature and field dependence of magnetization. Fig. 6(a) presents the temperature dependence of susceptibility ($\chi = M/H$) with the magnetic field of 1 T along *a*, *b*, and c^*. Here, c^* represents the direction that is perpendicular to the crystallographic *ab*-plane, which is slightly deviated from the crystallographic *c* axis in a monoclinic unit cell. For

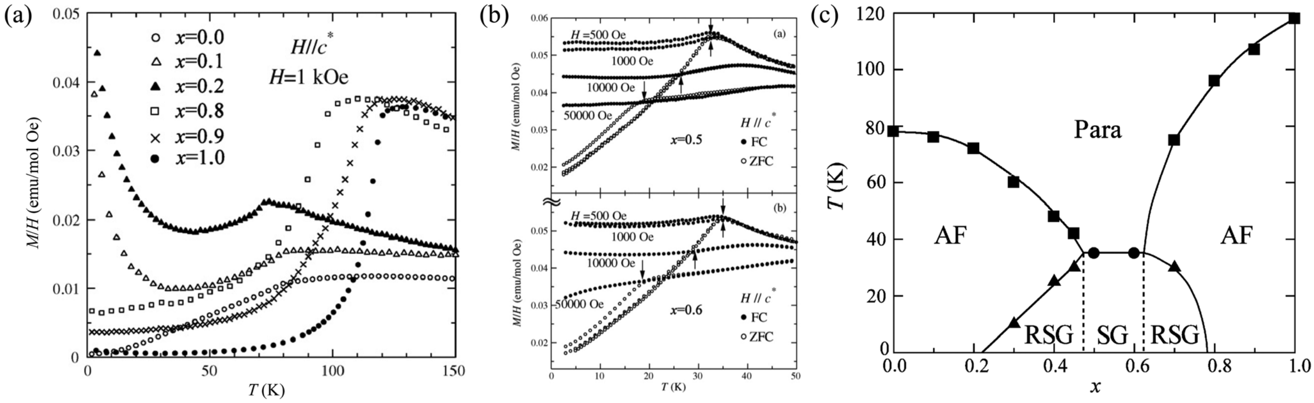

Fig. 5 (a and b) Temperature dependence of zero-field cooled (ZFC) susceptibility with the magnetic field applied parallel to the magnetic easy axis (c^*-axis) of $Mn_{1-x}Fe_xPS_3$ (x = 0.0, 0.1, 0.2, 0.8, 0.9, 1.0). (c) Magnetic phase diagram of the $Mn_{1-x}Fe_xPS_3$. SG, RSG, AF, and Para indicate a spin glass phase, a reentrant spin glass phase, an antiferromagnetic ordered phase, and a paramagnetic phase, respectively. Reprinted (adapted) with permission.[81] Copyright 2008, Elsevier.

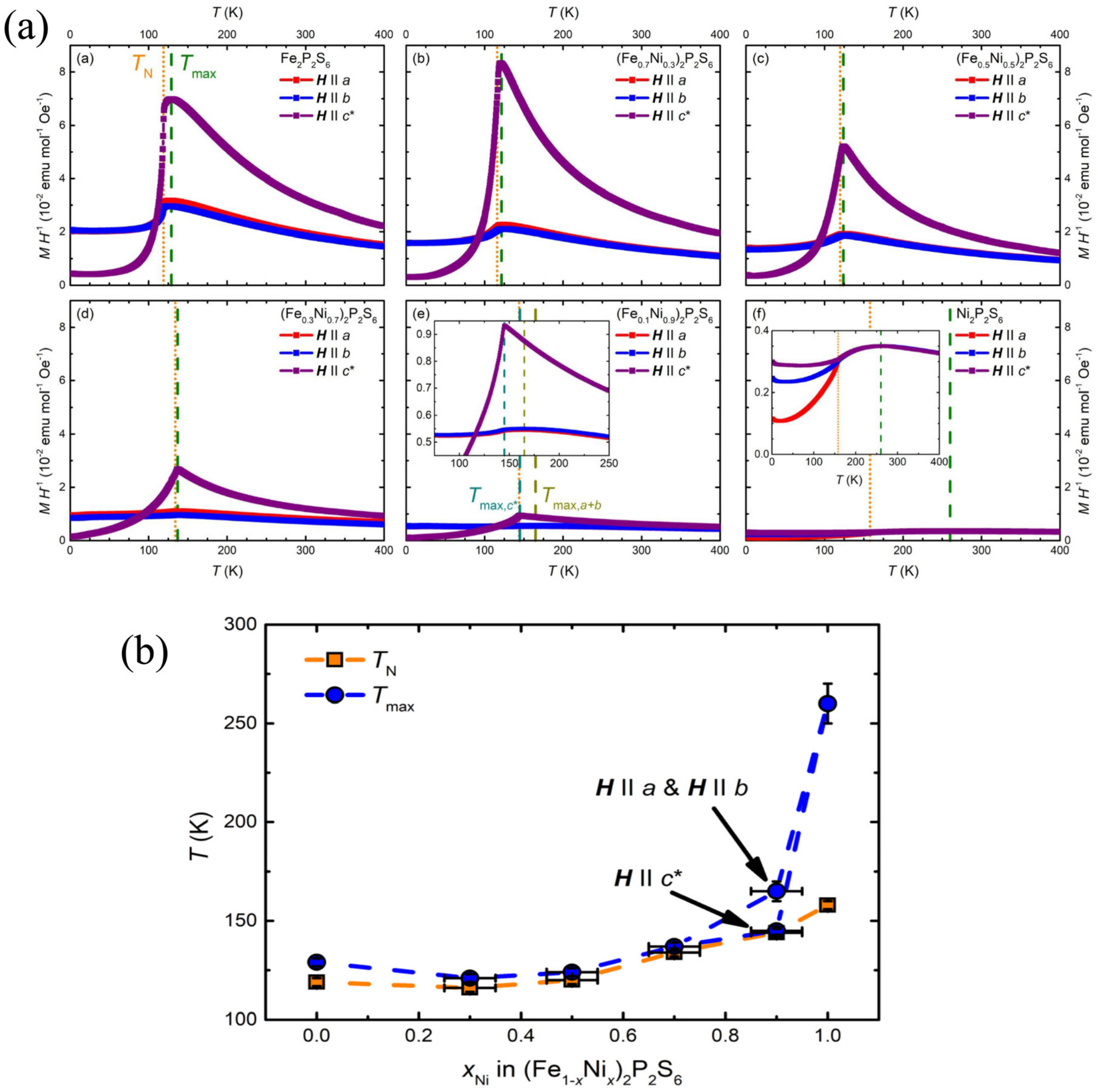

Fig. 6 (a) Temperature dependencies of magnetization divided by magnetic field MH^{-1} for $Fe_2P_2S_6$, $(Fe_{0.7}Ni_{0.3})_2P_2S_6$, $(Fe_{0.5}Ni_{0.5})_2P_2S_6$, $(Fe_{0.3}Ni_{0.7})_2P_2S_6$, $(Fe_{0.1}Ni_{0.9})_2P_2S_6$, and $Ni_2P_2S_6$, measured with a field of 1 T applied along three different crystallographic directions. T_N and T_{max} denote Néel temperature and the maximum magnetization temperature. (b) Evolution of T_N and T_{max} with composition for $(Fe_{1-x}Ni_x)_2P_2S_6$. Reprinted (adapted) with permission.[88] Copyright 2021, American Physical Society.

end compounds $FePS_3$ ($x = 0$) and $NiPS_3$ ($x = 1$), susceptibility first increases upon cooling, forming a broad maximum at around temperature T_{max}, followed with the AFM transition temperature T_N below T_{max}. On increasing Ni content x, T_N is found to slightly reduce up to $x = 0.3$, followed by systematic increase with further increasing Ni content [Fig. 6(b)]. Judging from magnetic exchange interaction, such T_N increase can be explained by stronger magnetic exchange interactions J_1 and J_3 for $NiPS_3$ [128] than $FePS_3$ [107] (Table 4). Composition dependence for T_{max} follows a similar non-monotonic trend, but T_{max} increases more remarkably with Ni content in Ni-rich compositions [Fig. 6(b)]. As mentioned in the previous section on $Mn_{1-x}Fe_xPS_3$, the broad maximum exists in pristine MPX_3 and has been ascribed to the strong low-dimensional dynamic magnetism pertaining to short-range correlated spins. Similarly, in $Fe_{1-x}Ni_xPS_3$ this broad maximum is also suppressed by substitution, leading to sharper susceptibility transition at T_N in substituted samples. This suggests the suppression of the short-range magnetic correlation by substitution in this system. However, the Raman spectroscopy results based on two-magnon Raman scattering reveal that the short-range dynamic magnetism does not quickly quench but rather persists to compositions much below $x = 0.9$.[91] Therefore, more efforts are needed to clarify the nature of such a broad maximum above T_N.

The rapid suppression of a broad maximum with Fe substitution in $NiPS_3$ also suggests the modification of XY-type magnetism. In fact, the evolution from XY- to Ising-type anisotropy below $x < 0.9$ is clearly manifested in susceptibility. For pristine $NiPS_3$ ($x = 1$), susceptibility measured with field along a (χ_a), b (χ_b), and c^* (χ_{c^*}) axes overlaps above T_N but display significant anisotropy below T_N [Fig. 6(a)], implying a moment orientation along the a-axis and consistent with the reported magnetic structure.[123] However, by adding Fe, the $x \le 0.9$ (*i.e.*, Fe content ≥ 10%) samples display anisotropy even above T_N, and χ_{c^*} exhibits much stronger temperature dependence. Those observations are characters for highly anisotropic Ising-type magnetism with out-of-plane moment orientation of the end compound $FePS_3$ ($x = 0$).[107] Therefore, a transition from XY- to Ising-type anisotropy may start with only 10% Fe substitution in $NiPS_3$. Such sensitive tuning of magnetic anisotropy in $NiPS_3$ by just 10% Fe substitution might be attributed to a much stronger (≈9 times) single-ion anisotropy (A) for $FePS_3$ [107] than $NiPS_3$ [128] (Table 4).

4.2.1.1.3. $Ni_{1-x}Mn_xPS_3$. $Ni_{1-x}Mn_xPS_3$ provides a platform to study spin-flop transitions under relatively low magnetic fields. In AFM systems, a magnetic field along the easy axis exceeding a critical spin-flop field H_{SF} drives the magnetic moments to rotate to a canted configuration with a component *perpendicular* to the field direction, resulting in a net moment along the easy axis.[163,164] Such field-driven moment reorientation from AFM to SF state is known as the spin-flop (SF) transition, which manifests into a super-linear behavior in field-dependent magnetization measurements (*i.e.*, magnetization upturn). This is different from the spin–flip transition in which the moments are polarized to the magnetic field direction under a strong field and is characterized by a magnetization saturation-like behavior. For $MnPS_3$ with magnetic moment along the out-of-plane direction (Fig. 3),[78,134] a SF transition in the isothermal magnetization has been observed under out-of-plane magnetic field ($H\perp ab$) but is absent under in-plane field ($H\|ab$) [Fig. 7(a)–(c)].[10,28,65,119,146] During this SF transition, the magnetic moments undergo continuous rotation towards the ab-plane.[134] Although the SF transition was discovered a long time ago[165] and widely studied from bulk to atomically thin $MnPS_3$,[29] it has been reported only recently in $NiPS_3$.[89] $NiPS_3$ displays an SF transition under the in-plane field of ∼6 T at 2 K [Fig. 7(c)], which is consistent with the almost in-plane moment orientation of this compound (Fig. 3),[33,111,166] as shown by a black arrow in Fig. 7(c). Also, the zig-zag AFM structure with moments oriented along a-axis leads to an anisotropic SF transition that is sensitive to the in-plane field orientations.[89]

The distinct SF behavior in $NiPS_3$ and $MnPS_3$ indicates an evolution of SF transition with composition in "mixed" compounds $Ni_{1-x}Mn_xPS_3$. Indeed, magnetism is found to be highly tunable with composition. Fig. 7(b) and (c) show that the in-plane and out-of-plane magnetizations exhibit a systematic enhancement upon increasing Mn content x, consistent with the greater magnetic moment of Mn^{2+} than Ni^{2+}. Interestingly, the SF transitions are also extremely sensitive to composition variation.[89] The SF transition in $NiPS_3$ under an in-plane field disappears up to 5% Mn substitution (*i.e.*, x = 0.05 in $Ni_{1-x}Mn_xPS_3$, Fig. 7(c)). Similarly, the H_{SF} for the out-of-plane field in $MnPS_3$ is reduced by half with 5% Ni substitution (*i.e.*, x = 0.95) and disappears upon 10% substitution (x = 0.9) [Fig. 7(b)]. Such highly sensitive nature of SF tran-

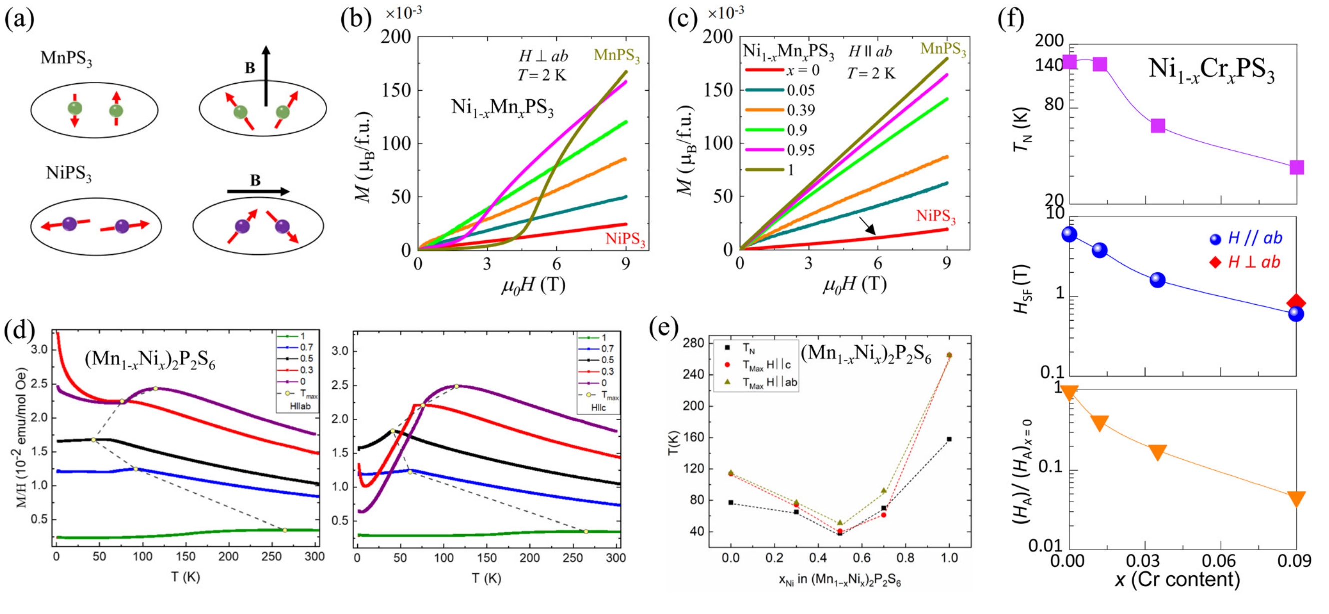

Fig. 7 (a) Schematics of spin-flop transition for $MnPS_3$ and $NiPS_3$.[89] (b and c) Magnetic field dependence of magnetization for $Ni_{1-x}Mn_xPS_3$ under in-plane ($H\|ab$) and out-of-plane ($H\perp ab$) magnetic fields.[89] Reprinted (adapted) with permission.[89] Copyright 2021, American Physical Society. (d) Temperature dependence of magnetization for $(Mn_{1-x}Ni_x)_2P_2S_6$ under in-plane ($H\|ab$) and out-of-plane ($H\|c$) magnetic fields.[87] (e) Evolution of T_N and T_{max} with composition for $(Mn_{1-x}Ni_x)_2P_2S_6$.[87] (f) Doping dependence of Néel temperature (T_N), spin-flop field (H_{SF}), and the effective magnetic anisotropy field (H_A) of $Ni_{1-x}Cr_xPS_3$.[177]

sition to light substitution of magnetic atoms is very different from that of non-magnetic substitution. It has been found that 20% substitution is needed to reduce H_{SF} by half in Zn-substituted $MnPS_3$.[78,85] In Ni-substituted $MnPS_3$, the substantially different single-ion anisotropy (Table 4) may explain the efficient suppression of SF transition. A similar mechanism has also been proposed for the suppression of H_{SF} in $MnPS_3$ under pressure.[135] In addition, Ni–Mn substitution can also be viewed as inducing magnetic impurities, especially in low-substitution levels. Hence, it is necessary to consider the magnetic interaction to understand the observed sensitive doping dependence in $Ni_{1-x}Mn_xPS_3$. The magnetic ordering temperature T_N characterizes the strengths of magnetic interactions. For lightly substituted samples with x close to 0 or 1, the T_N is found to only change slightly as compared to the parent compounds $NiPS_3$ and $MnPS_3$, which is interesting given that the light Ni–Mn substitution drastically suppresses the SF transitions. This suggests that the efficient suppression of the SF transition with light magnetic substitution in $Ni_{1-x}Mn_xPS_3$ can be attributed to the tuning of single ion isotropy rather than exchange interaction.

The modification of magnetic anisotropy with Ni–Mn substitution in $Mn_{1-x}Ni_xPS_3$ [87] is further demonstrated by the temperature dependence of susceptibility ($\chi = M/H$) [Fig. 7(d)]. For compositions $0 \le x \le 0.5$, the out-of-plane susceptibility (χ_c, measured under an out-of-plane field) is significantly reduced below T_N in comparison to in-plane susceptibility (χ_{ab}, measured under an in-plane field), implying moment orientation along the c axis, consistent with the reported magnetic structure of pristine $MnPS_3$.[78,134] This susceptibility trend is reversed on further increasing Ni content above $x > 0.5$ in which $\chi_{ab} < \chi_c$ below T_N,[87] suggesting switching of magnetic easy axis from out-of-plane to in-plane direction above $x > 0.5$. These results agree well with a theoretical study that predicts the magnetic transition from Néel-type (where all nearest-neighbor spins are aligned antiparallel as shown in Fig. 3) in pristine $MnPS_3$ to zigzag-type in pristine $NiPS_3$ (Fig. 3) at around $x = 0.25–0.5$.[152]

In addition, the T_N and T_{max} (broad maximum temperature) in susceptibility also provide useful information. As shown in Fig. 7(e), both T_N and T_{max} undergo non-monotonic dependence on Ni–Mn substitution with a minimum around $x = 0.5$ (ref. 87, 89 and 152) that can be ascribed to the attenuation of the magnetic interaction due to magnetic disorder in such a magnetically substituted system. T_{max} is much larger than T_N for both $MnPS_3$ and $NiPS_3$, but is comparable with increasing substitution levels [Fig. 7(e)], reminiscent to the observation for $Fe_{1-x}Ni_xPS_3$ [88,91] described above. Furthermore, for $x = 0.5$ composition, the PM to AFM transition at $T_N = 42$ K is followed by the emergence of a reentrant spin glass state at low temperature,[152] which is manifested by the irreversibility between ZFC and FC below $T = 30$ K similar to the case of $Mn_{1-x}Fe_xPS_3$ described above.[81]

4.2.1.1.4. $Ni_{1-x}Cr_xPS_3$. The Cr-based layered compounds, such as CrI_3, $Cr_2Ge_2Te_6$, $CrCl_3$, and $CrPS_4$, have recently gained intensive attention because of their robust magnetic order persisting in the 2D limit.[7,8,167–169] Surprisingly, the study of Cr-based MPX_3 compounds has been very limited. So far, only $CrPSe_3$ [170] and $Cr_{2/3}PS_3$ [171] have been reported while the stoichiometric $CrPS_3$ has not been experimentally realized. This has been attributed to the weakened P–P dimerization that favors the formation of Cr^{3+} cation instead of the +2 metal valence required to stabilize the MPX_3 lattice.[172] The direct substitution of Cr^{3+} for M^{2+} ion in MPX_3 is challenging from a chemical valence balance perspective, which may eventually lead to vacancies at metal sites. A similar issue also occurs for V_xPS_3 ($x = 0.78$ (ref. 173 and 174) and 0.9 (ref. 71)) in which V^{2+} and V^{3+} ions coexist and lead to V vacancies. Indeed, Cr substitution in MPX_3 has been found to be challenging in comparison to other divalent metal ion substitutions.[87–89,91,175,176]

So far, light substitution of up to 9% without inducing a clear signature of vacancies in $NiPS_3$ has been recently reported.[177] The lack of vacancies from composition analyses implies an isovalent substitution of +2 valence for Cr ions. Interestingly, a low Cr amount already can efficiently modulate the magnetism in $NiPS_3$. As shown in Fig. 7(f), first, the magnetic transition temperature T_N is found to reduce significantly from 155 K in $NiPS_3$ to 34 K in the $x = 0.09$ sample. Second, the SF transition under an in-plane magnetic field in $NiPS_3$ is significantly suppressed [Fig. 7(f)]. Also, the SF transition starts to occur even under a weak out-of-plane magnetic field of <1 T in the $x = 0.09$ sample, which strongly implies moment reorientation upon Cr substitution. Evaluating the characteristic field for spin flop, magnetic exchange, and magnetic anisotropy also reveals that the magnetic anisotropy is significantly suppressed by Cr substitution. Furthermore, in addition to SF transition, a moment polarization-like behavior has been observed under both in-plane and out-of-plane fields, with a similar polarization field of ~8 T and a small saturation moment of $0.24\mu_B$ per formula unit.

Suppressed SF transition and more isotropic magnetization are consistent with a suppression of magnetic anisotropy upon Cr substitution, which gives rise to more controllable moment orientations and eventually the moment polarization in the $x = 0.09$ sample. Indeed, similar field-induced moment polarization at relatively low magnetic fields have also been seen in quite a few Cr-based AFM compounds such as $CuCrP_2S_6$,[153,154] $CrPS_4$,[178] $CrCl_3$,[179] and CrSBr.[180] However, owing to the 3+ valence of Cr ions instead of the 2+ metal valence expected in MPX_3, substituting Cr is limited to only 9% in $NiPS_3$, as discussed above. This makes it difficult to explore the potential of this route.

Therefore, recently, an alternative approach that balances the valence by co-substituting mono-valent metal ions together with the tri-valent Cr ions has been reported, through which all M^{2+} ions can be replaced to tune the magnetism more efficiently.[181] This work provides a new doping strategy in the MPX_3 family, which successfully substitutes an equal Cu and Cr for Ni leading to a wide range of medium-entropy compositions $Cu_xNi_{2(1-x)}Cr_xP_2S_6$ ($0 \le x \le 1$).

4.2.1.1.5. $Mn_{1-x}Co_xPS_3$. Compared to other metal substitutions, Co substitution has been fairly elusive in MPX_3 with only a few recent studies.[114,116,117] This might be due to the challenges in crystal growth for $CoPS_3$[117] which causes this compound and its derivatives to be less-explored.[36,108,129,182] A recent breakthrough in reactive flux technique using P_2S_5 and metal precursors offers an opportunity to study Co-substituted MPX_3 compounds,[114–118] as described in section 2. The $Mn_xCo_{2-x}P_2S_6$ single crystals can be obtained by annealing the stoichiometric mixture of Mn, Co, and P_2S_5 powders at 540 °C for 72 hours.[117]

The two parent compounds $Mn_2P_2S_6$ (Néel-type AFM with out-of-plane easy axis) and $Co_2P_2S_6$ (zig-zag type AFM with in-plane easy axis) exhibit distinct AFM ordering, so magnetism is expected to be tunable with substituting. As shown in Fig. 8(a), the magnetic susceptibility of $Mn_xCo_{2-x}P_2S_6$ lacks significant irreversibility between ZFC and FC in the entire temperature range, suggesting AFM ordering below T_N without spin-glass state that is also seen in Fe-[81] and Ni-substituted[152] $Mn_2P_2S_6$. Similar to many other metal substituted MPX_3,[81,85,87,89,152] T_N also exhibits a non-monotonic composition dependence, showing maximum values for the two end compounds (x = 0 and 1) and reduces upon mixing the metal atoms. In addition, the broad maximum temperature T_{max} observed just above T_N also displays a similar variation with substitution, except that the broad maximum in susceptibility is completely suppressed for the x = 1 (50% Mn and 50% Co) sample, as shown in Fig. 8(a). Such suppression is also observed in thin flakes of $Mn_2P_2S_6$, which has been ascribed to the reorientation of Mn^{2+} moments that gives rise to a weak FM state.[183] Similar weak ferromagnetism may also be responsible to the rapid rise in the susceptibility at low temperature below $T < 30$ K [Fig. 8(a)] and non-linear isothermal magnetization at $T = 2$ K [Fig. 8(b)] for this x = 1 sample. Nevertheless, one should always be caution about the presence of trace FM impurities in doped materials.

The evolution of Curie–Weiss temperature θ_{cw} extracted from the linear fit of the high temperature ($T > 200$ K) paramagnetic (PM) region of the inverse susceptibility also provides useful information.[117] θ_{cw} is negative for AFM $Mn_xCo_{2-x}P_2S_6$, which undergoes a non-monotonic variation with Mn–Co substitution and reaches the maximal (*i.e.*, less negative) at x = 1, indicating the attenuation of AFM interaction around this composition. This is probably due to magnetic frustration owing to the competition between distinct AFM exchange interactions J_1, J_2, and J_3 for $Mn_2P_2S_6$ [35] and $Co_2P_2S_6$.[129]

4.2.1.1.6. $Ni_{1-x}Co_xPS_3$. Magnetic properties of Co-substituted $NiPS_3$ ($Ni_{1-x}Co_xPS_3$) have been investigated in both single crystals and nanosheet (NS) samples.[90] $Ni_{1-x}Co_xPS_3$ single crystals were grown using a CVT technique as shown in

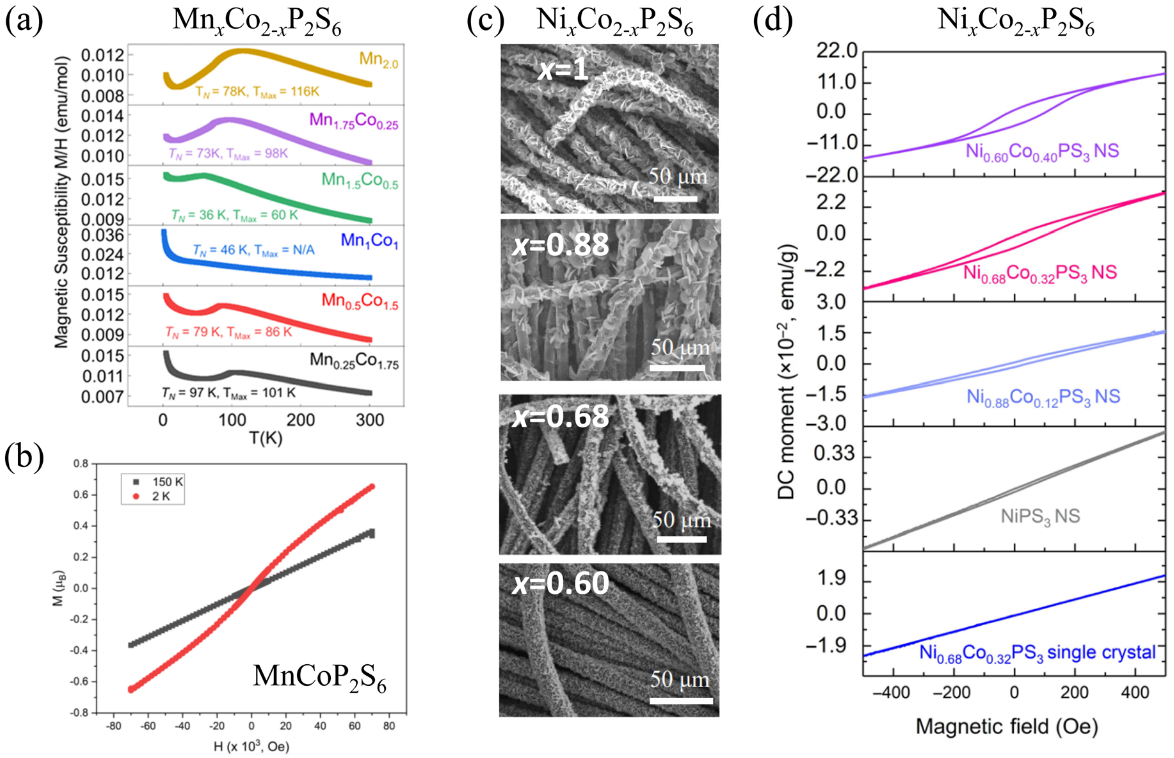

Fig. 8 (a) Field-cooled (FC) magnetic susceptibility of $Mn_xCo_{2-x}P_2S_6$ measured with H = 1000 Oe.[117] (b) Magnetization for $MnCoP_2S_6$ at 2 K and 150 K.[117] Reprinted (adapted) with permission.[117] Copyright 2022, American Chemical Society. (c) SEM images of nanosheet (NS) of $NiPS_3$, $Ni_{0.88}Co_{0.12}PS_3$, $Ni_{0.68}Co_{0.32}PS_3$, and $Ni_{0.60}Co_{0.40}PS_3$.[90] (d) Magnetization at 5 K for $Ni_{1-x}Co_xPS_3$ NS and single crystal samples.[90]

Table 1. For NS samples, $Ni_{1-x}Co_xPS_3$ ($0 \leq x < 0.5$) NS of average thickness of 8 nm (around 10 layers) were grown by a chemical vapor conversion method *via* a two-step process: first, the metal hydroxide NS precursor containing various Ni : Co ratios were synthesized on carbon cloth through a wet chemical method. Second, these metal hydroxide precursors were loaded downstream of an evacuated custom-designed fused silica socket tube with a mixture of P and S positioned on the other side. Ultrathin $Ni_{1-x}Co_xPS_3$ NS can be evenly grown on carbon cloth over a reaction time of 90 min at 480° to 490 °C with an argon gas flow [Fig. 8(c)].[90]

Magnetization measurements with the background from carbon cloth removed are shown in Fig. 8(d). $T_N \approx 155$ K for pristine $NiPS_3$ is suppressed by Co substitution for both single crystals and NS, which is in line with the general trend of metal substitution in MPX_3 as described above. In contrast to bulk single crystals, susceptibility for all $Ni_{1-x}Co_xPS_3$ ($0 \leq x \leq 0.4$) NS samples display low-temperature upturns, suggesting the rise of weak ferromagnetism. Field dependence of magnetization [Fig. 8(d)] also reveals magnetic hysteresis over a low field region ($|H| < 300$ Oe), which becomes more obvious with increasing Co content.

Providing similar lattice parameters and zig-zag type AFM structures for pristine $NiPS_3$ and $CoPS_3$, it is not surprising that Co–Ni substitution does not cause significant modification in magnetic properties. The low-temperature magnetization upturn and magnetic hysteresis occur in NS samples, which might be attributed to the sulfur vacancy in NSs. Electron spin resonance (ESR) spectroscopy measurements[90] have revealed that the sulfur vacancy formation, which is in line with the rise of ferromagnetism with Co substitution. Defect-induced ferromagnetism has been observed in the atomically thin layers of non-magnetic 2D materials such as graphene[2,184] and MoS_2.[4,185] As mentioned earlier in section 4.1, in $NiPS_3$, the magnetic interactions are mainly governed by the Ni–S–Ni superexchange interactions, occurring through the overlapping of half-filled Ni e_g and S 3p orbitals that mediates the effective electron hopping between neighboring Ni sites.[128] Therefore, tuning of magnetic states due to sulfur vacancy is plausible in $Ni_{1-x}Co_xPS_3$ NS. In fact, the theoretical calculations have demonstrated the disruption of anion-mediated superexchange interaction between Ni moments due to sulfur vacancy.[90] Furthermore, the calculated electronic structure has revealed unoccupied in-gap-like states that could serve as a carrier trap site and hinder the charge transfer process, further suppressing superexchange interaction and might facilitate other competing magnetic phases in $NiPS_3$.

4.2.1.1.7. Non-magnetic dopant: $Mn_xZn_{1-x}PS_3$. Magnetic properties of Zn-substituted $MnPS_3$ have been widely studied using magnetization[77,78,85] and Raman[151] measurements. Up on replacing Mn by non-magnetic Zn, the broad maximum immediately above T_N in susceptibility measured with in-plane field starts to vanish with increasing Zn substitution, leading to a sharp susceptibility peak at magnetic transition T_N.[85] This suggests a breakdown of short-range correlation, as expected for metal substitution in MPX_3.[81,87,88,91] In addition, for Zn-rich samples (Zn content ≥ 0.5), the low-temperature susceptibility displays an abrupt enhancement, which has been ascribed to a weak PM behavior of the significant number of isolated spins due to magnetic dilution by Zn.[85,151]

Suppression of transition temperature T_N by Zn substitution is seen in both susceptibility[85] and Raman[151] experiments. Unlike magnetic ion substitutions that always lead to a U-shape non-monotonic composition dependency of T_N, non-magnetic Zn substitution gradually suppresses T_N to zero temperature up to 50% substitution level in magnetization measurements[77,85] [Fig. 9(a)], or even to 70% from extrapolating the results from Raman spectroscopy[151] [Fig. 9(b)]. This is surprising given the critical concentration for site dilution in a honeycomb lattice with nearest-neighbor interactions (J_1) is $x = 0.7$.[186] Therefore, J_1 alone may not explain the behavior of $Mn_xZn_{1-x}PS_3$, and the second (J_2) and the third (J_3) nearest-neighbor interactions, though weaker than J_1 in $MnPS_3$ (see Table 4), might be ascribed for the magnetic stability below $x < 0.7$.[85] Of course, measurements on the addition of high-Zn samples would provide a better estimate of the critical composition, which was determined by linear extrapolation of a few compositions[151] as shown in Fig. 9(b).

The impact of Zn substitution in $MnPS_3$ is further manifested as reduced SF transition field H_{SF}.[78] Substituting Zn for Mn breaks down the long-range magnetic order, resulting in "weakly bound" Mn moments aligned along the out-of-plane direction. For $MnPS_3$ in which the dipolar anisotropy dominates, the local dipole field along the out-of-plane direction may be attenuated by these weakly bound moments. Furthermore, replacing a Mn with a non-magnetic Zn is accompanied by a vanishing moment at the substitute site, which affects the nearby Mn moments and causes them to be canted.[77] On a larger scale, this leads to an average staggered magnetic moment which consequently suppresses the magnetic anisotropy of the system, which eventually suppresses H_{SF}.[78]

4.2.1.1.8. Non-magnetic dopant: $Fe_{1-x}Zn_xPS_3$. Magnetic dilution by non-magnetic Zn substitution has also been studied in Ising-type antiferromagnet $FePS_3$.[93] Substituting Zn in $FePS_3$ is reported to induce weak ferromagnetism associated with spin/cluster spin glass.[93] As shown in Fig. 9(c), substituting Fe with non-magnetic Zn suppresses T_N. For Zn content x greater than 0.3, significant irreversibility between ZFC and FC measurements starts to occur at temperatures below T_N, which has been ascribed to weak ferromagnetism associated with glassy behavior.[93] For high Zn samples ($0.7 \leq x \leq 0.9$), susceptibility upturn appears at low temperatures, which has been attributed to the emergence of FM order with an out-of-plane easy axis.[93] This conclusion is also supported by the Curie–Weiss temperature (θ_{CW}), which becomes less negative with increasing Zn substitution and even attains positive values for $\chi_\perp$ of $x = 0.7$ and 0.9 samples, suggesting the attenuation of AFM interactions and development of FM correlation with Zn substitution in $FePS_3$.[93]

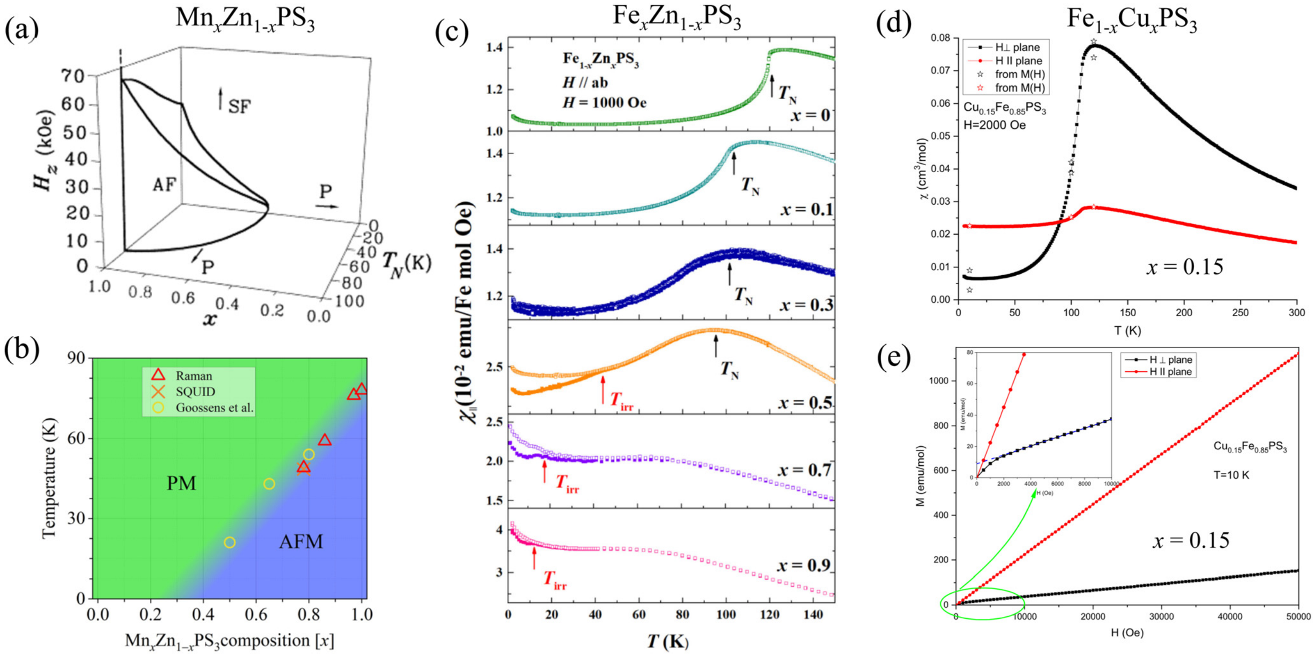

Fig. 9 (a and b) Magnetic phase diagrams for $Mn_xZn_{1-x}PS_3$. Field dependence of phases is also shown in (a).[85,151] Reprinted (adapted) with permission.[85] Copyright 1998, IOP Publishing. Reprinted (adapted) with permission.[151] Copyright 2023, American Physical Society. (c) Temperature dependence of magnetic susceptibilities of $Fe_{1-x}Zn_xPS_3$ under an in-plane magnetic field of 1000 Oe.[93] (d) Temperature dependence of the magnetic susceptibility for $Cu_{0.15}Fe_{0.85}PS_3$ measured under in-plane (H||plane) and out-of-plane (H⊥plane) field of 2000 Oe. (e) Field dependence of magnetization for $Cu_{0.15}Fe_{0.85}PS_3$ at T = 10 K.[187]

The rise of ferromagnetism is further supported by the field dependence of magnetization. The in-plane magnetization displays linear field dependence for all compositions and temperature ranges. However, under $H\perp ab$ magnetic field, the x = 0.9 sample displays magnetic hysteresis and saturation behavior with saturation moment reaching ~4μ_B/Fe, which is consistent with the S = 2 Fe^{2+}.[93] The theoretical study further reveals the key role played by hole doping to stabilize ferromagnetism in Zn-substituted $FePS_3$.[93] In highly Zn-substituted samples x = 0.7 and 0.9,[93] the XPS result reveals the presence of Fe^{3+} ion in addition to Fe^{2+} ion, leading to hole doping and the subsequent rising of FM interactions mediated by bound magnetic polarons induced impurity-band-exchange in such diluted environment induced by Zn substitution in $FePS_3$.

4.2.1.1.9. Non-magnetic dopant: $Fe_{1-x}Cu_xPS_3$. In addition to Zn, magnetic dilution in $FePS_3$ has also been realized by Cu substitution.[187] Cu substitution up to 15% is found to suppress T_N to ≈108 K from that of 120 K in pristine $FePS_3$ [Fig. 9(d)],[187] consistent with the result obtained for Zn-substituted $FePS_3$ [93] and can be attributed to the suppression of magnetic exchange interactions, as discussed in the previous section. Other than that, the susceptibility for the substituted sample is highly similar to that of the pristine $FePS_3$: the out-of-plane susceptibility measured with a magnetic field perpendicular to the basal plane displays a much stronger temperature dependence below T_N than in-plane susceptibility. In addition, in the PM state, susceptibility displays strong anisotropy, with a much higher value for the out-of-plane susceptibility that is similar to undoped $FePS_3$ [Fig. 9(d)]. These observations suggest that magnetic anisotropy is not strongly modified upon Cu substitution up to 15%.

In field-dependent magnetization, the 10% Cu-substituted sample displays a weak non-linearity under an out-of-plane magnetic field [Fig. 9(e)], which was claimed to be a signature of weak ferromagnetism due to the reorientation of canted moments, and has also been observed in Zn-[78] and Ni-substituted[89] $MnPS_3$. In addition to a moment canting scenario, other mechanisms, such as sulfur vacancy which has been seen in Co-substituted $NiPS_3$ nanoflakes[90] (see section 4.2.1.1.5) and the presence of the finite clusters of uncompensated spins[187] might also give rise to weak ferromagnetism in $Cu_{0.15}Fe_{0.85}PS_3$.

4.2.1.1.10. Non-magnetic dopant: $Fe_{1-x}Cd_xPS_3$. Cd as another non-magnetic dopant has been studied a long time ago on a 50% Cd-substituted $Fe_{0.5}Cd_{0.5}PS_3$ sample.[188] Magnetic phase transition is not observed in susceptibility measurements down to 57 K. The Curie–Weiss temperature displays positive values, decreasing from 104 K for pristine $FePS_3$ to 40 K for $Fe_{0.5}Cd_{0.5}PS_3$. The positive Curie–Weiss temperature even in pristine $FePS_3$ appears interesting given it well defined AFM ground state. It might be ascribed to the competition between the direct FM J_1 and indirect AFM J_2 interactions.[188] The suppression of Curie–Weiss temperature upon introduction of Cd in $FePS_3$ can be attributed to the attenuation of direct J_1 owing to the expanded lattice due to Cd substitution, which increases the nearest neighbor distance of Fe^{2+} by 1.95%.[188] A more concrete understanding may be obtained by future substitution studies covering more Cd compositions.

4.2.1.1.11. Metal substitution in selenides: $Fe_{1-x}Mn_xPSe_3$. Most of the metal substitutions were performed on sulfides as summarized above, whereas the selenide $MPSe_3$ compounds are relatively less explored. Mn–Fe substitution has been reported in selenide compounds $MnPSe_3$ and $FePSe_3$,[86] which are characterized by Néel-type and Ising-type magnetic structures with in-plane and out-of-plane moments, respectively (Fig. 3). Similar to sulfide $FePS_3$ stated above, anisotropy between out-of-plane susceptibility $\chi_\perp$ and in-plane susceptibility $\chi_\parallel$ above T_N is a character of Ising-type magnetism in $FePSe_3$. Such anisotropy is suppressed by Mn substitution for Fe [Fig. 10(a)],[122] which is expected since the end compounds $FePSe_3$ and $MnPSe_3$ possess different magnetic structures with different easy axes. Interestingly, the susceptibility anisotropy below T_N suggests that the out-of-plane magnetic easy axis for $FePSe_3$ is robust against Mn-substitution up to 90%, which is also supported by the emergence and evolution of the SF transition. SF transition is not observed up to 9 T in $FePSe_3$ due to the strong magnetic anisotropy for Ising-type magnetism. Heavy Mn substitution leads the SF to occur in out-of-plane magnetization only, and further increased Mn content beyond 90% causes the SF transition to appear in in-plane magnetization, implying the switching of easy axis from out-of-plane to in-plane when Mn content $x > 0.9$ [Fig. 10(b)]. The rotation of the magnetic easy axis occurring only above 90% Mn for Fe substitution suggests a highly anisotropic magnetic order in $FePSe_3$. This can be estimated from the relative magnitudes of single-ion anisotropy (A) for the two end compounds $FePSe_3$ and $MnPSe_3$. Though the experimental value of A is still lacking for $FePSe_3$, in sulfide counterparts $FePS_3$ [107] possesses much higher A by >300 times than that of $MnPS_3$ [35] (Table 4). Expecting a similar scenario in selenide samples, the robust magnetic easy axis against up to 90% Mn substitution in $FePSe_3$ can be understood.

Because both end compounds $FePSe_3$ [42] and $MnPSe_3$ [43] exhibit 2D magnetism down to the monolayer limit, exploring possible 2D magnetism in their mixed compounds ($Fe_{1-x}Mn_xPSe_3$) is interesting. Having said that, the strong frustration arising from mixing two different magnetic metal ions

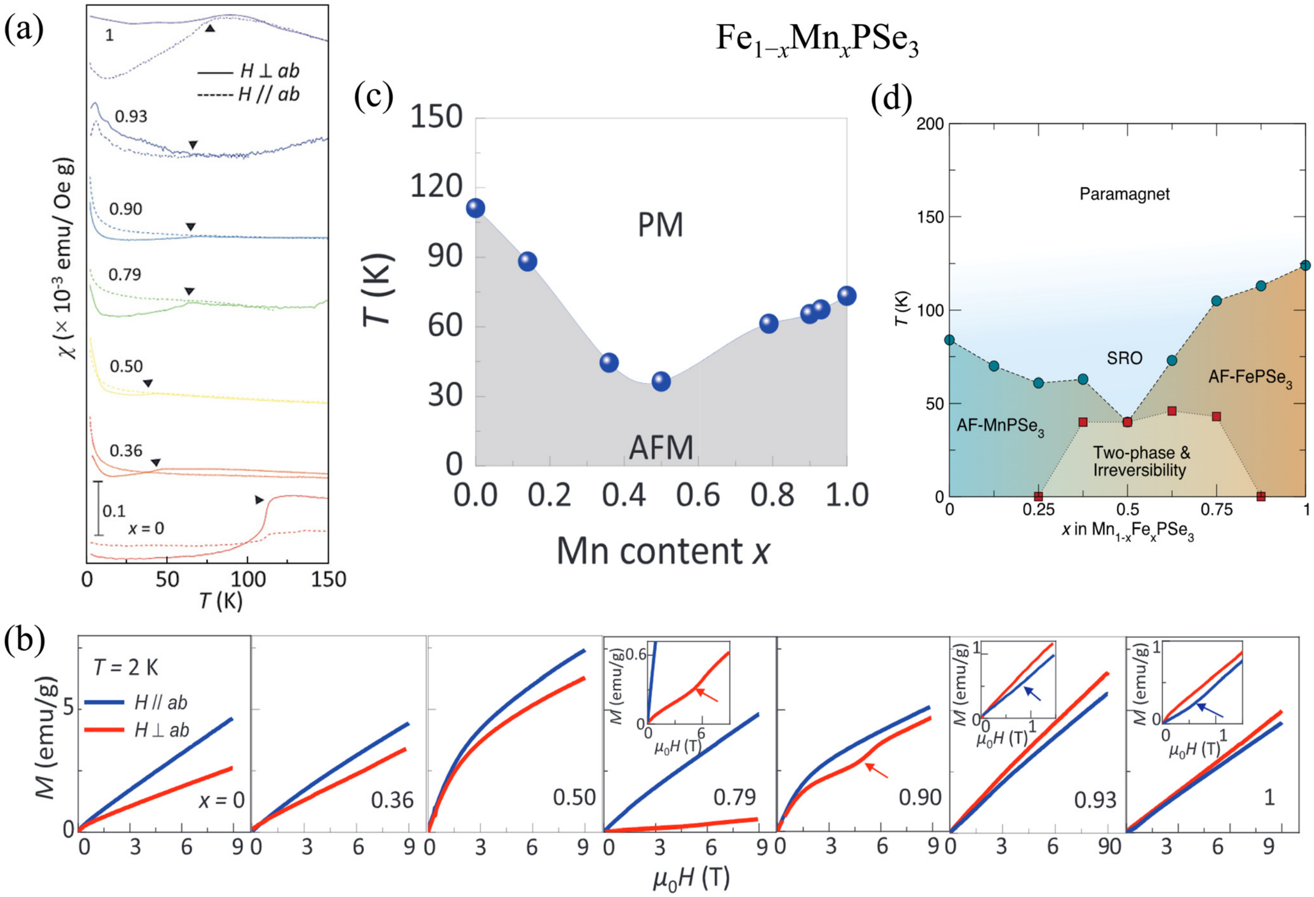

Fig. 10 (a) Temperature dependencies susceptibility for $Fe_{1-x}Mn_xPSe_3$ measured under a magnetic field of 0.1 T.[122] (b) Isothermal magnetization at 2 K for $Fe_{1-x}Mn_xPSe_3$ under out-of-plane ($H \perp ab$, red) and in-plane ($H \| ab$, blue) magnetic fields. Insets show spin-flop transition at low fields.[122] (c and d) Magnetic phase diagrams of $Mn_{1-x}Fe_xPSe_3$ obtained from (c) single crystals[122] and (d) polycrystals.[86] Reprinted (adapted) with permission.[86] Copyright 2020, American Physical Society.

may destabilize magnetic order in the 2D limit. Indeed, such mixing suppresses T_N and leads it to reach a minimum for 50% substitution in studies using both single crystals[122] [Fig. 10(c)] and polycrystals[86] [Fig. 10(d)]. This appears to be a generic behavior for all polymetallic MPX_3.[81,85,87,89] In addition, a mixed phase consisting of both Fe^{2+}- and Mn^{2+}-type ordering, forming nano-sized chemically disordered clusters in intermediate compositions ($0.25 < x < 0.875$) has also been discovered[86] [Fig. 10(d)].

4.2.1.1.12. $HEPX_3$ (HE = high entropy; X = S or Se). High entropy (HE) alloy involves the mixing of five or more elements each with a composition of 5–35 atomic percentage. The composition of HE compounds can be greatly varied by adjusting the ratios of constituent elements. Such flexible composition stoichiometry allows for property tuning with a wide compositions range. Incorporating multiple elements also offers various valence states and spin states in a system. Depending on the choices of elements, the distribution of charges and spin interactions may vary significantly. Furthermore, the presence of multiple elements results in a complex and disordered atomic structure. Hence, with the added complexity, HE compounds provides an opportunity to investigate the interplay between charge, spin, and composition degrees of freedom. Recently, the bimetallic substitution in MPX_3 has been extended to the realm of HE compounds.[113,121,189] Providing various anisotropy of ions and diverse magnetic structures for different MPX_3 compounds, such a strategy is expected to lead to rich magnetic properties and phases.

For $Mn_{0.25}Fe_{0.25}Co_{0.25}Ni_{0.27}P_{1.04}S_3$ [113,189] with equal molar ratio of metal atoms, a well-defined PM to AFM transition at T_N = 70 K is found in susceptibility measurements[113] [Fig. 11(a)]. Deviation from this equal metal concentration results in broader or less-obvious AFM transition, as observed in $Mn_{0.2}Fe_{0.3}Co_{0.25}Ni_{0.25}PS_3$.[189] In $Mn_{0.25}Fe_{0.25}Co_{0.25}Ni_{0.27}P_{1.04}S_3$, the magnetic moments are likely to be aligned perpendicular to the basal plan, providing a weaker temperature dependence for susceptibility under an in-plane field. A spin-glass state is also proposed due to the emergence of irreversibility between ZFC and FC susceptibility at a temperature below T_N [Fig. 11(b)]. Similarly, the spin-glass phase has also been observed in a few other $HEPS_3$ compounds at different glass temperatures,[113,189] as summarized in Table 5. In addition to sulfides, selenide-based HE compounds have also been studied in Fe–Mn–Cd–In-based HE $MPSe_3$.[121] The comparison study on $FePSe_3$, $Fe_{0.8}Mn_{0.1}Cd_{0.05}In_{0.05}PSe_3$, $Fe_{0.7}(MnCd)_{0.1}In_{0.1}PSe_3$, and $(FeMnCd)_{0.25}In_{0.17}PSe_3$ has revealed decreased T_N with reducing Fe amount [Fig. 11(c)]. The AFM transition disappears in $(FeMnCd)_{0.25}In_{0.17}PSe_3$, leaving a substantial susceptibility irreversibility around 15 K [Fig. 11(c)] that implies a glass state, which is further confirmed by the frequency-dependent peak in AC susceptibility measurements.[121]

4.2.1.2. *Non-isovalent substitution*

4.2.1.2.1. $CuCrP_2X_6$ (X = S or Se). The metal substitution in $M_2P_2X_6$ has been extended to the mixing of monovalent $M_1{}^{1+}$ (M_1 = Cu or Ag) and trivalent $M_2{}^{3+}$ (M_2 = V or Cr) ions to from $(M_1{}^{1+})(M_2{}^{3+})P_2X_6$.[153–157,190–192] Chemical valence is balanced by maintaining an equal amount of monovalent and trivalent ions. While these compounds have been discovered a long time ago,[155,157,190,193] there have been only a few studies on magnetic properties.[154,155,157,190,193,194] $CuCrP_2S_6$ [153,154] has recently gained increased attention. In contrast to the random distribution of dissimilar metal ions in isovalent metal-substituted $M_2P_2X_6$,[76–91] weak repulsive Coulomb interactions and substantial size difference between Cu^{1+} and Cr^{3+} cations[156] favor an alternating arrangements of them in $CuCrP_2S_6$:[153,154] as shown in Fig. 12(a), Cr^{3+} ions are located almost at the center in the vdW layer, whereas Cu+ ions are slightly displaced from the center at the alternative positions above and below the Cr^{3+} layers.[154] This further leads to broken inversion symmetry and ferroelectricity up to room temperature.[58,59,195]

Regarding the magnetic properties which is the focus of this review, $CuCrP_2S_6$ displays an AFM order below T_N = 32 K (ref. 154) [Fig. 12(b)]. On the other hand, $CuCrP_2Se_6$ has a slightly higher T_N (= 40 K) than that of $CuCrP_2S_6$, which is

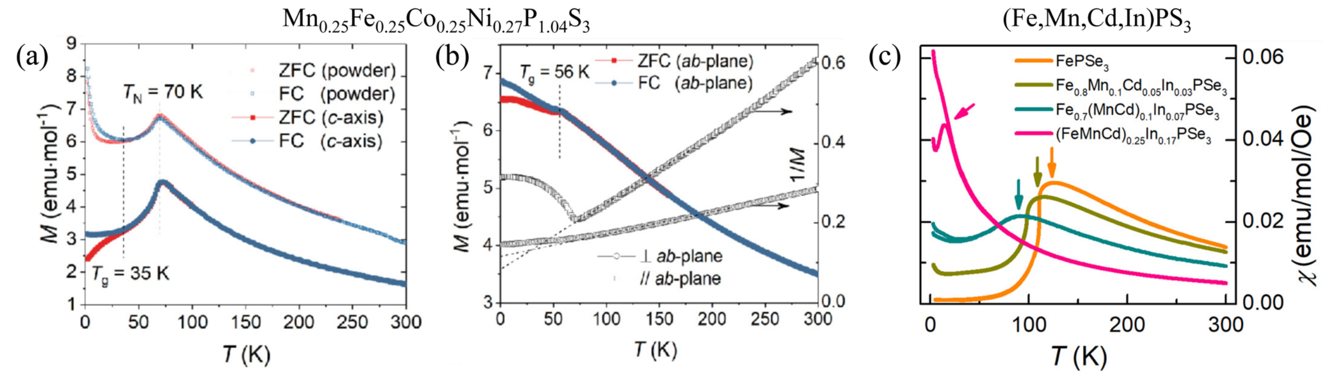

Fig. 11 (a and b) Magnetization of (Mn,Fe,Co,Ni)PS_3 under the external magnetic field of 500 Oe along different directions. The antiferromagnetic transition (T_N) and spin glass transition temperature (T_g) are indicated.[113] Reprinted (adapted) with permission.[113] Copyright 2021, American Chemical Society. (c) Susceptibility (χ) of pristine $FePSe_3$ and (Fe,Mn,Cd,In)PS_3.[121] Reprinted (adapted) with permission.[121] Copyright 2022, American Physical Society.

Table 5 Summary of magnetic properties of high-entropy MPX_3 compounds

$HEPX_3$ compounds	Magnetic properties	Ref.
$Mn_{0.25}Fe_{0.25}Co_{0.25}Ni_{0.27}P_{1.04}S_3$	AFM (T_N = 70 K) and spin-glass (T_{g1} = 35 K, T_{g2} = 56 K)	113
$Zn_{0.29}Mn_{0.14}Fe_{0.17}Co_{0.18}Ni_{0.24}PS_{2.61}$	Spin-glass (T_g = 30 K), T_{kink} = 120 K	113
$Mg_{0.19}Mn_{0.18}Fe_{0.19}Co_{0.26}Ni_{0.28}P_{1.08}S_3$	Multikinks in MT at 8 K, 42 K, 60, and 120 K	113
$V_{0.16}Mn_{0.18}Fe_{0.21}Co_{0.23}Ni_{0.24}PS_{2.62}$	Spin-glass (T_g = 37 K), T_{kink} = 150 K	113
$(FeMnCd)_{0.25}In_{0.17}PSe_3$	Spin-glass (T_g = 15 K)	121

likely attributed to a stronger Cr–Se–Se–Cr superexchange interaction due to enhanced covalency arising from greater atomic orbitals for Se.[196] The much sharper drop in susceptibility measured with the field along the *a*-axis in comparison to other field directions suggests the magnetic moment orientation along the *a*-axis. The linear fit of inverse susceptibility yielded a positive Curie–Weiss temperature θ_{cw} = 24 K [Fig. 12(b)], implying in-plane FM interaction that may be attributed to an A-type AFM order[154] (see Fig. 3). The effective moments of $\mu_{eff} = (3.78 \pm 0.05)\mu_B$ f.u.$^{-1}$ for $H \| ab$ and $\mu_{eff} = (3.89 \pm 0.05)\mu_B$ f.u.$^{-1}$ for $H \perp ab$[153] match with the theoretical value of $3.87\mu_B$ for Cr^{3+}. Like many other Cr-based van der Waals magnets such as $CrPS_4$,[178] $CrCl_3$,[179] and CrSBr,[180] as well as Cr-substitute $NiPS_3$ mentioned above (section 4.2.1.1.6), a field-driven AFM to FM transition has been observed in magnetization measurements with a saturation moment of $\approx 3\mu_B$/Cr [Fig. 12(c)]. Consistent with the easy-axis along the *a*-axis, an SF transition appears in magnetization with low $H_{SF} \approx 0.4$ T [Fig. 12(d)].

As mentioned above in section 4.2.1.1.4, the mono- and trivalent of Cu^+ and Cr^{3+} allows for co-substitute other bi-valent ions such as Ni^{2+} to form $Cu_xNi_{2(1-x)}Cr_xP_2S_6$ ($0 \le x \le 1$).[181] This doping strategy provides further tuning of magnetism in the MPX_3 family and leads to a wide range of medium-entropy compositions.

4.2.1.2.2. $AgMP_2X_6$ (M = V or Cr; X = S or Se). $AgVP_2S_6$ and $AgCrP_2S_6$ have been studied a long time ago.[191,192] Structurally, these materials form a zig-zag chain of V^{3+} (S = 1) and Cr^{3+} (S = 3/2) ions respectively along the *a*-axis [Fig. 13(a)], which is distinct from other MPX_3 compounds. Long-range AFM order is absent in $AgVP_2S_6$ from 5 to 200 K in susceptibility measurements[191] [Fig. 13(b)]. In contrast, $AgCrP_2S_6$ is reported to be AFM below $T_N \approx 7$ K (ref. 192) [Fig. 13(c)]. Such T_N from susceptibility is lower than $T_N \approx 20$ K obtained from powder neutron diffraction experiment.[155] Both compositions display enhanced susceptibility at low temperatures, but $AgVP_2S_6$ [191] is characterized by isotropic susceptibility for magnetic field directions along and perpendicular to the zig-zag chain direction [Fig. 13(a)], while $AgCrP_2S_6$ features a small anisotropy at low temperatures[192] [Fig. 13(b)].

A more recent study has expanded to selenide counterpart $AgVP_2Se_6$ [197] and $AgCrP_2Se_6$.[198] These compounds are structu-

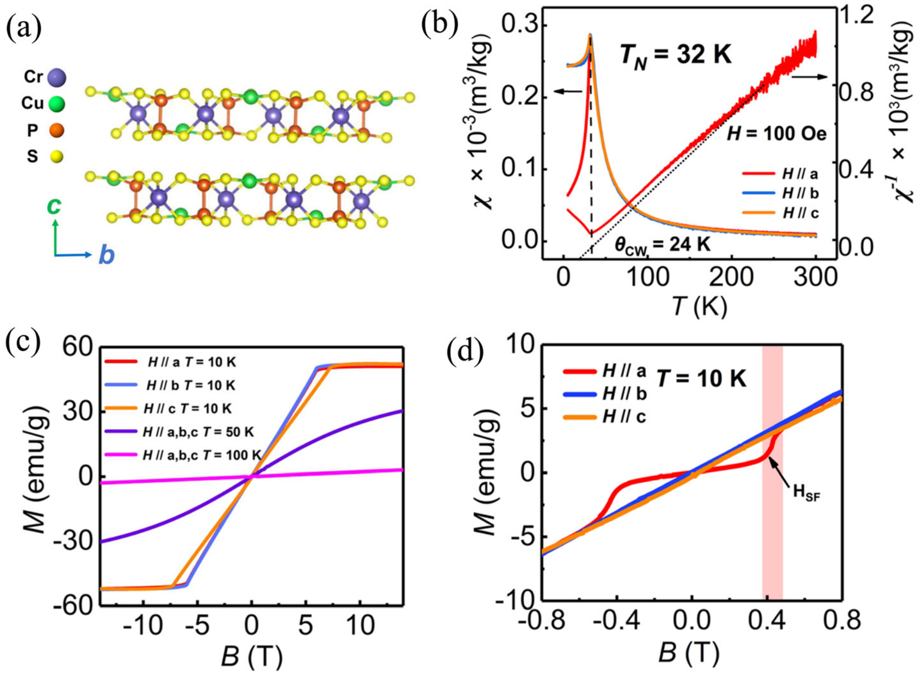

Fig. 12 (a) Crystal structure of $CuCrP_2S_6$. (b and c) Temperature and magnetic field dependencies of magnetic susceptibility of $CuCrP_2S_6$. (d) Spin-flop transition when the field is applied along the *a*-axis.[154]

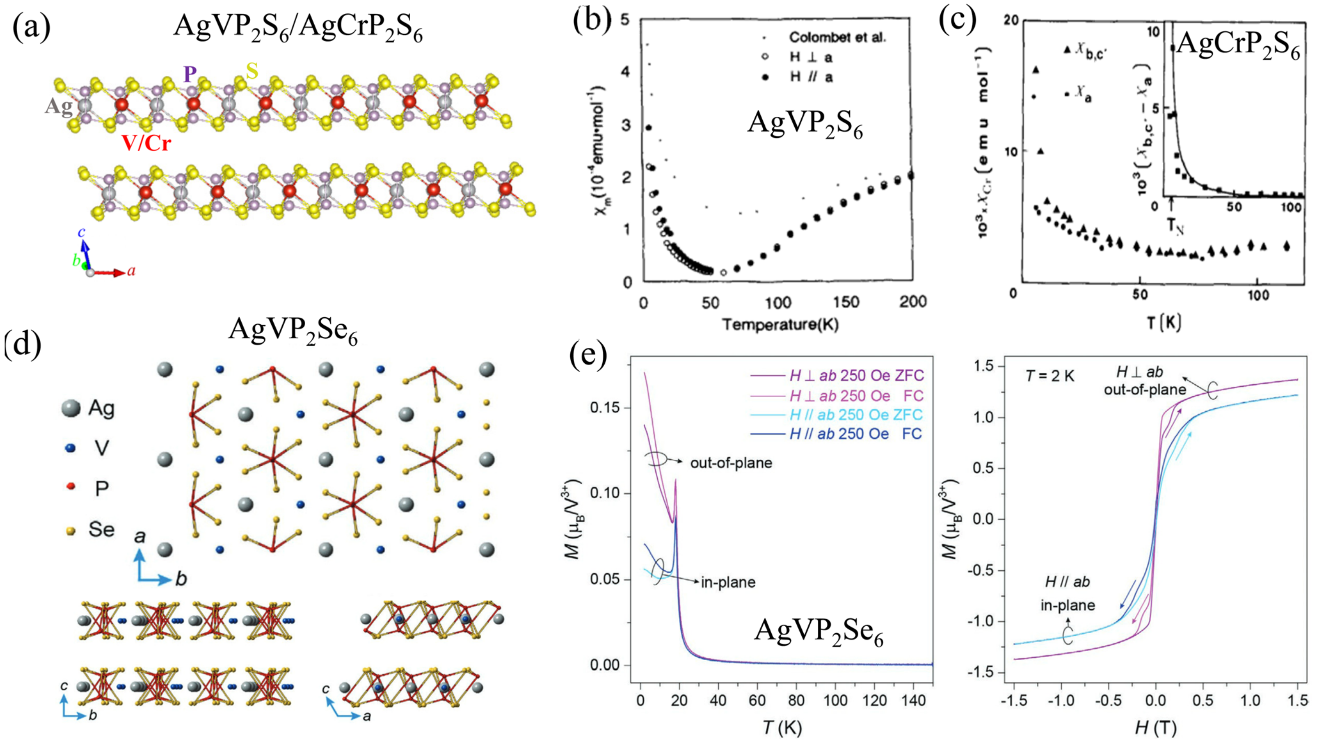

Fig. 13 (a) Crystal structure of $AgVP_2S_6$ and $AgCrP_2S_6$. (b and c) Temperature dependence of the susceptibility for $AgVP_2S_6$[191] and $AgCrP_2S_6$.[192] Reprinted (adapted) with permission.[191] Copyright 1994, Elsevier. Reprinted (adapted) with permission.[192] Copyright 1990, Elsevier. (d) Crystal structure (top and side views) of $AgVP_2Se_6$. (e) Temperature (left) and magnetic field (right) dependencies of magnetization for $AgVP_2Se_6$.[197]

rally slightly different from the above $AgVP_2S_6$ and $AgCrP_2S_6$ [Fig. 13(d)]. Interestingly, susceptibility irreversibility and magnetization saturation of $AgVP_2S_6$[197] [Fig. 13(e)] implies ferromagnetism with a $T_c \sim 18.5$ K, which is distinct from the AFM ground state for other MPX_3. On the other hand, $AgCrP_2Se_6$[198] exhibits AFM ground state below $T_N \sim 42$ K, which features field-driven moment polarization under the high field of $B \sim 3–6$ T. Furthermore, polar-reflective magnetic circular dichroism (RMCD) experiments on $AgVP_2Se_6$[197] found a growing hysteresis loop with reducing thickness in thin flakes, which persist down to 6.7 nm flake thickness with unchanged T_c.

4.2.2. Chalcogen (X) substitution.

As discussed in section 3, transition metal atoms M are surrounded by P_2X_6 clusters in each layer of MPX_3 (Fig. 2). So, substituting chalcogen X modifies the local environment of M^{2+} ion within honeycomb layers with the magnetic plane intact [Fig. 4(b)]. Therefore, chalcogen substitution offers a relatively clean approach to modifying magnetic exchange interactions. This approach has been demonstrated to be effective in other vdW magnets such as chromium halides,[145,146] in which the magnetism can be efficiently controlled by non-magnetic ligand substitution. Although the syntheses and structural characterizations of chalcogen-substituted MPX_3 have been reported a long time ago,[199–201] their magnetic properties were studied recently in a few Mn-, Fe-, and Ni-based MPX_3 compounds,[31,32] as described below.

4.2.2.1. $MnPS_{3-x}Se_x$. In $MnPS_{3-x}Se_x$, the successful substitution can be readily seen by the colors of the crystal. Upon increasing the Se content, these relatively transparent crystals gradually change color from green to wine red [Fig. 14(a)], indicating the variation of the optical gap.[31] Upon Se substitution, T_N displays a monotonic, slight reduction from 78.5 K for $MnPS_3$ to 74 K for $MnPSe_3$[31,32] [Fig. 14(b)], which is drastically different from non-monotonic composition dependence seen in metal-substituted $MnPS_3$.[81,85,87,89] This is found to be caused by the suppressed exchange interaction.[31] Magnetism in $MnPS_3$ is governed by the nearest-neighbor exchange interaction (J_1) from the Mn–Mn direct exchange,[39,128,129] and the third nearest-neighbor interaction (J_3) is also considerable (Table 5). Se substitution for S expands in-plane lattice[202,203] and elongates Mn–Mn distance, which attenuates the direct exchange and consequently reduces T_N.[31,32]

In addition to magnetic exchange interactions, chalcogen S–Se substitution also modifies magnetic anisotropy.[31] This is expected because the two end compounds $MnPS_3$ and $MnPSe_3$, though both possess Néel-type AFM structure within each vdW layer where all nearest-neighbor spins are aligned antiparallel, feature different magnetic out-of-plane[78,134] and almost-in-plane[30,86,94,95] easy axis, respectively[30,78,86,94,95,134] (Fig. 3). The modification of magnetic anisotropy is reflected by the evolution of SF transition. SF transition in $MnPS_3$ occurs under an in-plane field. The SF field H_{SF} is gradually suppressed to zero upon increasing Se content near $x = 1$

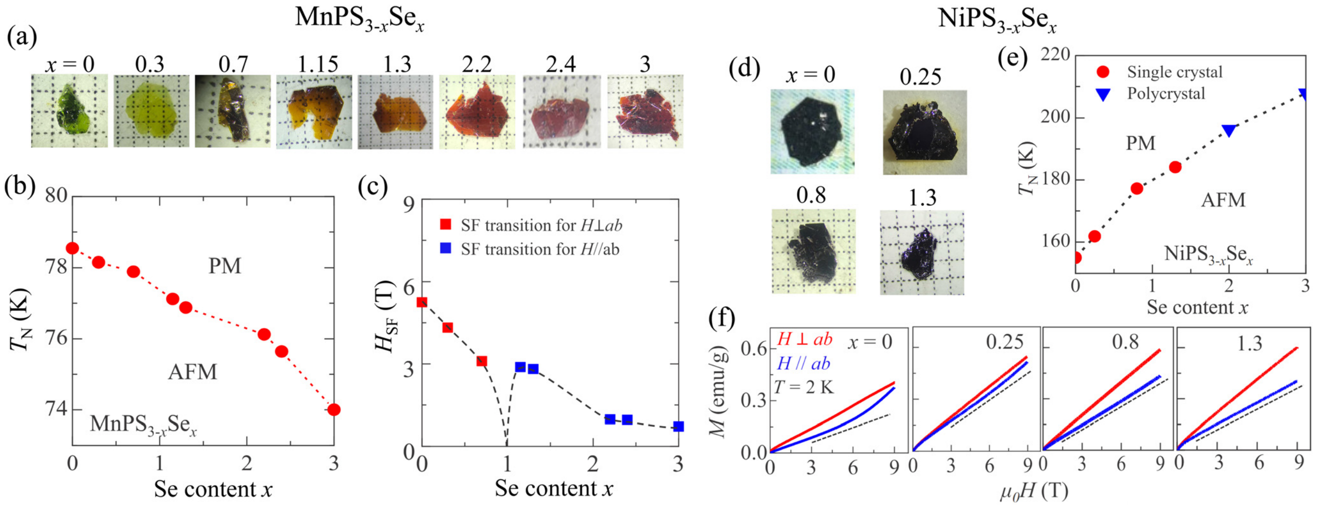

Fig. 14 (a) Images of $MnPS_{3-x}Se_x$ single crystals. Doping dependence of (b) Néel temperature (T_N) and (c) spin-flop (SF) field for $MnPS_{3-x}Se_x$. (d) Images of $NiPS_{3-x}Se_x$ single crystals ($0 \le x \le 1.3$). (e) Doping dependence of T_N for $NiPS_{3-x}Se_x$. (f) Field dependence of magnetization of $NiPS_{3-x}Se_x$ at $T = 2$ K.[31] Reprinted (adapted) with permission.[31] Copyright 2022, American Physical Society.

($MnPSSe_2$). On the other hand, the SF transition re-appears but under an out-of-plane field for $x > 1$ samples. Since SF transition in AFM material is driven by magnetic field component along the magnetic moment direction (*i.e.*, easy axis), this implies the rotation of easy axis from out-of-plane towards the in-plane direction with Se substitution, which can be attributed to the enhanced single-ion anisotropy upon Se substitution that usually favors the in-plane moment orientation in MPX_3. The switching of the easy axis is found to happen closer to the $MnPS_3$ side *i.e.*, between $x = 0.7$ and 1.2 [Fig. 14(c)], implying the magnetism in $MnPS_3$ is softer than $MnPSe_3$, which is also consistent with the results obtained from the theoretical calculations that reveal much smaller anisotropy between the in-plane and out-of-plane directions of the spins in $MnPS_3$ than $MnPSe_3$.[31]

4.2.2.2. $NiPS_{3-x}Se_x$. The study on Ni-based $NiPS_{3-x}Se_x$ faces difficulty in synthesizing single crystals for Se-rich compositions. Indeed, the studies on $NiPSe_3$ are very limited[39] as compared to the sulfide counterpart $NiPS_3$. A recent investigation on $NiPS_{3-x}Se_x$[31] combining single crystal with Se content up to $x = 1.3$ [Fig. 14(d)] and polycrystals up to $x = 3$ have revealed monotonic enhancement in T_N with increasing Se content, from ∼155 K for $NiPS_3$ to ∼210 K for $NiPSe_3$ [Fig. 14(e)]. This observation is distinct from the reduced T_N due to metal substitution in $NiPS_3$.[87,89] Interestingly, compared to $MnPS_{3-x}Se_x$ in which Se substitution slightly reduces T_N,[31,32] in $NiPS_3$ the similar Se substitution causes strong T_N enhancement.[31] Such results have been ascribed to different governing exchanges in Mn- and Ni-based systems.[31] Magnetism of both systems are determined by the nearest J_1 and third nearest J_3 while the second nearest-neighbor interaction J_2 is negligible (Table 4). Unlike $MnPS_3$ in which the direct exchange between the neighboring metal ions contributes to J as described in the previous section, neutron scattering experiments[39,128] have demonstrated that the magnetic interactions in $NiPS_3$ are superexchange in nature. The direct exchange between Ni^{2+}, however, does not exist due to the filled t_{2g} orbitals for Ni^{2+}.[39,128] Therefore, compared to S, Se with extended 4p-orbitals favors orbital overlap and enhances superexchange between Ni^{2+} through chalcogen, giving rise to enhanced T_N.

Similar to the case of $MnPS_3$, Se substitution also tunes SF transitions in $NiPS_3$.[31] The SF transition under an in-plane field of ∼6 T for $NiPS_3$ ($x = 0$) occurs at a higher in-plane field of ∼8 T for $x = 0.25$ [Fig. 14(f)]. Further increasing Se content up to 1.3 results in essentially linear magnetization under both in-plane ($H \| ab$) and out-of-plane ($H \perp ab$) fields up to 9 T. This is consistent with enhanced exchange interactions with Se substitution, based on evaluating the SF field, $H_{SF} \approx \sqrt{2H_EH_A}$ where H_E and H_A are effective exchange and magnetic anisotropy fields, respectively.[204] SF transition also provides a measure of magnetic anisotropy. When SF transition switches from one magnetic field direction to another, it suggests rotation of magnetic easy axis as seen in aforementioned $MnPS_{3-x}Se_x$. For $NiPS_{3-x}Se_x$, however, unavailable single crystals for Se-rich compositions, and the lack of experimentally determined magnetic structure for end compound $NiPSe_3$, make it difficult to judge the evolution of magnetic anisotropy based on magnetization study.

4.2.2.3. $FeP(S_{1-x}Se_x)_3$. In the MPX_3 family, $FePS_3$ has been identified as a representative material that displays Ising-type magnetism characterized by out-of-plane magnetic moments (Fig. 3).[6,40,107] Such Ising-type magnetism in $FePS_3$ has been proposed to originate from the combination of the strong spin–orbit coupling (SOC) of the high-spin Fe^{2+} (d^6) state and the trigonal distortion of FeS_6 octahedra.[40] Another Fe-based MPX_3 compound $FePSe_3$ which was discovered a few decades ago[30,100] has so far received surprisingly less attention than

$FePS_3$ despite the fact that both $FePS_3$ [6,40,107] and $FePSe_3$ [30,42] exhibit similar Ising-type zig-zag AFM ordering from bulk to the monolayer limit. This is in stark contrast to the distinct magnetic structures (experimentally or theoretically determined) for sulfide and selenide compounds in some other known MPX_3 such as $MnP(S,Se)_3$ and $NiP(S,Se)_3$.[31,205] Such lack of change in magnetic structure in $FeP(S,Se)_3$ naturally raises a question of whether chalcogen substitution may play any role in modifying magnetic properties, which has been investigated in ref. 122. For the entire composition range, magnetic susceptibility displays strong anisotropy both below and above T_N, with the in-plane susceptibility measured under the in-plane field ($H\|ab$) showing much weaker temperature dependence as compared to the out-of-plane susceptibility [Fig. 15(a)], implying the persistence of the Ising-type magnetism up on Se substitution. In Mn- and Ni-based MPX_3, the magnetic anisotropy mainly originate from anisotropic superexchange interaction that arises from SOC of non-magnetic ligands.[206,207] However, in $FeP(Se_{1-x}S_x)_3$, magnetic anisotropy predominantly stems from the strong crystal electric field on Fe^{2+} ion (discussed in section 4.1.),[138,139] and thus S–Se substitution does not substantially change magnetic anisotropy and consequently maintains the robust Ising-type magnetic ordering in $FeP(Se_{1-x}S_x)_3$.[122]

The evolution of T_N with Se substitution is also interesting. Unlike Mn- and Ni-based MPX_3 in which chalcogen substitution leads to monotonic decrease or increase in T_N, respectively (see sections 4.2.2.1 and 4.2.2.2), in Fe-based system, a non-monotonic dependent is observed[122] [Fig. 15(b)]. This has been attributed to the evolution of magnetic exchange:[122] previous neutron scattering measurement has revealed dominant J_1 in $FePS_3$ [107] (Table 4), which is FM in nature and sensitive to Fe–Fe distance due to direct exchange interaction of the nearest-neighbor Fe moments.[128,188] A similar direct exchange scenario occurs for $MnPS_{3-x}Se_x$ except J_1 is AFM in nature (see sections 4.2.2.1). With the consideration that the competition between FM and AFM correlations determines the magnetic ordering type and transition temperature, the evolution of T_N can be understood in terms of the nearest-neighbor Fe–Fe distance that governs the FM J_1 in $FeP(Se_{1-x}S_x)_3$. As shown in Fig. 15(c), the nearest-neighbor Fe–Fe distance in $FeP(Se_{1-x}S_x)_3$ first reduces with S substitution up to $x = 0.5$. Further increasing S content slightly modifies the lattice structure and leads to elongated Fe–Fe distance. This causes a non-monotonic composition dependence for J_1 and eventually results in non-monotonic evolution for T_N.

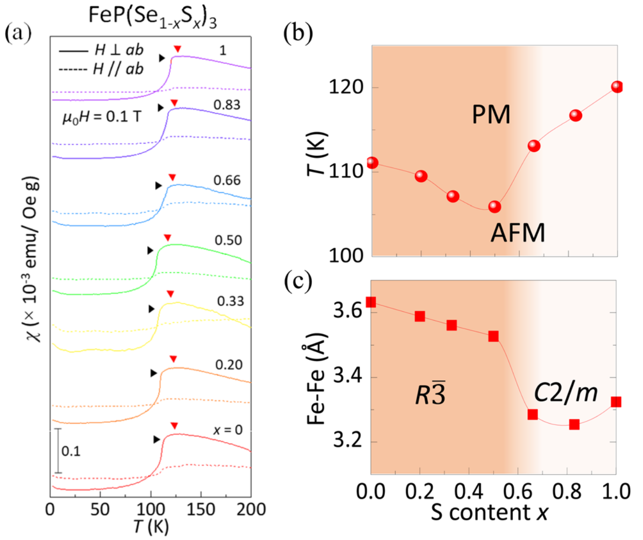

Fig. 15 (a) Temperature dependencies of susceptibility of $FeP(Se_{1-x}S_x)_3$ measured under a magnetic field of 0.1 T. Doping dependence of (b) T_N and (c) Fe–Fe distance for $FeP(Se_{1-x}S_x)_3$.[122]

4.2.3. Inter-layer intercalation. In addition to metal and chalcogen substitutions, the layered structure of MPX_3 allows for another doping strategy – inter-layer intercalation of guest ions, as shown in the schematic in Fig. 4(c). The metal and chalcogen substitutions are all based on the direct mixing of dopants and source materials during synthesis such as flux and chemical vapor transport (CVT). On the other side, the intercalation technique is usually applied to post-grown crystals, involving the insertion of guest ions into inter-layer spaces of the material. So, this method is relatively clean and does not strongly modify the host layers. Generally, intercalation to vdW materials is expected to modulate the inter-layer spacing and may also lead to carrier doping. Therefore, compared to metal M and chalcogen X substitutions, intercalation offers a new approach to tuning the magnetic properties of MPX_3 materials, which may create new magnetic phenomena and novel magnetic phases in MPX_3 that are not accessible by substitution. Intercalation of Li[54,98,100,208,209] and various organic-ions[96,97,99,101] have been reported in MPX_3, which were achieved by electrochemical[54,97–99,208,209] and wet chemical[96,100,101] techniques.

4.2.3.1. Lithium intercalation. Lithium (Li) intercalation in MPX_3 has been reported a long time ago.[54,100,208,209] Earlier work mainly focused on the electrical, optical, and electrochemical properties of Li-intercalated MPX_3. Regarding magnetic properties, the effects of Li intercalation on $NiPS_3$, $FePS_3$, $FePSe_3$, and $MnPSe_3$ compounds were first studied four decades ago.[100] The intercalation was achieved by reacting MPX_3-powered samples and *n*-butyllithium solution in hexane at room temperature in a dry, oxygen-free environment for 10–15 days. The duration of the reaction and concentration of *n*-butyllithium was found to affect the amount of intercalated Li. In this work,[100] resistivity reduction in those powered samples implies successful intercalation. However, magnetic properties including transition temperature, effective moment, and Weiss temperature extracted from temperature-dependent magnetic susceptibility measurements do not display notable changes [Fig. 16(a)].

Recent studies adopting electrochemical interaction to intercalate Li in single crystalline samples reveal modified magnetic properties in Li_xNiPS_3 [98] and Li_xFePS_3.[210] The intercalation in both studies was performed using a battery setup [Fig. 16(b)] and the expanded *c*-axis implies successful interca-

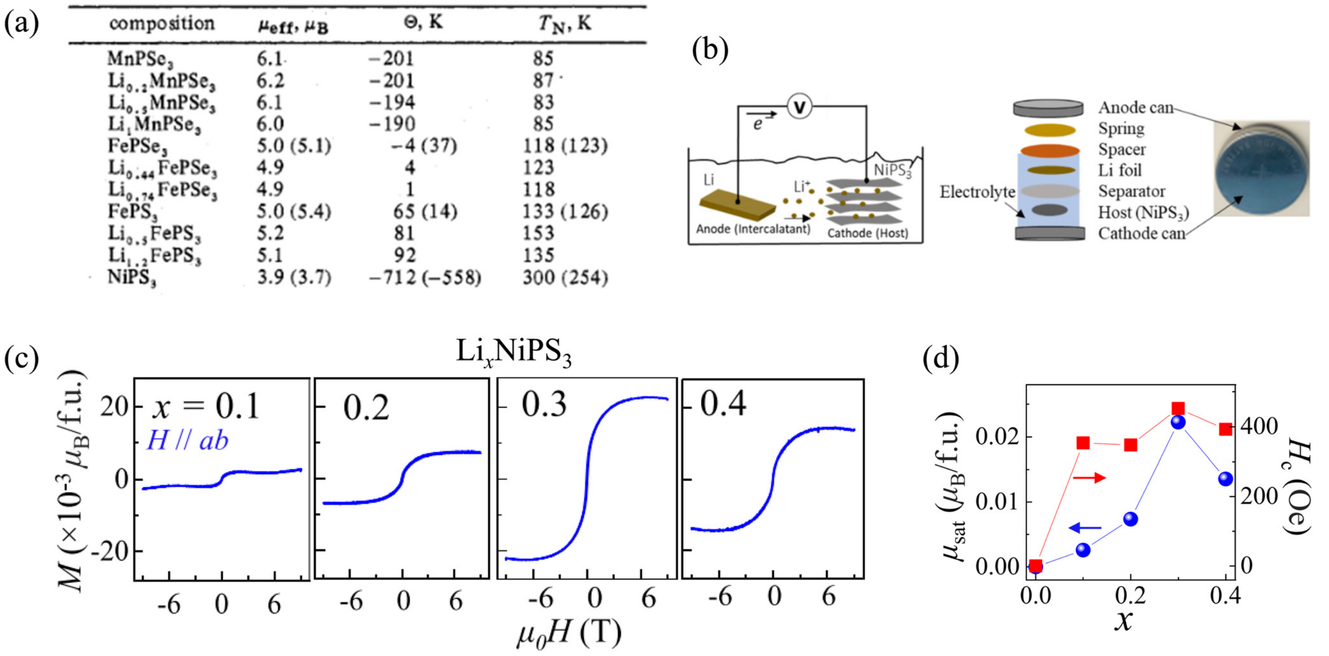

composition	μ_{eff}, μ_B	Θ, K	T_N, K
$MnPSe_3$	6.1	−201	85
$Li_{0.2}MnPSe_3$	6.2	−201	87
$Li_{0.5}MnPSe_3$	6.1	−194	83
Li_1MnPSe_3	6.0	−190	85
$FePSe_3$	5.0 (5.1)	−4 (37)	118 (123)
$Li_{0.44}FePSe_3$	4.9	4	123
$Li_{0.74}FePSe_3$	4.9	1	118
$FePS_3$	5.0 (5.4)	65 (14)	133 (126)
$Li_{0.5}FePS_3$	5.2	81	153
$Li_{1.2}FePS_3$	5.1	92	135
$NiPS_3$	3.9 (3.7)	−712 (−558)	300 (254)

Fig. 16 (a) Magnetic properties for Li_xMnPSe_3, Li_xFePSe_3, Li_xFePS_3, and Li_xNiPS_3.[100] Reprinted (adapted) with permission.[100] Copyright 1979, American Chemical Society. (b) Conceptual schematic of electrochemical intercalation process and the coin cell setup for intercalation.[98] (c) Non-linear field dependence of magnetization of Li_xNiPS_3 at T = 2 K after removing the linear magnetization background.[98] (d) Evolution of saturation moment (μ_{sat}) and coercive fields (H_c) with Li content.[98]

lation. For $NiPS_3$, samples with Li content up to x = 0.4 are air-stable and maintain good crystallinity based on X-ray diffraction and scanning electron microscope imaging, though non-magnetic Li_3PS_4 impurity starts to occur for $x \geq 0.3$. It is worth noting that the Li amount is the nominal content calculated based on the intercalation duration and electrical current because neither X-ray diffraction nor energy dispersive X-ray spectroscopy can directly probe Li. Similar to the earlier study using *n*-butyllithium solution for Li intercalation,[100] the electrochemically intercalated Li_xNiPS_3 (x = 0–0.4) samples do not display clear changes in T_N. However, the development of non-linear field dependence for magnetization, and its saturation-like behavior after removing the linear background [Fig. 16(c)], and the rise of the hysteresis loop and tiny magnetic moment [Fig. 16(d)] have been ascribed to ferrimagnetism due to uncompensated antiparallel magnetic moments.[98] For $FePS_3$,[210] in contrast, T_N is found to be reduced with the expansion of the *c*-axis by Li-intercalation, suggesting a possible role of inter-layer magnetic exchange. The Ising-type magnetism characterized by strong anisotropy in magnetic susceptibility in the high-temperature paramagnetic state remains robust. At low temperatures, non-linear field dependence for magnetization is also observed, similar to Li-intercalated $NiPS_3$.

4.2.3.2. Organic-ion intercalation. The vdW gap allows for not only the intercalation of small Li atoms or ions but also the much larger organic molecules or ions.[96,97,99,211,212] Organic ion intercalation has been mainly performed on $NiPS_3$.[96,97,99] Intercalating tetraheptyl ammonium (THA^+),[97] tetrabutylammonium (TBA^+),[99] cobaltocenium ions [$Co(Cp)_2{}^+$, where Cp is a cyclopentadienyl ring $C_5H_5{}^-$],[99] and 1,10-phenanthroline[96] using electrochemical[97,99] and solution reaction[96] have been performed. Compared to Li-intercalation, intercalating large organic ions results in a much more significant elongation of inter-layer spacing.[96,97,99] It has also been found that the intralayer lattice structure does not display remarkable change upon intercalation.[96]

Organic-ions intercalation in $NiPS_3$ is found to drastically modify the magnetic properties,[96,97,99] mainly giving rise to a low-temperature FIM state[97,99] that is also reported in Li-intercalated $NiPS_3$ [98] described in the previous section. The conclusion has been drawn based on the transition-like sharp susceptibility upturn around and below 100 K [Fig. 17(a) and (c)], as well as magnetic hysteresis loops in THA^+-,[97] TBA^+-,[99] and $Co(Cp)_2{}^+$ (ref. 99)-intercalated $NiPS_3$ [Fig. 17(b) and (d)]. It has been proposed[99] that the cation intercalation causes the reduction of certain Ni from the Ni^{2+} to the Ni^0 state, together with its displacement from the O_h to the T_d lattice site. Such transition from high spin Ni^{2+}–O_h atoms ([Ar]$3d^8s^0$) to zero-spin Ni^0–T_d ([Ar]$3d^{10}s^0$) leads to uncompensated antiferromagnetism, *i.e.* a FIM state. An alternative mechanism based on the Stoner effect has also been proposed:[97] the charge doping due to organic-ion intercalation enhances the density of states (DOS) at the Fermi level and eventually triggers the inter-chain Stoner splitting of the itinerant electrons, resulting in the higher electron concentration in one Ni chain to create net magnetic moment which gives rise to ferrimagnetism.

Recently, a new method using iron dopant as reaction active sites to intercalating organic-ion in $NiPS_3$ has been

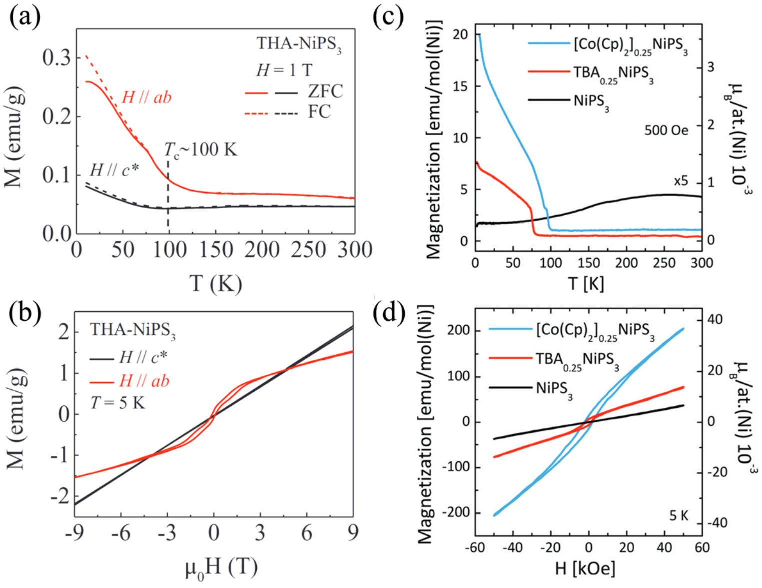

Fig. 17 (a) Temperature and (b) field dependencies of magnetization of intercalated THA-$NiPS_3$.[97] (c) Field-cooled temperature-dependent magnetization and (d) magnetic hysteresis for $NiPS_3$, $TBA_{0.25}NiPS_3$, and $[Co(Cp)_2]_{0.25}NiPS_3$.[99]

reported.[96] In this method, light Fe-substituted $NiPS_3$ (*i.e.*, $Fe_{0.02}Ni_{0.98}PS_3$) single crystals are synthesized, which is followed by intercalation of a complexing agent 1,10-phenanthroline by solution reaction with aniline chloride.[96] In this process, 1,10-phenthroline removes Fe^{2+} ions into the solution, creating metal-ion vacancies. The aniline chloride provides a proton to 1,10-phenthroline, and such protonated 1,10-phenanthroline is attracted towards the vacant metal sites, forcing intercalation of 1,10-phenanthroline into inter-layer spacing. The intercalated samples also display the signature of ferrimagnetism.

5. Engineering magnetism through pressure

In addition to chemical doping, pressure has also been established as an efficient external stimulus to tune magnetic properties. In MPX_3, high pressure has been found to effectively modulate electronic properties.[64–72] Recently, pressure has also been used to control magnetism in this material family.[213–216] A recent review article has extensively summarized the theoretical and experimental progress of the structural, electronic, magnetic, and optical properties tuning of MPX_3 under pressure.[217] In this review, we focus on engineering magnetism in MPX_3 materials. Since pressure generally tunes lattice structures and possibly induces structure transitions, it also sheds light on tuning magnetism through changing magnetic exchange and anisotropy. Therefore, here we briefly describe the pressure-driven modification of magnetism in MPX_3. The magnetic properties of MPX_3 are found to be sensitive to high pressure. T_N systematically increases with the pressure for $MnPS_3$[213,216] and $FePS_3$,[214] which can be explained by the enhanced magnetic interactions under pressure. In particular, compressing the crystal planes closer strengthens the inter-layer interaction.[214,216] For $MnPS_3$, the T_N also enhances with applying pressure, with different reported rates of 6.7 K GPa^{-1} (ref. 213) and 13 K GPa^{-1} (ref. 216) depending on the type of samples (polycrystal or single crystal). In addition, SF transition is tunable by pressure. In $MnPS_3$,[216] the SF field decreases at a rate of 4.0×10^3 Oe GPa^{-1}, which is likely due to the reduction of magnetic anisotropy under pressure. Furthermore, the magnetic structure for $MnPS_3$ remains unchanged up to ~3.6 GPa (ref. 213) but changes at ~2 GPa for $FePS_3$[214] and ~4 GPa for $NiPSe_3$.[215] Such changes in magnetic structures are accompanied by the insulator-to-metal transition and even superconductivity in $FePSe_3$[72] and $NiPSe_3$.[215] Therefore, high pressure, as well as strain, are excellent tools that can be combined with chemical tuning (substitution and intercalation) to achieve additional properties, such as the combination of the desired magnetic structure and electrical conductivity.

6. Summary and perspectives

In this review article, we provide a summary covering the crystal growth, structure, and magnetic properties of the vdW-type AFM MPX_3 material family, with a focus on property tuning by various doping scenarios. Metal substitution, chalcogen substitution, and inter-layer intercalation are highly effective in tuning the magnetic properties in MPX_3, including magnetic ordering, exchange interactions, magnetic anisotropy, *etc.* Generally, AFM ground states are robust, and most of those metal and chalcogen substitution tune properties within antiferromagnetism, except for a few cases such as $Fe_{1-x}Zn_xPS_3$ and $AgVP_2Se_6$ that display FM-like behaviors such as irreversibility, hysteresis, and saturation magnetization. However, magnetization is not a bulk measurement as a tiny number of magnetic impurities may give rise to a strong magnetization signal. Also, quite a few FM-like signatures may originate from a spin–flip transition or a canted AFM state, as seen in AFM $CuCrP_2S_6$ and $Ni_{1-x}Cr_xPS_3$. Therefore, other bulk measurements such as neutron diffraction are needed to clarify the magnetic ground state as well as any field-induced phase transitions. Indeed, the rapid development of MPX_3 and its derivatives calls for more neutron resource allocations on these interesting vdW magnetic compounds.

On the other hand, intercalations of a few guest species have been reported to result in a FIM state at low temperatures. The differences in substitution and intercalation might be attributed to different consequences: substitution within each individual layer plays a role mainly in altering magnetic anisotropy and exchange interactions while intercalation in the inter-layer spacing might lead to carrier doping or reductive reaction for metal ions. Also, intercalation is efficient in tuning inter-layer distance, especially when intercalating large ions such as organic intercalation. This effectively reduces interlayer interaction and may push the magnetism approach to a 2D limit. Therefore, intercalation might be a good tool to engineering magnetism for compounds in which the inter-layer exchange J_z is important. So far, there are not many reported intercalation studies, therefore more efforts toward this direction are needed to fully explore this promising material tuning approach. Similarly, a direct probe for magnetic ordering such as neutron diffraction is also highly desired in this direction. Another urgent need is an accurate and convenient approach to determine the amount of Li for Li-intercalated samples.

High-entropy (HE) MPX_3 is an emerging field with great opportunities owing to the expanded degrees of freedom. The combination of multiple elements in HE compounds offers greater versatility and tunability of material properties as compared to conventional bi-metallic and bi-chalcogenide alloys by varying the composition of M and X elements. Incorporating multiple components in an HE compound could induce a severe lattice distortion due to the difference in their atomic sizes, which provides opportunities for crystal structure and symmetry engineering for possible novel functional properties. The HE alloys are expected to generate unusual magnetic orderings due to competing magnetic interactions enabled by the interplay between spin, charge, and orbital degrees of freedom.[218] On the other side, the randomness introduced by high entropy may also quench the magnetic order and simultaneously facilitate the insulator-to-metal transition and subsequent emergence of superconductivity, which may be extremely challenging but has been observed in $FePSe_3$-based HE compounds under external pressure.[121] Further exploring HE MPX_3 compounds could provide pathways to realize enhanced conductivity and even superconductivity at an ambient pressure or much lower pressure. Understanding the effect of entropy on the structural stability and material properties of complex HE compounds is critical for their optimal design and utilization in practical applications. However, the controlled synthesis of the alloy composition, and the large parameter space, pose significant challenges for controlled study (*e.g.*, fixing the content of one or more metals) to clarify the mechanism behind the property changes. More effort, especially in synthesis and applying additional experimental tools, would be beneficial.

One driving force of the study of MPX_3 is the feasibility of obtaining their atomically thin layers that provide invaluable opportunities for studying new phenomena originating from 2D magnetism and future device applications. The tunable magnetism summarized in this review further demonstrates the great potential of this material platform. Despite their well-established magnetic orders in bulk materials and the fact of being one of a few first demonstrated 2D magnets in the atomically thin layer form, the study of 2D magnetism in MPX_3 is still in an early stage with only a few pristine compositions being investigated, as summarized in Table 6. It has been found that the long-range magnetic orders in atomically mono- or bi-layers only exist in a few MPX_3 compounds such as $MnPS_3$,[29,109] $FePS_3$,[6] $NiPS_3$,[60] $CoPS_3$,[108] $MnPSe_3$,[43] and $FePSe_3$.[42] Whereas the 2D magnetism in substituted and intercalated MPX_3 compounds remains elusive. So far, few challenges to exploring magnetism in 2D have been identified in the MPX_3 family. First, because of the absence of net magnetization, direct probe of AFM states in 2D layers of MPX_3 is challenging by using nanoscale magnetic characterization techniques such as scanning single-spin magnetometry,[219] magneto-optical Kerr effect microscopy,[7,8] polar reflective magnetic circular dichroism (RMCD),[10] X-ray magnetic dichroism (XMCD),[167] and optical linear dichroism (LD).[48,220] In addition to developing more experimental techniques for probing AFM state in nanoscale, inducing ferromagnetism in MPX_3 can be a shortcut for 2D magnetism study. We hope the various doping techniques summarized in this review can provide some insight into creating FM ground states for field-driven polarized FM states in these materials. Another advantage of inducing ferromagnetism is the breaking of time-reversal symmetry that may bring in other exotic phenomena. Recent studies have predicted the non-trivial topological states in the FM phase of MPX_3,[221,222] providing a rare platform for investi-

Table 6 Summary of magnetic ordering in atomically thin layers of MPX_3 compounds

Compounds	Magnetic ordering temperature (K)			Ref.
	Monolayer	Bilayer	Bulk	
$MnPS_3$	—[a]	78	78	29 and 109
$FePS_3$	118	118	118	6
$NiPS_3$	—[a]	130	155	60
$CoPS_3$	100	100	120	108 and 129
$MnPSe_3$	40	56	74	43
$FePSe_3$	98	102	111	42

[a] Magnetic order not stable in the monolayer.

gating the interplay between magnetism and band topology in the 2D limit.

Although this review mainly focuses on magnetism, we wish to take this opportunity to comment on the electronic properties of MPX_3. Those materials are well-known wide band gap insulators and electronic transport measurements in bulk materials are almost impossible or only possible in the high-temperature range.[71,197] Enabling electronic studies in vdW-type magnetic MPX_3 could be an important direction. Exploiting the coupling between magnetic and electronic properties would provide a platform for tunable electrical properties to develop quantum materials and devices with multifunctional magnetic and electronic properties. Therefore, though applying high pressure has been demonstrated to be effective,[64–72] further development in approaches or materials that are compatible with 2D magnetism and device integration is critical, which calls for synergistic efforts in material modeling, high-throughput calculations, synthesis, characterization, and device study.

The vdW structure of MPX_3 materials is naturally advantageous for fabricating devices for electronic and optoelectronic applications. However, the highly insulating nature of MPX_3 materials has somewhat hindered the rapid development of device applications. To the best of our knowledge, so far the field-effect transistors (FET) using atomically thin layers of only a few MPX_3 compounds such as $NiPS_3$ [223] and $MnPS_3$ [53] have been reported. The FET based on $NiPS_3$ [223] and $MnPS_3$ [53] thin flakes have been found to exhibit n-type and p-type semiconducting behavior with on/off ratios of $\sim 10^3$–10^5 and $\sim 10^2$–10^3 respectively at room temperature, with low charge carrier mobilities of ~ 0.5–$1\ cm^2\ V^{-1}\ s^{-1}$ and $8.3 \times 10^{-3}\ cm^2\ V^{-1}\ s^{-1}$ respectively. On the other hand, recent works have mainly focused on optoelectronic devices such as photodetectors,[52,224–226] phototransistors,[227,228] and sensors[229] based on a few layers of MPX_3. High-performance and sensitive photodetectors working in a wide frequency range from near-infrared[226] to ultraviolet[52] have been successfully fabricated using the thin layers of $MnPS_3$,[53] $FePS_3$,[52,224] $MnPSe_3$,[225] and $FePSe_3$.[226] The few layers $NiPS_3$ [228] and $MnPSe_3$ [227] have also been integrated into phototransistors for ultrasensitive light detection. Furthermore, the $MnPS_3$ thin flakes[229] has been demonstrated as sensors for sensitive and selective moisture sensing. Providing this progress, efficiently tuning the magnetism would possibly lead to new optoelectronic and photonic applications, especially the light polarization-based applications for which magnetism can play a role. Furthermore, metalizing MPX_3 *via* combined chemical and strain may pave a way for electronic applications.

Finally, more attention should be given to atomic ordering in these substituted and intercalated compounds. The distribution of the dopants and possibly the associated vacancies may play important roles in mediating properties. The ultimate examples are well-defined atomic orderings such as superlattice or Peierls transition, which can be relatively easily probed by high-resolution structure characterization tools such as High-resolution/Scanning transmission electron microscopy (HRTEM/STEM) and synchrotron XRD. However, chemical short-range order, which is another ultimate example, is difficult to characterize and has not been widely studied in crystalline solids. Such chemical short-range order is distinct from the well-known short-range order in condensed matter physics that is defined from the long-range ordering. Roughly speaking, the long-range order is based on periodic ordering with long-range correlation length, while the short-range order is normally referred to as similar ordering but with much-shortened correlation length, which usually occurs with the disturbance of the long-range order by doping or increasing the temperature to around the phase transition temperature. In contrast, chemical short-range order occurs in a doped system and characterizes the deviation of the atomic distribution from the *perfect random distributions*. The study started from the III–V semiconductor alloys decades ago which mainly focused on long-range order,[230] and has been recently extended to chemical short-range order in other systems such as group-IV semiconductors,[231,232] metal alloys,[233,234] thermoelectric materials,[235,236] and oxides.[237] Thus far, chemical short-range order remains to be an extremely less-explored topic in condensed matter physics, probably owing to the lack of efficient experimental tools to probe it. In doped MPX_3 systems, chemical short-range order should also occur and may affect the magnetic properties. Providing rich and tunable magnetism, the doped MPX_3 compounds provide an ideal platform for studying the nature of the possible various chemical short-range orders in vdW materials and their impacts on magnetism, which is a new field awaiting exploration.

Author contributions

R. B. and J. H. designed, wrote, and edited this manuscript.

Data availability

No primary research results, software or code have been included and no new data were generated as part of this review.

Conflicts of interest

The authors declare no conflict of interest.

Acknowledgements

R. B. acknowledges the support from μ-ATOMS, an Energy Frontier Research Center funded by DOE, Office of Science, Basic Energy Sciences, under Award DE-SC0023412. J. H. acknowledges the support from the U.S. Department of Energy, Office of Science, Basic Energy Sciences program under Grant No. DE-SC0022006. The authors are grateful to T. Li at George Washington University for informative discussions.

References

1 K. S. Novoselov, A. K. Geim, S. V. Morozov, D. Jiang, Y. Zhang, S. V. Dubonos, I. V. Grigorieva and A. A. Firsov, *Science*, 2004, **306**, 666–669.

2 W. Han, R. K. Kawakami, M. Gmitra and J. Fabian, *Nat. Nanotechnol.*, 2014, **9**, 794–807.

3 B. Li, T. Xing, M. Zhong, L. Huang, N. Lei, J. Zhang, J. Li and Z. Wei, *Nat. Commun.*, 2017, **8**, 1958.

4 Z. Guguchia, A. Kerelsky, D. Edelberg, S. Banerjee, F. von Rohr, D. Scullion, M. Augustin, M. Scully, D. A. Rhodes, Z. Shermadini, H. Luetkens, A. Shengelaya, C. Baines, E. Morenzoni, A. Amato, J. C. Hone, R. Khasanov, S. J. L. Billinge, E. Santos, A. N. Pasupathy and Y. J. Uemura, *Sci. Adv.*, 2018, **4**, eaat3672.

5 K.-T. Ko, K. Kim, S. B. Kim, H.-D. Kim, J.-Y. Kim, B. I. Min, J.-H. Park, F.-H. Chang, H.-J. Lin, A. Tanaka and S.-W. Cheong, *Phys. Rev. Lett.*, 2011, **107**, 247201.

6 J.-U. Lee, S. Lee, J. H. Ryoo, S. Kang, T. Y. Kim, P. Kim, C.-H. Park, J.-G. Park and H. Cheong, *Nano Lett.*, 2016, **16**, 7433–7438.

7 B. Huang, G. Clark, E. Navarro-Moratalla, D. R. Klein, R. Cheng, K. L. Seyler, D. Zhong, E. Schmidgall, M. A. McGuire, D. H. Cobden, W. Yao, D. Xiao, P. Jarillo-Herrero and X. Xu, *Nature*, 2017, **546**, 270–273.

8 C. Gong, L. Li, Z. Li, H. Ji, A. Stern, Y. Xia, T. Cao, W. Bao, C. Wang, Y. Wang, Z. Q. Qiu, R. J. Cava, S. G. Louie, J. Xia and X. Zhang, *Nature*, 2017, **546**, 265–269.

9 Z. Zhang, J. Shang, C. Jiang, A. Rasmita, W. Gao and T. Yu, *Nano Lett.*, 2019, **19**, 3138–3142.

10 Z. Lin, B. Huang, K. Hwangbo, Q. Jiang, Q. Zhang, Z. Liu, Z. Fei, H. Lv, A. Millis, M. McGuire, D. Xiao, J.-H. Chu and X. Xu, *Nano Lett.*, 2021, **21**, 9180–9186.

11 Z. Fei, B. Huang, P. Malinowski, W. Wang, T. Song, J. Sanchez, W. Yao, D. Xiao, X. Zhu, A. F. May, W. Wu, D. H. Cobden, J.-H. Chu and X. Xu, *Nat. Mater.*, 2018, **17**, 778–782.

12 G. Zhang, F. Guo, H. Wu, X. Wen, L. Yang, W. Jin, W. Zhang and H. Chang, *Nat. Commun.*, 2022, **13**, 5067.

13 S. Albarakati, C. Tan, Z.-J. Chen, J. G. Partridge, G. Zheng, L. Farrar, E. L. H. Mayes, M. R. Field, C. Lee, Y. Wang, Y. Xiong, M. Tian, F. Xiang, A. R. Hamilton, O. A. Tretiakov, D. Culcer, Y.-J. Zhao and L. Wang, *Sci. Adv.*, 2019, **5**, eaaw0409.

14 S. Jiang, L. Li, Z. Wang, K. F. Mak and J. Shan, *Nat. Nanotechnol.*, 2018, **13**, 549–553.

15 Z. Wang, T. Zhang, M. Ding, B. Dong, Y. Li, M. Chen, X. Li, J. Huang, H. Wang, X. Zhao, Y. Li, D. Li, C. Jia, L. Sun, H. Guo, Y. Ye, D. Sun, Y. Chen, T. Yang, J. Zhang, S. Ono, Z. Han and Z. Zhang, *Nat. Nanotechnol.*, 2018, **13**, 554–559.

16 B. Huang, G. Clark, D. R. Klein, D. MacNeill, E. Navarro-Moratalla, K. L. Seyler, N. Wilson, M. A. McGuire, D. H. Cobden, D. Xiao, W. Yao, P. Jarillo-Herrero and X. Xu, *Nat. Nanotechnol.*, 2018, **13**, 544–548.

17 Y. Deng, Y. Yu, Y. Song, J. Zhang, N. Z. Wang, Z. Sun, Y. Yi, Y. Z. Wu, S. Wu, J. Zhu, J. Wang, X. H. Chen and Y. Zhang, *Nature*, 2018, **563**, 94–99.

18 T. Song, X. Cai, M. W.-Y. Tu, X. Zhang, B. Huang, N. P. Wilson, K. L. Seyler, L. Zhu, T. Taniguchi, K. Watanabe, M. A. McGuire, D. H. Cobden, D. Xiao, W. Yao and X. Xu, *Science*, 2018, **360**, 1214–1218.

19 Y. Wu, S. Zhang, J. Zhang, W. Wang, Y. L. Zhu, J. Hu, G. Yin, K. Wong, C. Fang, C. Wan, X. Han, Q. Shao, T. Taniguchi, K. Watanabe, J. Zang, Z. Mao, X. Zhang and K. L. Wang, *Nat. Commun.*, 2020, **11**, 3860.

20 D. R. Klein, D. MacNeill, J. L. Lado, D. Soriano, E. Navarro-Moratalla, K. Watanabe, T. Taniguchi, S. Manni, P. Canfield, J. Fernández-Rossier and P. Jarillo-Herrero, *Science*, 2018, **360**, 1218–1222.

21 J. Shang, X. Tang, X. Tan, A. Du, T. Liao, S. C. Smith, Y. Gu, C. Li and L. Kou, *ACS Appl. Nano Mater.*, 2020, **3**, 1282–1288.

22 D. Zhong, K. L. Seyler, X. Linpeng, R. Cheng, N. Sivadas, B. Huang, E. Schmidgall, T. Taniguchi, K. Watanabe, M. A. McGuire, W. Yao, D. Xiao, K.-M. C. Fu and X. Xu, *Sci. Adv.*, 2017, **3**, e1603113.

23 Z. Wang, I. Gutiérrez-Lezama, N. Ubrig, M. Kroner, M. Gibertini, T. Taniguchi, K. Watanabe, A. Imamoğlu, E. Giannini and A. F. Morpurgo, *Nat. Commun.*, 2018, **9**, 2516.

24 T. Song, M. W.-Y. Tu, C. Carnahan, X. Cai, T. Taniguchi, K. Watanabe, M. A. McGuire, D. H. Cobden, D. Xiao, W. Yao and X. Xu, *Nano Lett.*, 2019, **19**, 915–920.

25 Y. Wang, J. Balgley, E. Gerber, M. Gray, N. Kumar, X. Lu, J.-Q. Yan, A. Fereidouni, R. Basnet, S. J. Yun, D. Suri, H. Kitadai, T. Taniguchi, K. Watanabe, X. Ling, J. Moodera, Y. H. Lee, H. O. H. Churchill, J. Hu, L. Yang, E.-A. Kim, D. G. Mandrus, E. A. Henriksen and K. S. Burch, *Nano Lett.*, 2020, **20**, 8446–8452.

26 K. F. Mak, J. Shan and D. C. Ralph, *Nat. Rev. Phys.*, 2019, **1**, 646–661.

27 F. Wang, T. A. Shifa, P. Yu, P. He, Y. Liu, F. Wang, Z. Wang, X. Zhan, X. Lou, F. Xia and J. He, *Adv. Funct. Mater.*, 2018, **28**, 1802151.

28 R. Samal, G. Sanyal, B. Chakraborty and C. S. Rout, *J. Mater. Chem. A*, 2021, **9**, 2560–2591.

29 G. Long, H. Henck, M. Gibertini, D. Dumcenco, Z. Wang, T. Taniguchi, K. Watanabe, E. Giannini and A. F. Morpurgo, *Nano Lett.*, 2020, **20**, 2452–2459.

30 A. Wiedenmann, J. Rossat-Mignod, A. Louisy, R. Brec and J. Rouxel, *Solid State Commun.*, 1981, **40**, 1067–1072.

31 R. Basnet, K. M. Kotur, M. Rybak, C. Stephenson, S. Bishop, C. Autieri, M. Birowska and J. Hu, *Phys. Rev. Res.*, 2022, **4**, 023256.

32 H. Han, H. Lin, W. Gan, Y. Liu, R. Xiao, L. Zhang, Y. Li, C. Zhang and H. Li, *Appl. Phys. Lett.*, 2023, **122**, 033101.

33 A. R. Wildes, V. Simonet, E. Ressouche, G. J. Mcintyre, M. Avdeev, E. Suard, S. A. Kimber, D. Lançon, G. Pepe and B. Moubaraki, *Phys. Rev. B: Condens. Matter Mater. Phys.*, 2015, **92**, 224408.

34 A. R. Wildes, H. M. Rønnow, B. Roessli, M. J. Harris and K. W. Godfrey, *Phys. Rev. B: Condens. Matter Mater. Phys.*, 2006, **74**, 094422.

35 A. R. Wildes, B. Roessli, B. Lebech and K. W. Godfrey, *J. Phys.: Condens. Matter*, 1998, **10**, 6417–6428.

36 A. R. Wildes, V. Simonet, E. Ressouche, R. Ballou and G. J. McIntyre, *J. Phys.: Condens. Matter*, 2017, **29**, 455801.

37 T. Sekine, M. Jouanne, C. Julien and M. Balkanski, *Phys. Rev. B: Condens. Matter Mater. Phys.*, 1990, **42**, 8382–8393.

38 Y. Takano, N. Arai, A. Arai, Y. Takahashi, K. Takase and K. Sekizawa, *J. Magn. Magn. Mater.*, 2004, **272–276**, E593–E595.

39 G. Le Flem, R. Brec, G. Ouvard, A. Louisy and P. Segransan, *J. Phys. Chem. Solids*, 1982, **43**, 455–461.

40 P. A. Joy and S. Vasudevan, *Phys. Rev. B: Condens. Matter Mater. Phys.*, 1992, **46**, 5425–5433.

41 G. Long, T. Zhang, X. Cai, J. Hu, C. Cho, S. Xu, J. Shen, Z. Wu, T. Han, J. Lin, J. Wang, Y. Cai, R. Lortz, Z. Mao and N. Wang, *ACS Nano*, 2017, **11**, 11330–11336.

42 J. Luo, S. Li, Z. Ye, R. Xu, H. Yan, J. Zhang, G. Ye, L. Chen, D. Hu, X. Teng, W. A. Smith, B. I. Yakobson, P. Dai, A. H. Nevidomskyy, R. He and H. Zhu, *Nano Lett.*, 2023, **23**, 2023–2030.

43 Z. Ni, A. V. Haglund, H. Wang, B. Xu, C. Bernhard, D. G. Mandrus, X. Qian, E. J. Mele, C. L. Kane and L. Wu, *Nat. Nanotechnol.*, 2021, **16**, 782–787.

44 S. Kang, K. Kim, B. H. Kim, J. Kim, K. I. Sim, J.-U. Lee, S. Lee, K. Park, S. Yun, T. Kim, A. Nag, A. Walters, M. Garcia-Fernandez, J. Li, L. Chapon, K.-J. Zhou, Y.-W. Son, J. H. Kim, H. Cheong and J.-G. Park, *Nature*, 2020, **583**, 785–789.

45 X. Wang, J. Cao, Z. Lu, A. Cohen, H. Kitadai, T. Li, Q. Tan, M. Wilson, C. H. Lui, D. Smirnov, S. Sharifzadeh and X. Ling, *Nat. Mater.*, 2021, **20**, 964–970.

46 F. Dirnberger, R. Bushati, B. Datta, A. Kumar, A. H. MacDonald, E. Baldini and V. M. Menon, *Nat. Nanotechnol.*, 2022, **17**, 1060–1064.

47 K. Hwangbo, Q. Zhang, Q. Jiang, Y. Wang, J. Fonseca, C. Wang, G. M. Diederich, D. R. Gamelin, D. Xiao, J.-H. Chu, W. Yao and X. Xu, *Nat. Nanotechnol.*, 2021, **16**, 655–660.

48 H. Zhang, Z. Ni, C. E. Stevens, A. Bai, F. Peiris, J. R. Hendrickson, L. Wu and D. Jariwala, *Nat. Photonics*, 2022, **16**, 311–317.

49 C. A. Belvin, E. Baldini, I. O. Ozel, D. Mao, H. C. Po, C. J. Allington, S. Son, B. H. Kim, J. Kim, I. Hwang, J. H. Kim, J.-G. Park, T. Senthil and N. Gedik, *Nat. Commun.*, 2021, **12**, 4837.

50 D. Afanasiev, J. R. Hortensius, M. Matthiesen, S. Mañas-Valero, M. Šiškins, M. Lee, E. Lesne, H. S. J. van der Zant, P. G. Steeneken, B. A. Ivanov, E. Coronado and A. D. Caviglia, *Sci. Adv.*, 2021, **7**, eabf3096.

51 J. Chu, F. Wang, L. Yin, L. Lei, C. Yan, F. Wang, Y. Wen, Z. Wang, C. Jiang, L. Feng, J. Xiong, Y. Li and J. He, *Adv. Funct. Mater.*, 2017, **27**, 1701342.

52 Y. Gao, S. Lei, T. Kang, L. Fei, C.-L. Mak, J. Yuan, M. Zhang, S. Li, Q. Bao, Z. Zeng, Z. Wang, H. Gu and K. Zhang, *Nanotechnology*, 2018, **29**, 244001.

53 R. Kumar, R. N. Jenjeti, M. P. Austeria and S. Sampath, *J. Mater. Chem. C*, 2019, **7**, 324–329.

54 A. H. Thompson and M. S. Whittingham, *Mater. Res. Bull.*, 1977, **12**, 741–744.

55 P. J. S. Foot, T. Katz, S. N. Patel, B. A. Nevett, A. R. Pieecy and A. A. Balchin, *Phys. Status Solidi A*, 1987, **100**, 11–29.

56 F. Liu, L. You, K. L. Seyler, X. Li, P. Yu, J. Lin, X. Wang, J. Zhou, H. Wang, H. He, S. T. Pantelides, W. Zhou, P. Sharma, X. Xu, P. M. Ajayan, J. Wang and Z. Liu, *Nat. Commun.*, 2016, **7**, 12357.

57 A. Belianinov, Q. He, A. Dziaugys, P. Maksymovych, E. Eliseev, A. Borisevich, A. Morozovska, J. Banys, Y. Vysochanskii and S. V. Kalinin, *Nano Lett.*, 2015, **15**, 3808–3814.

58 W. F. Io, S.-Y. Pang, L. W. Wong, Y. Zhao, R. Ding, J. Mao, Y. Zhao, F. Guo, S. Yuan, J. Zhao, J. Yi and J. Hao, *Nat. Commun.*, 2023, **14**, 7304.

59 C. B. Park, A. Shahee, K.-T. Kim, D. R. Patil, S. A. Guda, N. Ter-Oganessian and K. H. Kim, *Adv. Electron. Mater.*, 2022, **8**, 2101072.

60 K. Kim, S. Y. Lim, J.-U. Lee, S. Lee, T. Y. Kim, K. Park, G. S. Jeon, C.-H. Park, J.-G. Park and H. Cheong, *Nat. Commun.*, 2019, **10**, 345.

61 K. Du, X. Wang, Y. Liu, P. Hu, M. I. B. Utama, C. K. Gan, Q. Xiong and C. Kloc, *ACS Nano*, 2016, **10**, 1738–1743.

62 Y. Jin, M. Yan, T. Kremer, E. Voloshina and Y. Dedkov, *Sci. Rep.*, 2022, **12**, 735.

63 A. Kamata, K. Noguchi, K. Suzuki, H. Tezuka, T. Kashiwakura, Y. Ohno and S. Nakai, *J. Phys. Soc. Jpn.*, 1997, **66**, 401–407.

64 H.-S. Kim, K. Haule and D. Vanderbilt, *Phys. Rev. Lett.*, 2019, **123**, 236401.

65 Y. Wang, Z. Zhou, T. Wen, Y. Zhou, N. Li, F. Han, Y. Xiao, P. Chow, J. Sun, M. Pravica, A. L. Cornelius, W. Yang and Y. Zhao, *J. Am. Chem. Soc.*, 2016, **138**, 15751–15757.

66 R. A. Evarestov and A. Kuzmin, *J. Comput. Chem.*, 2020, **41**, 1337–1344.

67 M. Tsurubayashi, K. Kodama, M. Kano, K. Ishigaki, Y. Uwatoko, T. Watanabe, K. Takase and Y. Takano, *AIP Adv.*, 2018, **8**, 101307.

68 C. R. S. Haines, M. J. Coak, A. R. Wildes, G. I. Lampronti, C. Liu, P. Nahai-Williamson, H. Hamidov, D. Daisenberger and S. S. Saxena, *Phys. Rev. Lett.*, 2018, **121**, 266801.

69 M. J. Coak, D. M. Jarvis, H. Hamidov, C. R. S. Haines, P. L. Alireza, C. Liu, S. Son, I. Hwang, G. I. Lampronti, D. Daisenberger, P. Nahai-Williamson, A. R. Wildes, S. S. Saxena and J.-G. Park, *J. Phys.: Condens. Matter*, 2019, **32**, 124003.

70 X. Ma, Y. Wang, Y. Yin, B. Yue, J. Dai, J. Cheng, J. Ji, F. Jin, F. Hong, J.-T. Wang, Q. Zhang and X. Yu, *Sci. China: Phys., Mech. Astron.*, 2021, **64**, 297011.

71 M. J. Coak, S. Son, D. Daisenberger, H. Hamidov, C. R. S. Haines, P. L. Alireza, A. R. Wildes, C. Liu, S. S. Saxena and J.-G. Park, *npj Quantum Mater.*, 2019, **4**, 1–6.

72 Y. Wang, J. Ying, Z. Zhou, J. Sun, T. Wen, Y. Zhou, N. Li, Q. Zhang, F. Han, Y. Xiao, P. Chow, W. Yang, V. V. Struzhkin, Y. Zhao and H. Mao, *Nat. Commun.*, 2018, **9**, 1914.

73 S. Y. Kim, T. Y. Kim, L. J. Sandilands, S. Sinn, M.-C. Lee, J. Son, S. Lee, K.-Y. Choi, W. Kim, B.-G. Park, C. Jeon, H.-D. Kim, C.-H. Park, J.-G. Park, S. J. Moon and T. W. Noh, *Phys. Rev. Lett.*, 2018, **120**, 136402.

74 S. Liu, A. Granados del Águila, D. Bhowmick, C. K. Gan, T. Thu Ha Do, M. A. Prosnikov, D. Sedmidubský, Z. Sofer, P. C. M. Christianen, P. Sengupta and Q. Xiong, *Phys. Rev. Lett.*, 2021, **127**, 097401.

75 M. A. Susner, M. Chyasnavichyus, M. A. McGuire, P. Ganesh and P. Maksymovych, *Adv. Mater.*, 2017, **29**, 1602852.

76 N. Chandrasekharan and S. Vasudevan, *Phys. Rev. B: Condens. Matter Mater. Phys.*, 1996, **54**, 14903–14906.

77 D. J. Goossens, A. J. Studer, S. J. Kennedy and T. J. Hicks, *J. Phys.: Condens. Matter*, 2000, **12**, 4233–4242.

78 A. M. Mulders, J. C. P. Klaasse, D. J. Goossens, J. Chadwick and T. J. Hicks, *J. Phys.: Condens. Matter*, 2002, **14**, 8697–8705.

79 Y. Takano, A. Arai, Y. Takahashi, K. Takase and K. Sekizawa, *J. Appl. Phys.*, 2003, **93**, 8197–8199.

80 J. N. Graham, M. J. Coak, S. Son, E. Suard, J.-G. Park, L. Clark and A. R. Wildes, *Phys. Rev. Mater.*, 2020, **4**, 084401.

81 T. Masubuchi, H. Hoya, T. Watanabe, Y. Takahashi, S. Ban, N. Ohkubo, K. Takase and Y. Takano, *J. Alloys Compd.*, 2008, **460**, 668–674.

82 V. Manríquez, P. Barahona and O. Peña, *Mater. Res. Bull.*, 2000, **35**, 1889–1895.

83 D. J. Goossens, S. Brazier-Hollins, D. R. James, W. D. Hutchison and J. R. Hester, *J. Magn. Magn. Mater.*, 2013, **334**, 82–86.

84 Y. He, Y.-D. Dai, H. Huang, J. Lin and Y. Hsia, *J. Alloys Compd.*, 2003, **359**, 41–45.

85 D. J. Goossens and T. J. Hicks, *J. Phys.: Condens. Matter*, 1998, **10**, 7643–7652.

86 A. Bhutani, J. L. Zuo, R. D. McAuliffe, C. R. dela Cruz and D. P. Shoemaker, *Phys. Rev. Mater.*, 2020, **4**, 034411.

87 Y. Shemerliuk, Y. Zhou, Z. Yang, G. Cao, A. U. B. Wolter, B. Büchner and S. Aswartham, *Electron. Mater*, 2021, **2**, 284–298.

88 S. Selter, Y. Shemerliuk, M.-I. Sturza, A. U. B. Wolter, B. Büchner and S. Aswartham, *Phys. Rev. Mater.*, 2021, **5**, 073401.

89 R. Basnet, A. Wegner, K. Pandey, S. Storment and J. Hu, *Phys. Rev. Mater.*, 2021, **5**, 064413.

90 F. Wang, N. Mathur, A. N. Janes, H. Sheng, P. He, X. Zheng, P. Yu, A. J. DeRuiter, J. R. Schmidt, J. He and S. Jin, *Sci. Adv.*, 2000, **7**, eabj4086.

91 S. Lee, J. Park, Y. Choi, K. Raju, W.-T. Chen, R. Sankar and K.-Y. Choi, *Phys. Rev. B*, 2021, **104**, 174412.

92 J. P. Odile, J. J. Steger and A. Wold, *Inorg. Chem.*, 1975, **14**, 2400–2402.

93 J. Peng, X. Yang, Z. Lu, L. Huang, X. Chen, M. He, J. Shen, Y. Xing, M. Liu, Z. Qu, Z. Wang, L. Li, S. Dong and J.-M. Liu, *Adv. Quantum Technol.*, 2023, **6**, 2200105.

94 S. Calder, A. V. Haglund, A. I. Kolesnikov and D. Mandrus, *Phys. Rev. B*, 2021, **103**, 024414.

95 P. Jeevanandam and S. Vasudevan, *J. Phys.: Condens. Matter*, 1999, **11**, 3563–3570.

96 X. Ma, L. Zhang, C. Xu, Q. Dong, R. I. Walton, Z. Li, H. Shi, G. Chen, J. Hu, J. Li and H. Yang, *Chem. Commun.*, 2020, **56**, 4603–4606.

97 M. Mi, X. Zheng, S. Wang, Y. Zhou, L. Yu, H. Xiao, H. Song, B. Shen, F. Li, L. Bai, Y. Chen, S. Wang, X. Liu and Y. Wang, *Adv. Funct. Mater.*, 2022, **32**, 2112750.

98 R. Basnet, D. Ford, K. TenBarge, J. Lochala and J. Hu, *J. Phys.: Condens. Matter*, 2022, **34**, 434002.

99 D. Tezze, J. M. Pereira, Y. Asensio, M. Ipatov, F. Calavalle, F. Casanova, A. M. Bittner, M. Ormaza, B. Martín-García, L. E. Hueso and M. Gobbi, *Nanoscale*, 2022, **14**, 1165–1173.

100 R. Brec, D. M. Schleich, G. Ouvrard, A. Louisy and J. Rouxel, *Inorg. Chem.*, 1979, **18**, 1814–1818.

101 E. Manova, A. Leaustic, I. Mitov, D. Gonbeau and R. Clement, *Mol. Cryst. Liq. Cryst. Sci. Technol., Sect. A*, 1998, **311**, 155–160.

102 J. J. Abraham, Y. Senyk, Y. Shemerliuk, S. Selter, S. Aswartham, B. Büchner, V. Kataev and A. Alfonsov, *Phys. Rev. B*, 2023, **107**, 165141.

103 M. Baithi, N. T. Dang, T. A. Tran, J. P. Fix, D. H. Luong, K. P. Dhakal, D. Yoon, A. V. Rutkauskas, S. E. Kichanov, I. Y. Zel, J. Kim, N. J. Borys, D. P. Kozlenko, Y. H. Lee and D. L. Duong, *Inorg. Chem.*, 2023, **62**, 12674–12682.

104 R. Nitsche and P. Wild, *Mater. Res. Bull.*, 1970, **5**, 419–423.

105 C. D. Carpentier and R. Nitsche, *Mater. Res. Bull.*, 1974, **9**, 401–410.

106 C. Liu, Z. Li, J. Hu, H. Duan, C. Wang, L. Cai, S. Feng, Y. Wang, R. Liu, D. Hou, C. Liu, R. Zhang, L. Zhu, Y. Niu, A. A. Zakharov, Z. Sheng and W. Yan, *Adv. Mater.*, 2023, **35**, 2300247.

107 D. Lançon, H. C. Walker, E. Ressouche, B. Ouladdiaf, K. C. Rule, G. J. McIntyre, T. J. Hicks, H. M. Rønnow and A. R. Wildes, *Phys. Rev. B*, 2016, **94**, 214407.

108 Q. Liu, L. Wang, Y. Fu, X. Zhang, L. Huang, H. Su, J. Lin, X. Chen, D. Yu, X. Cui, J.-W. Mei and J.-F. Dai, *Phys. Rev. B*, 2021, **103**, 235411.

109 K. Kim, S. Y. Lim, J. Kim, J.-U. Lee, S. Lee, P. Kim, K. Park, S. Son, C.-H. Park, J.-G. Park and H. Cheong, *2D Mater.*, 2019, **6**, 041001.

110 C.-T. Kuo, M. Neumann, K. Balamurugan, H. J. Park, S. Kang, H. W. Shiu, J. H. Kang, B. H. Hong, M. Han, T. W. Noh and J.-G. Park, *Sci. Rep.*, 2016, **6**, 20904.

111 H. Chu, C. J. Roh, J. O. Island, C. Li, S. Lee, J. Chen, J.-G. Park, A. F. Young, J. S. Lee and D. Hsieh, *Phys. Rev. Lett.*, 2020, **124**, 027601.

112 S. Lee, K.-Y. Choi, S. Lee, B. H. Park and J.-G. Park, *APL Mater.*, 2016, **4**, 086108.

113 T. Ying, T. Yu, Y.-S. Shiah, C. Li, J. Li, Y. Qi and H. Hosono, *J. Am. Chem. Soc.*, 2021, **143**, 7042–7049.

114 M. Cheng, Y.-S. Lee, A. K. Iyer, D. G. Chica, E. K. Qian, M. A. Shehzad, R. dos Reis, M. G. Kanatzidis and V. P. Dravid, *Inorg. Chem.*, 2021, **60**, 17268–17275.

115 D. G. Chica, A. K. Iyer, M. Cheng, K. M. Ryan, P. Krantz, C. Laing, R. dos Reis, V. Chandrasekhar, V. P. Dravid and M. G. Kanatzidis, *Inorg. Chem.*, 2021, **60**, 3502–3513.

116 M. Cheng, A. K. Iyer, A. P. Douvalis, S. M. Ribet, M. G. Kanatzidis and V. P. Dravid, *Chem. Mater.*, 2023, **35**, 1458–1465.

117 M. Cheng, A. K. Iyer, X. Zhou, A. Tyner, Y. Liu, M. A. Shehzad, P. Goswami, D. Y. Chung, M. G. Kanatzidis and V. P. Dravid, *Inorg. Chem.*, 2022, **61**, 13719–13727.

118 L.-J. Yao, C.-L. Hu, Z. Fang and J.-G. Mao, *J. Solid State Chem.*, 2022, **315**, 123433.

119 E. K. Qian, A. K. Iyer, M. Cheng, K. M. Ryan, L. Jirousek, D. G. Chica, P. Krantz, Y.-S. Lee, V. Chandrasekhar, V. P. Dravid and M. G. Kanatzidis, *Chem. Mater.*, 2023, **35**, 3671–3685.

120 B. L. Chittari, Y. Park, D. Lee, M. Han, A. H. MacDonald, E. Hwang and J. Jung, *Phys. Rev. B*, 2016, **94**, 184428.

121 X. Chen, J. Wang, T. Ying, D. Huang, H. Gou, Q. Zhang, Y. Li, H. Hosono, J. Guo and X. Chen, *Phys. Rev. B*, 2022, **106**, 184502.

122 R. Basnet, T. Patel, J. Wang, D. Upreti, S. K. Chhetri, G. Acharya, M. R. U. Nabi, J. Sakon and J. Hu, *Adv. Electron. Mater.*, 2024, **10**, 2300738.

123 A. R. Wildes, V. Simonet, E. Ressouche, G. J. McIntyre, M. Avdeev, E. Suard, S. A. J. Kimber, D. Lançon, G. Pepe, B. Moubaraki and T. J. Hicks, *Phys. Rev. B: Condens. Matter Mater. Phys.*, 2015, **92**, 224408.

124 W. Klingen, R. Ott and H. Hahn, *Z. Anorg. Allg. Chem.*, 1973, **396**, 271–278.

125 D. Khomskii, *Transition Metal Compounds*, Cambridge University Press, 2014.

126 M. Dalal, *A Textbook of Inorganic Chemistry – Volume 1*, Dalal Institute, 2017.

127 R. Basnet, *Understanding and Tuning Magnetism in van der Waals Magnetic Compounds*, Doctoral dissertation, University of Arkansas, 2023.

128 D. Lançon, R. A. Ewings, T. Guidi, F. Formisano and A. R. Wildes, *Phys. Rev. B*, 2018, **98**, 134414.

129 C. Kim, J. Jeong, P. Park, T. Masuda, S. Asai, S. Itoh, H.-S. Kim, A. Wildes and J.-G. Park, *Phys. Rev. B*, 2020, **102**, 184429.

130 A. R. Wildes, J. R. Stewart, M. D. Le, R. A. Ewings, K. C. Rule, G. Deng and K. Anand, *Phys. Rev. B*, 2022, **106**, 174422.

131 J. B. Goodenough, *Phys. Rev.*, 1955, **100**, 564–573.

132 J. Kanamori, *J. Phys. Chem. Solids*, 1959, **10**, 87–98.

133 N. Bazazzadeh, M. Hamdi, F. Haddadi, A. Khavasi, A. Sadeghi and S. M. Mohseni, *Phys. Rev. B*, 2021, **103**, 014425.

134 D. J. Goossens, A. R. Wildes, C. Ritter and T. J. Hicks, *J. Phys.: Condens. Matter*, 2000, **12**, 1845–1854.

135 D. J. Goossens, *Eur. Phys. J. B*, 2010, **78**, 305–309.

136 A. G. Chang, L.-W. Lan, Y.-J. Chan, C.-N. Kuo, T. Chen, C.-H. Huang, T.-H. Chuang, D.-H. Wei, C.-S. Lue and C.-C. Kuo, *Phys. Rev. B*, 2022, **106**, 125412.

137 Y. Lee, S. Son, C. Kim, S. Kang, J. Shen, M. Kenzelmann, B. Delley, T. Savchenko, S. Parchenko, W. Na, K.-Y. Choi, W. Kim, H. Cheong, P. M. Derlet, A. Kleibert and J.-G. Park, *Adv. Electron. Mater.*, 2023, **9**, 2200650.

138 R. R. Rao and A. K. Raychaudhuri, *J. Phys. Chem. Solids*, 1992, **53**, 577–583.

139 L. Bevaart, E. Frikkee and L. J. de Jongh, *Phys. Rev. B: Condens. Matter Mater. Phys.*, 1979, **19**, 4741–4756.

140 C.-K. Tian, C. Wang, W. Ji, J.-C. Wang, T.-L. Xia, L. Wang, J.-J. Liu, H.-X. Zhang and P. Cheng, *Phys. Rev. B*, 2019, **99**, 184428.

141 X. Hu, D.-X. Yao and K. Cao, *Phys. Rev. B*, 2022, **106**, 224423.

142 C. Tian, F. Pan, S. Xu, K. Ai, T. Xia and P. Cheng, *Appl. Phys. Lett.*, 2020, **116**, 202402.

143 G. Drachuck, Z. Salman, M. W. Masters, V. Taufour, T. N. Lamichhane, Q. Lin, W. E. Straszheim, S. L. Bud'ko and P. C. Canfield, *Phys. Rev. B*, 2018, **98**, 144434.

144 S. Pan, Y. Bai, J. Tang, P. Wang, Y. You, G. Xu and F. Xu, *J. Alloys Compd.*, 2022, **908**, 164573.

145 M. Abramchuk, S. Jaszewski, K. R. Metz, G. B. Osterhoudt, Y. Wang, K. S. Burch and F. Tafti, *Adv. Mater.*, 2018, **30**, 1801325.

146 T. A. Tartaglia, J. N. Tang, J. L. Lado, F. Bahrami, M. Abramchuk, G. T. McCandless, M. C. Doyle, K. S. Burch, Y. Ran, J. Y. Chan and F. Tafti, *Sci. Adv.*, 2020, **6**, eabb9379.

147 T. Masubuchi, X. Jin, K. Koyama, Y. Takahashi, K. Takase, Y. Uwatoko, Y. Takano and K. Sekizawa, *AIP Conf. Proc.*, 2006, **850**, 1279–1280.

148 T. Li, S. Jiang, N. Sivadas, Z. Wang, Y. Xu, D. Weber, J. E. Goldberger, K. Watanabe, T. Taniguchi, C. J. Fennie, K. Fai Mak and J. Shan, *Nat. Mater.*, 2019, **18**, 1303–1308.

149 S. Mondal, M. Kannan, M. Das, L. Govindaraj, R. Singha, B. Satpati, S. Arumugam and P. Mandal, *Phys. Rev. B*, 2019, **99**, 180407.

150 Y. Peng, Z. Lin, G. Tian, J. Yang, P. Zhang, F. Wang, P. Gu, X. Liu, C.-W. Wang, M. Avdeev, F. Liu, D. Zhou, R. Han, P. Shen, W. Yang, S. Liu, Y. Ye and J. Yang, *Adv. Funct. Mater.*, 2022, **32**, 2106592.

151 R. Oliva, E. Ritov, F. Horani, I. Etxebarria, A. K. Budniak, Y. Amouyal, E. Lifshitz and M. Guennou, *Phys. Rev. B*, 2023, **107**, 104415.

152 Z. Lu, X. Yang, L. Huang, X. Chen, M. Liu, J. Peng, S. Dong and J.-M. Liu, *J. Phys.: Condens. Matter*, 2022, **34**, 354005.

153 S. Selter, K. K. Bestha, P. Bhattacharyya, B. Özer, Y. Shemerliuk, M. Roslova, E. Vinokurova, L. T. Corredor, L. Veyrat, A. U. B. Wolter, L. Hozoi, B. Büchner and S. Aswartham, *Phys. Rev. Mater.*, 2023, **7**, 033402.

154 X. Wang, Z. Shang, C. Zhang, J. Kang, T. Liu, X. Wang, S. Chen, H. Liu, W. Tang, Y.-J. Zeng, J. Guo, Z. Cheng, L. Liu, D. Pan, S. Tong, B. Wu, Y. Xie, G. Wang, J. Deng, T. Zhai, H.-X. Deng, J. Hong and J. Zhao, *Nat. Commun.*, 2023, **14**, 840.

155 C. Payen, H. Mutka, J. L. Soubeyroux, P. Molinié and P. Colombet, *J. Magn. Magn. Mater.*, 1992, **104–107**, 797–798.

156 S. Selter, Y. Shemerliuk, B. Büchner and S. Aswartham, *Crystals*, 2021, **11**, 500.

157 H. Mutka, C. Payen, P. Molinié, J. L. Soubeyroux, P. Colombet and A. D. Taylor, *Phys. Rev. Lett.*, 1991, **67**, 497–500.

158 M. A. Gave, D. Bilc, S. D. Mahanti, J. D. Breshears and M. G. Kanatzidis, *Inorg. Chem.*, 2005, **44**, 5293–5303.

159 D. Kim, E. K. Qian, D. G. Chica, Y.-H. Chiang, M. G. Kanatzidis and Q. Tu, *ACS Appl. Nano Mater.*, 2023, **6**, 8214–8221.

160 A. Kargar, H. Hong, J. Tower, P. Guggenheim, E. Qian, C. Brown, M. Breen, J. F. Christian, K. Shah, E. Lukosi, R. Golduber, J. Gallagher, A. Benkechkache, M. Kanatzidis and M. R. Squillante, in *Hard X-Ray, Gamma-Ray, and Neutron Detector Physics XXIV*, SPIE, 2022, vol. 12241, pp. 59–12268.

161 D. G. Chica, Y. He, K. M. McCall, D. Y. Chung, R. O. Pak, G. Trimarchi, Z. Liu, P. M. De Lurgio, B. W. Wessels and M. G. Kanatzidis, *Nature*, 2020, **577**, 346–349.

162 A. del Moral, J. I. Arnaudas and P. M. Gehring, *J. Phys.: Condens. Matter*, 1994, **6**, 4779.

163 F. B. Anderson and H. B. Callen, *Phys. Rev.*, 1964, **136**, A1068–A1087.

164 L. J. D. Jongh and A. R. Miedema, *Adv. Phys.*, 2001, **50**, 947–1170.

165 K. Okuda, K. Kurosawa, S. Saito, M. Honda, Z. Yu and M. Date, *J. Phys. Soc. Jpn.*, 1986, **55**, 4456–4463.

166 A. P. Dioguardi, S. Selter, U. Peeck, S. Aswartham, M.-I. Sturza, R. Murugesan, M. S. Eldeeb, L. Hozoi, B. Büchner and H.-J. Grafe, *Phys. Rev. B*, 2020, **102**, 064429.

167 A. Bedoya-Pinto, J.-R. Ji, A. K. Pandeya, P. Gargiani, M. Valvidares, P. Sessi, J. M. Taylor, F. Radu, K. Chang and S. S. P. Parkin, *Science*, 2021, **374**, 616–620.

168 X. Cai, T. Song, N. P. Wilson, G. Clark, M. He, X. Zhang, T. Taniguchi, K. Watanabe, W. Yao, D. Xiao, M. A. McGuire, D. H. Cobden and X. Xu, *Nano Lett.*, 2019, **19**, 3993–3998.

169 J. Son, S. Son, P. Park, M. Kim, Z. Tao, J. Oh, T. Lee, S. Lee, J. Kim, K. Zhang, K. Cho, T. Kamiyama, J. H. Lee, K. F. Mak, J. Shan, M. Kim, J.-G. Park and J. Lee, *ACS Nano*, 2021, **15**, 16904–16912.

170 M. Baithi, N. T. Dang, T. A. Tran, J. P. Fix, D. H. Luong, K. P. Dhakal, D. Yoon, A. V. Rutkauskas, S. E. Kichanov, I. Y. Zel, J. Kim, N. J. Borys, D. P. Kozlenko, Y. H. Lee and D. L. Duong, *Inorg. Chem.*, 2023, **62**, 12674–12682.

171 Z.-L. Huang, J.-T. Zhao, J.-X. Mi, S.-Y. Mao and L.-S. Zheng, *J. Solid State Chem.*, 1999, **144**, 388–391.

172 D. Sen and T. Saha-Dasgupta, *Phys. Rev. Mater.*, 2023, **7**, 064008.

173 G. Ouvrard, R. Fréour, R. Brec and J. Rouxel, *Mater. Res. Bull.*, 1985, **20**, 1053–1062.

174 K. Ichimura and M. Sano, *Synth. Met.*, 1991, **45**, 203–211.

175 D. J. Goossens, D. James, J. Dong, R. E. Whitfield, L. Norén and R. L. Withers, *J. Phys.: Condens. Matter*, 2011, **23**, 065401.

176 P. Fuentealba, C. Olea, H. Aguilar-Bolados, N. Audebrand, R. C. de Santana, C. Doerenkamp, H. Eckert, C. J. Magon and E. Spodine, *Phys. Chem. Chem. Phys.*, 2020, **22**, 8315–8324.

177 R. Basnet, D. Upreti, T. Patel, S. Karki Chhetri, G. Acharya, M. R. U. Nabi, M. M. Sharma, J. Sakon, M. Mortazavi and J. Hu, *Phys. Rev. B*, 2024, **109**, 184405.

178 Y. Peng, S. Ding, M. Cheng, Q. Hu, J. Yang, F. Wang, M. Xue, Z. Liu, Z. Lin, M. Avdeev, Y. Hou, W. Yang, Y. Zheng and J. Yang, *Adv. Mater.*, 2020, **32**, 2001200.

179 M. A. McGuire, G. Clark, S. KC, W. M. Chance, G. E. Jellison, V. R. Cooper, X. Xu and B. C. Sales, *Phys. Rev. Mater.*, 2017, **1**, 014001.

180 E. J. Telford, A. H. Dismukes, K. Lee, M. Cheng, A. Wieteska, A. K. Bartholomew, Y.-S. Chen, X. Xu, A. N. Pasupathy, X. Zhu, C. R. Dean and X. Roy, *Adv. Mater.*, 2020, **32**, 2003240.

181 D. Upreti, R. Basnet, M. M. Sharma, S. K. Chhetri, G. Acharya, M. R. U. Nabi, J. Sakon, M. Mortazavi and J. Hu, 2024, arXiv:2408.02858. DOI: 10.48550/arXiv.2408.02858.

182 T. Matsuoka, R. Rao, M. A. Susner, B. S. Conner, D. Zhang and D. Mandrus, *Phys. Rev. B*, 2023, **107**, 165125.

183 W. Bai, Z. Hu, C. Xiao, J. Guo, Z. Li, Y. Zou, X. Liu, J. Zhao, W. Tong, W. Yan, Z. Qu, B. Ye and Y. Xie, *J. Am. Chem. Soc.*, 2020, **142**, 10849–10855.

184 O. V. Yazyev and L. Helm, *Phys. Rev. B: Condens. Matter Mater. Phys.*, 2007, **75**, 125408.

185 L. Cai, J. He, Q. Liu, T. Yao, L. Chen, W. Yan, F. Hu, Y. Jiang, Y. Zhao, T. Hu, Z. Sun and S. Wei, *J. Am. Chem. Soc.*, 2015, **137**, 2622–2627.

186 V. K. S. Shante and S. Kirkpatrick, *Adv. Phys.*, 1971, **20**, 325–357.

187 V. Pashchenko, O. Bludov, D. Baltrunas, K. Mazeika, S. Motria, K. Glukhov and Yu. Vysochanskii, *Condens. Matter Phys.*, 2022, **25**, 43701.

188 A. Bhowmick, B. Bal, S. Ganguly, M. Bhattacharya and M. L. Kundu, *J. Phys. Chem. Solids*, 1992, **53**, 1279–1284.

189 T. Ying, T. Yu, Y. Qi, X. Chen and H. Hosono, *Adv. Sci.*, 2022, **9**, 2203219.

190 P. Colombet, A. Leblanc, M. Danot and J. Rouxel, *J. Solid State Chem.*, 1982, **41**, 174–184.

191 T. Asano, Y. Ajiro, M. Mekata, H. Yamazaki, N. Hosoito, T. Shinjo and H. Kikuchi, *Solid State Commun.*, 1994, **90**, 125–128.

192 C. Payen, P. Molinie, P. Colombet and G. Fillion, *J. Magn. Magn. Mater.*, 1990, **84**, 95–101.

193 S. Lee, P. Colombet, G. Ouvrard and R. Brec, *Mater. Res. Bull.*, 1986, **21**, 917–928.
194 S. Selter, K. K. Bestha, P. Bhattacharyya, B. Özer, Y. Shemerliuk, L. T. Corredor, L. Veyrat, A. U. B. Wolter, L. Hozoi, B. Büchner and S. Aswartham, *Phys. Rev. Mater.*, 2022, **7**, 033402.
195 Y. Ma, Y. Yan, L. Luo, S. Pazos, C. Zhang, X. Lv, M. Chen, C. Liu, Y. Wang, A. Chen, Y. Li, D. Zheng, R. Lin, H. Algaidi, M. Sun, J. Z. Liu, S. Tu, H. N. Alshareef, C. Gong, M. Lanza, F. Xue and X. Zhang, *Nat. Commun.*, 2023, **14**, 7891.
196 X. Bourdon, V. Maisonneuve, V. B. Cajipe, C. Payen and J. E. Fischer, *J. Alloys Compd.*, 1999, **283**, 122–127.
197 Y. Peng, X. Cheng, P. Gu, F. Wang, J. Yang, M. Xue, W. Yang, C. Wang, S. Liu, K. Watanabe, T. Taniguchi, Y. Ye and J. Yang, *Adv. Funct. Mater.*, 2020, **30**, 1910036.
198 M. A. Susner, B. S. Conner, E. Rowe, R. Siebenaller, A. Giordano, M. V. McLeod, C. R. Ebbing, T. J. Bullard, R. Selhorst, T. J. Haugan, J. Jiang, R. Pachter and R. Rao, *J. Phys. Chem. C*, 2024, **128**, 4265–4276.
199 X. Yan, X. Chen and J. Qin, *Mater. Res. Bull.*, 2011, **46**, 235–238.
200 G. Kliche, *Z. Naturforsch., A: Astrophys., Phys. Phys. Chem.*, 1983, **38**, 1133–1137.
201 B. Zapeka, M. Kostyrko, I. Martynyuk-Lototska and R. Vlokh, *Philos. Mag.*, 2015, **95**, 382–393.
202 B. Hillman, L. Noren and D. J. Goossens, in Proceedings of the 35th Annual Australia/New Zealand Condensed Matter and Materials Meeting, (Australian Institute of Physics, 2011), p. 50.
203 Y. Gu, Q. Zhang, C. Le, Y. Li, T. Xiang and J. Hu, *Phys. Rev. B*, 2019, **100**, 165405.
204 Y. Yu, G. Deng, Y. Cao, G. J. McIntyre, R. Li, N. Yuan, Z. Feng, J.-Y. Ge, J. Zhang and S. Cao, *Ceram. Int.*, 2019, **45**, 1093–1097.
205 A. M. Ruiz, D. L. Esteras, A. Rybakov and J. J. Baldoví, *Dalton Trans.*, 2022, **51**, 16816–16823.
206 J. L. Lado and J. Fernández-Rossier, *2D Mater.*, 2017, **4**, 035002.
207 G. Wang, K. Yang, Y. Ma, L. Liu, D. Lu, Y. Zhou and H. Wu, *Chin. Phys. Lett.*, 2023, **40**, 077301.
208 A. Le Méhauté, G. Ouvrard, R. Brec and J. Rouxel, *Mater. Res. Bull.*, 1977, **12**, 1191–1197.
209 P. J. S. Foot and B. A. Nevett, *Solid State Ionics*, 1983, **8**, 169–172.
210 D. Upreti, R. Basnet, M. M. Sharma, S. K. Chhetri, G. Acharya, M. R. U. Nabi, J. Sakon, B. Da, M. Mortazavi and J. Hu, 2024, DOI: **10.48550/arXiv.2407.12662**.
211 C. Yang, X. Chen, J. Qin, K. Yakushi, Y. Nakazawa and K. Ichimura, *J. Solid State Chem.*, 2000, **150**, 281–285.
212 J. S. O. Evans, D. O'Hare, R. Clement, A. Leaustic and P. Thuéry, *Adv. Mater.*, 1995, **7**, 735–739.
213 D. P. Kozlenko, O. N. Lis, N. T. Dang, M. Coak, J.-G. Park, E. V. Lukin, S. E. Kichanov, N. O. Golosova, I. Yu. Zel and B. N. Savenko, *Phys. Rev. Mater.*, 2024, **8**, 024402.
214 M. J. Coak, D. M. Jarvis, H. Hamidov, A. R. Wildes, J. A. M. Paddison, C. Liu, C. R. S. Haines, N. T. Dang, S. E. Kichanov, B. N. Savenko, S. Lee, M. Kratochvílová, S. Klotz, T. C. Hansen, D. P. Kozlenko, J.-G. Park and S. S. Saxena, *Phys. Rev. X*, 2021, **11**, 011024.
215 H. Sun, L. Qiu, Y. Han, E. Yi, J. Li, M. Huo, C. Huang, H. Liu, M. Li, W. Wang, D.-X. Yao, B. A. Frandsen, B. Shen, Y. Hou and M. Wang, *Mater. Today Phys.*, 2023, **36**, 101188.
216 W. Toyoshima, T. Masubuchi, T. Watanabe, K. Takase, K. Matsubayashi, Y. Uwatoko and Y. Takano, *J. Phys.: Conf. Ser.*, 2009, **150**, 042215.
217 T. Matsuoka, H.-S. Kim, S. Samanta, J. L. Musfeldt and D. G. Mandrus, *Front. Mater.*, 2024, **11**, 1362744.
218 L. Min, M. Sretenovic, T. W. Heitmann, T. W. Valentine, R. Zu, V. Gopalan, C. M. Rost, X. Ke and Z. Mao, *Commun. Phys.*, 2022, **5**, 1–7.
219 L. Thiel, Z. Wang, M. A. Tschudin, D. Rohner, I. Gutiérrez-Lezama, N. Ubrig, M. Gibertini, E. Giannini, A. F. Morpurgo and P. Maletinsky, *Science*, 2019, **364**, 973–976.
220 Q. Zhang, K. Hwangbo, C. Wang, Q. Jiang, J.-H. Chu, H. Wen, D. Xiao and X. Xu, *Nano Lett.*, 2021, **21**, 6938–6945.
221 J. Yang, Y. Zhou, Y. Dedkov and E. Voloshina, *Adv. Theory Simul.*, 2020, **3**, 2000228.
222 N. Sheremetyeva, I. Na, A. Saraf, S. M. Griffin and G. Hautier, *Phys. Rev. B*, 2023, **107**, 115104.
223 R. N. Jenjeti, R. Kumar, M. P. Austeria and S. Sampath, *Sci. Rep.*, 2018, **8**, 8586.
224 J. Duan, P. Chava, M. Ghorbani-Asl, Y. Lu, D. Erb, L. Hu, A. Echresh, L. Rebohle, A. Erbe, A. V. Krasheninnikov, M. Helm, Y.-J. Zeng, S. Zhou and S. Prucnal, *ACS Appl. Mater. Interfaces*, 2022, **14**, 11927–11936.
225 P. Liu and Y. Pu, *Results Phys.*, 2021, **29**, 104750.
226 T. Xu, M. Luo, N. Shen, Y. Yu, Z. Wang, Z. Cui, J. Qin, F. Liang, Y. Chen, Y. Zhou, F. Zhong, M. Peng, M. Zubair, N. Li, J. Miao, W. Lu, C. Yu and W. Hu, *Adv. Electron. Mater.*, 2021, **7**, 2100207.
227 X. Han, P. Song, J. Xing, Z. Chen, D. Li, G. Xu, X. Zhao, F. Ma, D. Rong, Y. Shi, Md. R. Islam, K. Liu and Y. Huang, *ACS Appl. Mater. Interfaces*, 2021, **13**, 2836–2844.
228 Y. Liu and X. Sun, *Magnetochemistry*, 2022, **8**, 101.
229 R. Kumar, R. N. Jenjeti and S. Sampath, *Adv. Mater. Interfaces*, 2019, **6**, 1900666.
230 *Spontaneous Ordering in Semiconductor Alloys*, ed. A. Mascarenhas, Springer US, Boston, MA, 2002.
231 B. Cao, S. Chen, X. Jin, J. Liu and T. Li, *ACS Appl. Mater. Interfaces*, 2020, **12**, 57245–57253.
232 X. Jin, S. Chen and T. Li, *Commun. Mater.*, 2022, **3**, 1–9.
233 R. Zhang, S. Zhao, J. Ding, Y. Chong, T. Jia, C. Ophus, M. Asta, R. O. Ritchie and A. M. Minor, *Nature*, 2020, **581**, 283–287.
234 J. Ding, Q. Yu, M. Asta and R. O. Ritchie, *Proc. Natl. Acad. Sci. U. S. A.*, 2018, **115**, 8919–8924.
235 B. Jiang, Y. Yu, J. Cui, X. Liu, L. Xie, J. Liao, Q. Zhang, Y. Huang, S. Ning, B. Jia, B. Zhu, S. Bai, L. Chen, S. J. Pennycook and J. He, *Science*, 2021, **371**, 830–834.

236 S. Roychowdhury, T. Ghosh, R. Arora, M. Samanta, L. Xie, N. K. Singh, A. Soni, J. He, U. V. Waghmare and K. Biswas, *Science*, 2021, **371**, 722–727.

237 H. Ji, A. Urban, D. A. Kitchaev, D.-H. Kwon, N. Artrith, C. Ophus, W. Huang, Z. Cai, T. Shi, J. C. Kim, H. Kim and G. Ceder, *Nat. Commun.*, 2019, **10**, 592.

238 K. Kim, S. Y. Lim, J. Kim, J.-U. Lee, S. Lee, P. Kim, K. Park, S. Son, C.-H. Park, J.-G. Park and H. Cheong, *2D Mater.*, 2019, **6**, 041001.

239 K. C. Rule, G. J. McIntyre, S. J. Kennedy and T. J. Hicks, *Phys. Rev. B: Condens. Matter Mater. Phys.*, 2007, **76**, 134402.

240 Y. Jin, Y. Jin, K. Li, M. Yan, Y. Guo, Y. Zhou, A. Preobrajenski, Y. Dedkov and E. Voloshina, *J. Phys. Chem. Lett.*, 2022, **13**, 10486–10493.

241 T. T. Mai, K. F. Garrity, A. McCreary, J. Argo, J. R. Simpson, V. Doan-Nguyen, R. V. Aguilar and A. R. H. Walker, *Sci. Adv.*, 2021, **7**, eabj3106.

242 D. Jana, P. Kapuscinski, A. Pawbake, A. Papavasileiou, Z. Sofer, I. Breslavetz, M. Orlita, M. Potemski and C. Faugeras, *Phys. Rev. B*, 2023, **108**, 144415.

243 R. Gusmão, Z. Sofer, D. Sedmidubský, Š. Huber and M. Pumera, *ACS Catal.*, 2017, **7**, 8159–8170.

244 L. Liao, E. Kovalska, V. Mazanek, L. Valdman, L. Dekanovsky, W. Bing, D. Sedmidubský, J. Luxa, Š. Huber, A. P. Herman, R. Kudrawiec and Z. Sofer, *J. Mater. Chem. C*, 2022, **10**, 8834–8844.

245 J. Zhang, W. Xu, L. Wang, Z. Zheng, F. Liu, P. Yu and G. Yang, *Cryst. Growth Des.*, 2023, **23**, 1259–1268.

246 X. Zhao, X. Yin, D. Liu, C. Huo, G.-Z. Dong, S. Chen, Z.-B. Liu, X.-Q. Yan and J.-G. Tian, *J. Phys. Chem. C*, 2022, **126**, 6837–6846.

247 X. Wang, K. Du, W. Liu, P. Hu, X. Lu, W. Xu, C. Kloc and Q. Xiong, *Appl. Phys. Lett.*, 2016, **109**, 123103.

248 D. Lançon, R. A. Ewings, T. Guidi, F. Formisano and A. R. Wildes, *Phys. Rev. B*, 2018, **98**, 134414.